Characterization of high harmonic generation from gas under loose focusing condition

PhD thesis

Nagyillés Balázs

Supervisors:

Divéki Zsolt

Extreme Light Infrastructure - Attosecond Light Pulse Source

and

Subhendu Kahaly

Extreme Light Infrastructure - Attosecond Light Pulse Source

University of Szeged, Doctoral School of Physics

2025

Contents

List of Abbreviations

ADK	Ammosov-Delone-Krainov
ATI	Above-Threshold Ionization
CEP	Carrier-envelope phase
ELI ALPS	Extreme Light Infrastructure Attosecond Light Pulse Source
GD	Group delay
GDD	Group Delay Dispersion
HHG	High harmonic generation
IR	Infrared
LASSO	Least Absolute Shrinkage and Selection Operator
MCP	Microchannel plate detector
MIR	Mid-Infrared
ML	Machine Learning
MZI	Mach–Zehnder interferometer
NIST	National Institute of Standards and Technology
OPCPA	Optical Parametric Chirped Pulse Amplification
ROM	Relativistically Oscillating Mirror
SFA	Strong field approximation
SHHG	Solid-state high harmonic generation
TDSE	Time-Dependent Schrödinger Equation
VUV	Vacuum Ultra Violet
XUV	Extreme ultraviolet
YAG	Yttrium Aluminium Garnet
ZnO	Zinc Oxide Crystal

Chapter 1

Scientific background

1.1 Introduction

With the invention of the laser [1], it became possible to generate coherent light pulses short enough to capture transient phenomena in matter. As laser technology evolved [2], the relentless pursuit of ever shorter pulse durations was driven by the principle that faster pulses unveil faster and more localized dynamics [3, 4]. This quest has not only deepened our understanding of ultrafast processes but has also catalyzed progress in applied research [5] and spurred innovations in industrial domains where precise timing and ultrafast control are paramount [6].

The historical trend toward shorter pulse durations, together with the steady increase of achievable peak intensities, is summarized in Fig. 1.1 [7], which illustrates the remarkable progress achieved through innovations in laser physics and nonlinear optics.

Despite these advances, there are fundamental limits on how short pulses can be directly generated from conventional laser gain media. These limits are imposed by the finite spectral bandwidth supported by the medium and by the difficulty of achieving uniform and controllable spectral phase across broad bandwidths. For state-of-the-art systems such as Ti:sapphire lasers and optical parametric amplifiers, the minimum pulse durations are typically in the 5–6 fs range [8, 9]. Pushing further into the single-cycle regime, near 2 fs in the NIR, requires post-compression techniques. These involve spectral broadening in hollow-core fibers [10–13] followed by dispersion compensation using chirped mirrors [14, 15] or acousto-optic modulators [16]. While effective, these methods face practical limitations, beyond which direct laser-driven generation of shorter pulses becomes increasingly challenging. More recent developments include multi-pass cells [17, 18] and bulk-material compression schemes [19, 20].

To generate even shorter pulse durations, in the sub-femtosecond regime, one needs to expand the spectrum to the shorter wavelength range where enough bandwidth can be supported with the required spectral phase. To this end, alternative methods have been developed. Among them, high-order harmonic generation (HHG) has emerged as one of

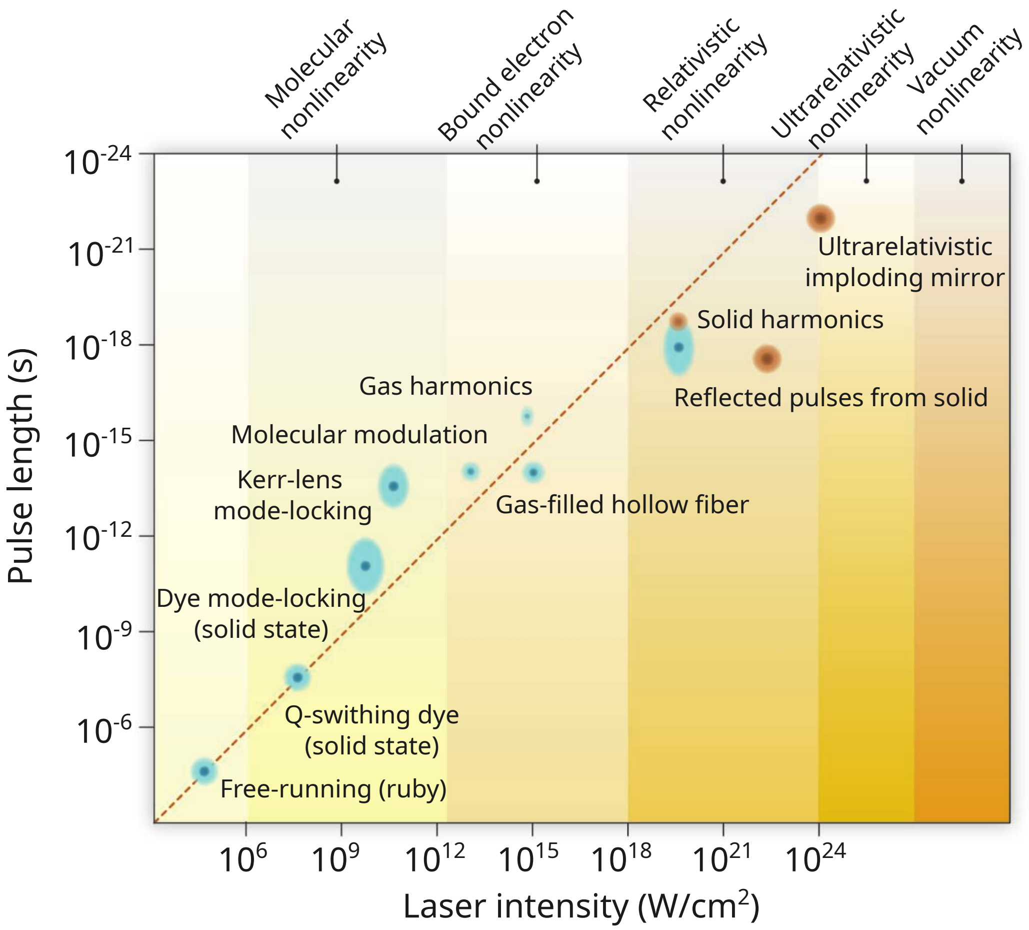

FIGURE 1.1: Historical progression of the shortest generated light pulses. [7] Over 18 orders of magnitude, the pulse duration of coherent light emission scales inversely with laser intensity. Blue areas indicate experiments, red areas mark simulations or theory as 2011.

the most mature and experimentally accessible approach [21, 22]. Other concepts, such as ultrabroadband light synthesis with coherent phase control [23] or free-electron lasers (FEL) driven by plasma wakefield accelerators [24], promise extreme photon energies and ultrashort durations but typically demand large-scale infrastructure and complex instrumentation [25]. In contrast, HHG can be realized on a table-top scale while delivering femtosecond-to-attosecond pulses with high spatial and temporal coherence [26–28].

HHG is an inherently nonlinear process, in which a strong laser field drives atoms or molecules to emit photons at multiples of the fundamental frequency. These higher order harmonics can be either odd or even, depending on the symmetry properties of the medium [29] or electric field [30, 31], where generation takes place. The resulting spectrum can extend from the extreme ultraviolet (XUV) into the soft X-ray regime [32–34]. A breakthrough in the early 2000s showed that HHG could be harnessed to generate isolated attosecond bursts [27] or pulse trains [26], establishing the foundations of attosecond science and enabling direct time-domain studies of electron motion and ultrafast quantum dynamics.

The first experimental observation of HHG was reported in 1987 by independent groups in Chicago [35] and at CEA Saclay [36]. These early experiments used rare noble gases such as argon, krypton, and xenon, driven by the most advanced lasers of the time: Nd:YAG systems at 1064 nm [36], KrF excimer lasers at 248 nm [37, 38], and Ti:sapphire lasers at 800 nm [38–40]. Through the 1990s and early 2000s, the field expanded to include molecular targets [41–43], revealing the role of molecular orbitals and nuclear motion in strong-field dynamics. Major milestones followed, including the demonstration of HHG from plasma surfaces at ultra-high intensities [44–46], and the discovery of high-harmonic emission from bulk crystals in 2010 [47–49].

The solid-state breakthrough marked the beginning of a new chapter, emphasizing the potential of condensed matter systems as compact and efficient sources of attosecond light. Compared to gases, solids offer higher target densities and better integration prospects with photonic technologies, though the physics involves richer dynamics such as interband transitions and band-structure effects.

Today, HHG serves both as a powerful light source and as a precision probe, enabling applications ranging from ultrafast spectroscopy [26, 27, 50, 51] to coherent diffractive imaging [52, 53] to relativistic plasma optics [54–56] and time-resolved electron dynamics. Its continuing development remains central to advancing attosecond metrology and next-generation ultrafast light sources.

1.2 High Harmonic Generation

Over the past several decades, a variety of theoretical approaches have been developed to describe and interpret high-order harmonic generation. These range from simple classical trajectory models [57] to fully quantum mechanical treatments based on numerical solutions of the time-dependent Schrödinger equation (TDSE) [58]. Each approach provides its own perspective on the physics of HHG, depending on the underlying assumptions and the available computational resources.

In classical models, electron motion is described using Newtonian dynamics, typically framed within the well-known three-step picture: tunnel ionization, acceleration in the laser field, and recombination with the parent ion accompanied by high-energy photon emission [59, 60]. Such models give clear physical intuition and are particularly effective for predicting cutoff energies and understanding temporal gating mechanisms. However, they cannot capture quantum interference effects or reproduce all the detailed structures of the harmonic spectrum.

At the opposite end, full TDSE simulations provide an ab initio description by following the time evolution of the electron wave function in the combined atomic potential and external laser field. While computationally demanding, these calculations can reproduce fine spectral features and coherence effects intrinsic to HHG [61–63].

Between these two extremes lies the widely used semi-classical model introduced by Lewenstein and co-workers in 1994 [64]. Built upon the strong-field approximation (SFA), this framework provides a practical means of calculating the induced dipole moment of an atom exposed to an intense laser field. The Lewenstein model successfully reproduces the key features of HHG, including the plateau structure of the spectrum and the cutoff law that scales with laser intensity and wavelength. Such an approach, in combination with Saddle Point Analysis [65], can also reveal trajectory-based quantum path interference features (see [66] and references therein). Because of its balance between physical transparency and computational efficiency, it has become a cornerstone in HHG theory and is frequently incorporated into larger simulations that include macroscopic propagation.

In practice, the Lewenstein model has proven invaluable for interpreting experiments and guiding the design of optimized HHG setups. Despite its simplifying assumptions—most notably the neglect of the Coulomb potential after ionization—it shows excellent agreement with experimental results, particularly when combined with propagation models that account for dispersion, absorption, and phase matching in the generating medium.

1.2.1 Keldysh theory of ionization

Before introducing the Lewenstein model, it is useful to revisit the Keldysh theory of strong-field ionization [67, 68], which provides the natural starting point for a discussion on HHG. Within the SFA framework, the continuum electron is represented by a Volkov state, and the transition amplitude from the bound state is calculated using the time-dependent Schrödinger equation. Keldysh demonstrated that the nature of ionization is determined by a single dimensionless parameter,

$$\gamma = \sqrt{\frac{I_p}{2U_p}} = \frac{\omega}{E_0}\sqrt{2I_p}, \tag{1.1}$$

which compares the tunneling time through the laser-suppressed Coulomb barrier to the optical period of the driving field, I_p is the ionization potential of the target atom or molecule and U_p is the ponderomotive energy. This can be written with the electric field amplitude E_0, using the relation $U_p = E_0/(4\,\omega_0^2)$, where ω is the center frequency of the laser field.

When $\gamma \gg 1$, ionization takes place in the multiphoton regime, requiring the absorption of a discrete number of photons. In contrast, for $\gamma \ll 1$ the process takes place via tunneling, where the electron escapes the barrier essentially in a static field. At the intermediate case $\gamma \simeq 1$, both regimes overlap, and the Keldysh theory provides a smooth interpolation between the two limits. Importantly, this framework not only explains the onset of tunneling ionization in strong fields, but also connects directly to the saddle-point picture in the Lewenstein model, where the electron is assumed to tunnel at a complex ionization time and subsequently propagate in the continuum as a Volkov state.

The relevance of the Keldysh parameter for HHG is clear when considering why perturbative multiphoton theory fails to describe experimental spectra. In the perturbative limit, the intensity of the n^{th} harmonic scales as I^{n} and drops rapidly with increasing order, predicting only a few observable harmonics. Experiments, however, reveal a broad plateau with nearly constant intensity across many harmonics, followed by a sharp cutoff. Such behavior can only occur in the non-perturbative tunneling regime ($\gamma \ll 1$), where the electron dynamics are governed by the continuum excursion in the laser field rather than by the absorption of individual photons. This breakdown of perturbation theory is the central reason why HHG must be treated within the strong-field approximation, and why the Lewenstein integral—built upon the Keldysh ionization step and Volkov propagation—forms the appropriate theoretical framework. This plateau structure in HHG is one of the key aspects in attosecond pulse generation.

1.2.2 Time-dependent Schrödinger equation

To arrive at the Lewenstein integral for HHG within the strong-field approximation, we begin with the time-dependent Schrödinger equation for a single active electron in an atom subject to a strong laser field (for a detailed discussion elucidating all the assumptions, see Ref. [65]). In the length gauge and under the dipole approximation, the equation reads [69]:

$$i\frac{\partial}{\partial t}\psi(\vec{r},t) = \left(-\frac{1}{2}\nabla^2 + V(\vec{r}) + \vec{r}\cdot\vec{E}(t)\right)\psi(\vec{r},t), \tag{1.2}$$

with $V(\vec{r})$ the atomic potential and $\vec{E}(t)$ the driving electric field. Atomic units are used throughout ($\hbar = m_e = |e| = 1$). The system is assumed to start in the ground state at $t \to -\infty$, i.e. $\psi(\vec{r}, t \to -\infty) = \phi_g(\vec{r})$, where the field-free Hamiltonian $H_0 = -\frac{1}{2}\nabla^2 + V(\vec{r})$ satisfies $H_0\phi_g = E_g\phi_g$ with $E_g = -I_p$. Here $I_p > 0$ denotes the ionization potential.

SFA [67, 70, 71] assumes that, once ionized, the electron's motion in the continuum is driven almost entirely by the laser field, so the atomic potential can be neglected during this stage [4, 64]. Ground-state depletion is also neglected, keeping its amplitude essentially constant. Continuum dynamics are then described by Volkov states, which are exact solutions of the free-electron Schrödinger equation in the presence of the external field:

$$i\partial_t \chi = \left(-\tfrac{1}{2}\nabla^2 + \vec{r}\cdot\vec{E}(t)\right)\chi. \tag{1.3}$$

Introducing the vector potential $\vec{A}(t) = -\int_{-\infty}^{t}\vec{E}(s)\,ds$, the Volkov solution in the length gauge takes the form [65, 71]

$$\chi_{\vec{p}}(\vec{r},t) = (2\pi)^{-3/2}\exp\left[i(\vec{p}+\vec{A}(t))\cdot\vec{r} - i\int_{-\infty}^{t}\frac{[\vec{p}+\vec{A}(s)]^2}{2}\,ds\right], \tag{1.4}$$

where, the field-induced momentum shift and the accumulated phase from the classical action are explicitly included.

The full wave function can be written in integral form using the time-evolution operator $U(t,t')$:

$$\psi(t) = U(t,-\infty)|\phi_g\rangle = e^{iI_pt}|\phi_g\rangle. \tag{1.5}$$

Within the SFA, propagation after ionization is approximated with the Volkov propagator $U_V(t,t')$, defined by

$$i\partial_t U_V = \left(-\tfrac{1}{2}\nabla^2 + \vec{r}\cdot\vec{E}(t)\right)U_V, \qquad U_V(t,t) = 1, \tag{1.6}$$

whose momentum-space representation is

$$U_V(t,t') = \int\frac{d^3p}{(2\pi)^3}|\chi_{\vec{p}}(t)\rangle\langle\chi_{\vec{p}}(t')|. \tag{1.7}$$

The approximate wave function then becomes [64]

$$\psi(t) = e^{iI_pt}|\phi_g\rangle - i\int_{-\infty}^{t}dt'\,U_V(t,t')\,(\vec{r}\cdot\vec{E}(t'))\,e^{iI_pt'}|\phi_g\rangle, \tag{1.8}$$

where the exponential prefactor reflects the ground-state phase evolution ($e^{-iE_gt} = e^{iI_pt}$).

The quantity of interest for HHG is the time-dependent dipole moment

$$\vec{d}(t) = \langle\psi(t)|\vec{r}|\psi(t)\rangle, \tag{1.9}$$

whose Fourier transform yields the emitted harmonic spectrum. Since $\langle\phi_g|\vec{r}|\phi_g\rangle = 0$ and the continuum–continuum contribution is neglected in the SFA, the leading contribution comes from the ground–continuum cross term:

$$\vec{d}(t) = -ie^{iI_pt}\int_{-\infty}^{t}dt'\,e^{iI_pt'}\langle\phi_g|\vec{r}\,U_V(t,t')\,(\vec{r}\cdot\vec{E}(t'))|\phi_g\rangle + \text{c.c.} \tag{1.10}$$

Inserting the explicit form of the Volkov propagator gives

$$\langle\phi_g|\vec{r}\,U_V(t,t')\,(\vec{r}\cdot\vec{E}(t'))|\phi_g\rangle = \int \frac{d^3p}{(2\pi)^3}\langle\phi_g|\vec{r}|\chi_{\vec{p}}(t)\rangle\langle\chi_{\vec{p}}(t')|\vec{r}\cdot\vec{E}(t')|\phi_g\rangle. \tag{1.11}$$

Assuming linear polarization along z, the field reduces to $\vec{E}(t) = E(t)\hat{z}$, $\vec{A}(t) = A(t)\hat{z}$, and the dipole moment simplifies to

$$d(t) = i\int_{-\infty}^{t} dt'\,E(t')\int \frac{d^3p}{(2\pi)^3}\langle\phi_g|z|\chi_{\vec{p}}(t)\rangle\langle\chi_{\vec{p}}(t')|z|\phi_g\rangle\,e^{iI_p(t-t')} + \text{c.c.}. \tag{1.12}$$

The recombination and ionization matrix elements are obtained directly from the Volkov form. For recombination,

$$\langle\phi_g|z|\chi_{\vec{p}}(t)\rangle = \exp\left(-i\int_{-\infty}^{t}\frac{[\vec{p}+\vec{A}(s)]^2}{2}\,ds\right)\tilde{d}[\vec{p}+\vec{A}(t)], \tag{1.13}$$

where $\tilde{d}(\vec{k}) = \langle\phi_g|z|\vec{k}\rangle$ is the bound–continuum transition dipole. Similarly, for ionization,

$$\langle\chi_{\vec{p}}(t')|z|\phi_g\rangle = \exp\left(i\int_{-\infty}^{t'}\frac{[\vec{p}+\vec{A}(s)]^2}{2}\,ds\right)\tilde{d}^*[\vec{p}+\vec{A}(t')]. \tag{1.14}$$

Multiplying the two gives

$$\langle\phi_g|z|\chi_{\vec{p}}(t)\rangle\langle\chi_{\vec{p}}(t')|z|\phi_g\rangle = \tilde{d}[\vec{p}+\vec{A}(t)]\,\tilde{d}^*[\vec{p}+\vec{A}(t')]\exp\left(-i\int_{t'}^{t}\frac{[\vec{p}+\vec{A}(s)]^2}{2}\,ds\right). \tag{1.15}$$

Including the ground-state phase, the exponential factor becomes

$$\exp\left(-i\int_{t'}^{t}\frac{[\vec{p}+\vec{A}(s)]^2}{2}\,ds + iI_p(t-t')\right) = \exp\left(-i\int_{t'}^{t}\left[\tfrac{[\vec{p}+\vec{A}(s)]^2}{2}+I_p\right]ds\right). \tag{1.16}$$

Altogether, the Lewenstein expression for the dipole moment is

$$\vec{d}(t) = i\int_{-\infty}^{t}dt'\int\frac{d^3p}{(2\pi)^3}\,\underbrace{\vec{E}(t')\cdot\vec{d}(\vec{p}+\vec{A}(t'))}_{\text{ionization}}\,\underbrace{e^{-iS(\vec{p},t,t')}}_{\text{propagation}}\,\underbrace{\vec{d}^*(\vec{p}+\vec{A}(t))}_{\text{recombination}}+\text{c.c.}, \tag{1.17}$$

where the semiclassical action is

$$S(\vec{p},t,t') = \int_{t'}^{t} \left(\tfrac{[\vec{p}+\vec{A}(s)]^2}{2} + I_p \right) ds. \tag{1.18}$$

Equation (1.17) incorporates the three-step model of HHG. The ionization factor represents tunneling from the ground state at time t', the propagation factor carries the accumulated phase of the free electron in the laser field, and the recombination factor gives the overlap of the returning electron with the bound state at time t.

1.2.3 Saddle point approximation

To evaluate the Lewenstein integral [65, 72] and extract the harmonic spectrum, we take the Fourier transform of the time-dependent dipole moment $d(t)$. For harmonics at positive frequencies $\Omega > 0$, the Fourier component is defined as

$$a(\Omega) = \int_{-\infty}^{\infty} dt\, e^{i\Omega t}\, d(t), \tag{1.19}$$

where the integration extends over the pulse duration. For multi-cycle pulses, this is effectively over a long time window, while for spectral density one normalizes by the total duration. Substituting the Lewenstein expression for $d(t)$ and keeping only the contribution relevant to positive frequencies (the conjugate term contributes to negative frequencies), we obtain

$$\begin{aligned} a(\Omega) \approx i \int_{-\infty}^{\infty} dt\, e^{i\Omega t} \int_{-\infty}^{t} dt'\, \vec{E}(t') \int \frac{d^3p}{(2\pi)^3}\, \tilde{d}[\vec{p}+\vec{A}(t)]\, \tilde{d}^*[\vec{p}+\vec{A}(t')] \\ \cdot \exp\left(-i \int_{t'}^{t} \left[\frac{[\vec{p}+\vec{A}(s)]^2}{2} + I_p \right] ds \right). \end{aligned} \tag{1.20}$$

This expression is a multidimensional integral over t, t', and $\vec{p}$. In the strong-field regime, where the ponderomotive energy U_p greatly exceeds the photon energy ω, the integrand oscillates rapidly. The dominant contributions then come from the stationary points of the phase, which can be identified using the saddle point approximation.

The exponent can be rewritten as

$$i\Omega t - i \int_{t'}^{t} \left[\frac{[\vec{p}+\vec{A}(s)]^2}{2} + I_p \right] ds = i\Phi(t,t',\vec{p}), \tag{1.21}$$

with total phase

$$\Phi(t,t',\vec{p}) = \Omega t - \int_{t'}^{t} \left[\frac{[\vec{p}+\vec{A}(s)]^2}{2} + I_p \right] ds. \tag{1.22}$$

The saddle points are given by the stationary conditions $\partial\Phi/\partial t = 0$, $\partial\Phi/\partial t' = 0$, and $\nabla_p\Phi = \vec{0}$ [65, 73]. These correspond to the recombination time t_r, the ionization time t_i, and the canonical momentum $\vec{p}_s$. Assuming linear polarization along z, we can treat the momentum as effectively one-dimensional.

The momentum condition reads

$$\left.\frac{\partial\Phi}{\partial\vec{p}}\right|_{\vec{p}_s} = -\int_{t_i}^{t_r} [\vec{p}_s + \vec{A}(t')]\, dt' = \vec{p}_s(\tau) + \int_{t_i}^{t_r} \vec{A}(t')dt' = 0, \tag{1.23}$$

where $\tau = t_r - t_i$ is the excursion time. The recombination condition is

$$\left.\frac{\partial\Phi}{\partial t}\right|_{t_r} = \Omega - \left[\frac{[\vec{p} + \vec{A}(t_r)]^2}{2} + I_p\right] = 0, \tag{1.24}$$

which expresses energy conservation: the emitted photon energy equals the returning electron's kinetic energy plus the ionization potential. Finally, the ionization condition is

$$\left.\frac{\partial\Phi}{\partial t'}\right|_{t_i} = \frac{[p + \vec{A}(t_i)]^2}{2} + I_p = 0. \tag{1.25}$$

Since $I_p > 0$, this implies a negative kinetic energy at ionization, consistent with tunneling. As a result, both t_i and $\vec{p}_s$ are complex in general.

Expanding the action to second order around $\vec{p}_s$ and evaluating the Gaussian momentum integral produces the prefactor $(\pi/(i\,\tau/2+\epsilon))^{3/2}$. At this stage, the dipole elements are evaluated at the saddle-point momentum, and the accumulated phase is the quasi-classical action $S(\vec{p}_s, t, \tau)$. The resulting expression is [74]

$$\begin{aligned}\vec{d}(t) = \int_0^\infty d\tau \left(\frac{\pi}{i\,\tau/2+\epsilon}\right)^{3/2} \vec{d}^*\big(\vec{p}_s(t,\tau) + \vec{A}(t)\big)\, e^{-i\,S(\vec{p}_s,t,\tau)}\, \vec{E}(t-\tau) \\ \cdot\, \vec{d}\big(\vec{p}_s(t,\tau) + \vec{A}(t-\tau)\big) \;+\; \text{c.c.}\end{aligned} \tag{1.26}$$

Using Eq. (1.26) together with the saddle point equations, one can compute the high-harmonic spectrum, as shown in Fig. 1.2.

The plateau structure is clearly reproduced: harmonic intensities remain nearly constant over a broad range of orders, a feature not captured by perturbation theory. In Eq. (1.26), the $\tau^{-3/2}$ factor reveals that the dipole strength decreases with excursion time, reflecting the spreading of the electron wave packet. This explains why longer driving wavelengths, which increase τ, reduce efficiency. Eventually, the plateau terminates at the cutoff, where the harmonic yield drops sharply. The cutoff energy will be analyzed in the next section.

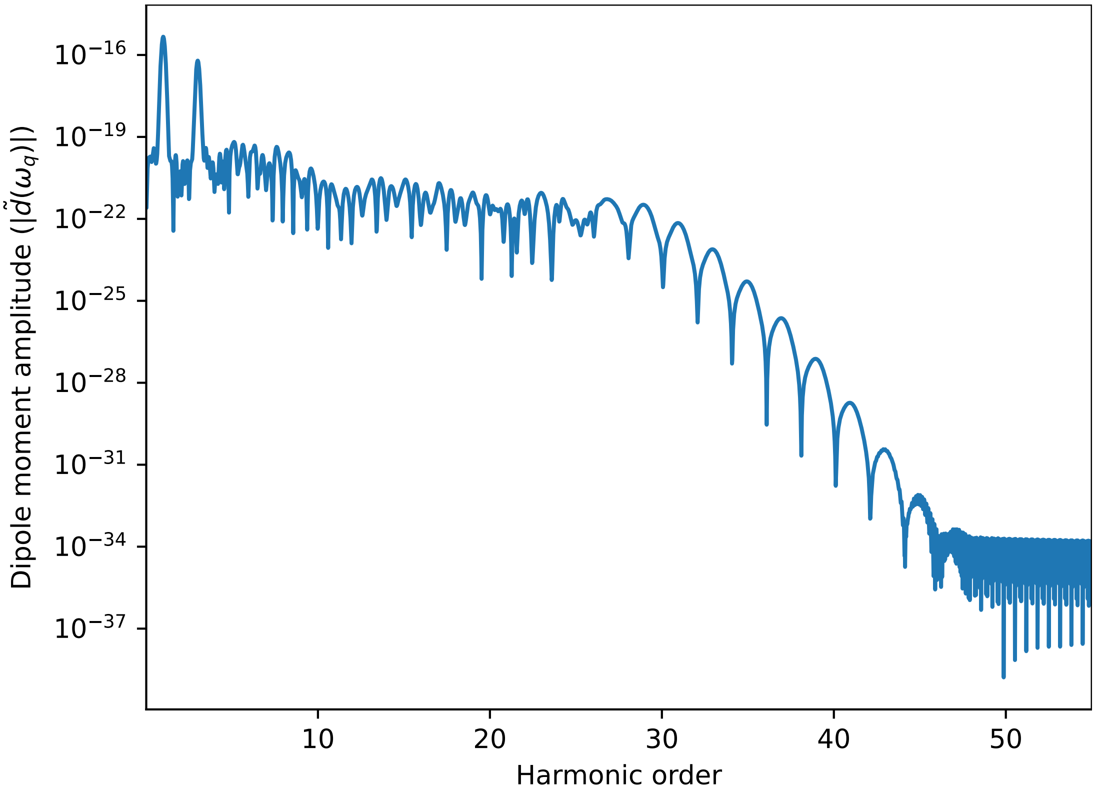

FIGURE 1.2: Simulated dipole spectrum obtained using the saddle-point approximation. The simulation corresponds to the calculations presented in Section 2.3, performed for an argon medium at an intensity of approximately $2 \cdot 10^{14}$ W/cm^2.

Although remarkably successful, the model has known limitations. It assumes that ionization occurs instantaneously at $t = 0$, which is an oversimplification. Furthermore, it describes only the single-atom response, whereas experimentally one measures the macroscopic signal resulting from many emitters. Achieving measurable XUV radiation requires phase matching, a subject addressed in Sec. 1.2.5 and Sec. 1.2.6.

1.2.4 Cutoff law

The cutoff energy in high-harmonic generation can be derived from a saddle-point analysis of the Lewenstein action. Stationarity with respect to momentum enforces that the electron returns to the core, which gives the velocity along the saddle trajectory as

$$\vec{v}(\tau) = \vec{p}_s + \vec{A}(\tau) = \vec{A}(\tau) - \frac{1}{t - t_i} \int_{t_i}^{t} \vec{A}(t')\, dt'. \tag{1.27}$$

Stationarity with respect to the ionization time yields the tunneling condition

$$\partial_{t_i} S(\vec{p}_s, t, t_i) = -\tfrac{1}{2}\left[\vec{p}_s + \vec{A}(t_i)\right]^2 - I_p = 0, \tag{1.28}$$

while the recombination kinetic energy is given by

$$K = \tfrac{1}{2}\big[\vec{p}_s + \vec{A}(t)\big]^2. \tag{1.29}$$

To make the cutoff transparent, one often adopts the tunneling-limit approximation $\vec{p}_s \simeq -\vec{A}(t_i)$, which corresponds to the electron emerging from the barrier with nearly zero initial velocity. In this case the velocity reduces to $\vec{v}(\tau) \simeq \vec{A}(\tau) - \vec{A}(t_i)$, the return condition becomes

$$\int_{t_i}^{t} \big[\vec{A}(\tau) - \vec{A}(t_i)\big]\, d\tau = \vec{0}, \tag{1.30}$$

and the recombination kinetic energy takes the form

$$K(t, t_i) \simeq \tfrac{1}{2}\big[\vec{A}(t) - \vec{A}(t_i)\big]^2. \tag{1.31}$$

For a monochromatic, linearly polarized driver with,

$$\vec{A}(t) = -\frac{E_0}{\omega}\sin(\omega t)\,\hat{\vec{e}}, \tag{1.32}$$

it is convenient to write $A(t) = A_0 \sin(\omega t)$ with $A_0 = E_0/\omega$. The time integral then evaluates to

$$\int_{t_i}^{t} A(t')\, dt' = A_0 \int_{t_i}^{t} \sin(\omega t')\, dt' = \frac{A_0}{\omega}\big(\cos(\omega t_i) - \cos(\omega t)\big). \tag{1.33}$$

Inserting this result into the return condition (1.30) yields

$$\frac{A_0}{\omega}\big(\cos(\omega t_i) - \cos(\omega t)\big) - (t - t_i) A_0 \sin(\omega t_i) = 0. \tag{1.34}$$

After dividing through by A_0 and introducing the phases $\phi = \omega t$, $\phi_i = \omega t_i$, and $\alpha = \omega(t - t_i)$, we obtain

$$\frac{\cos\phi_i - \cos\phi}{\alpha} = \sin\phi_i. \tag{1.35}$$

Substituting this into (1.31) and rearranging (1.35) gives

$$\frac{K(\phi, \phi_i)}{U_p} = 2\big(\sin\phi - \sin\phi_i\big)^2, \qquad \cos\phi - \cos\phi_i + (\phi - \phi_i)\sin\phi_i = 0, \tag{1.36}$$

where $U_p = E_0^2/(4\omega^2)$ is the ponderomotive energy.

Maximizing K/U_p under this return condition yields the well-known result

$$K_{\max} \simeq 3.17\, U_p, \qquad \hbar\omega_{\text{cutoff}} = I_p + K_{\max} \simeq I_p + 3.17\, U_p. \tag{1.37}$$

The cutoff law was first formulated by Krause, Schafer, and Kulander [60], who estimated the maximum photon energy as $I_p + 3U_p$ in 1992. A more accurate value of $I_p + 3.17U_p$ was later obtained independently by L'Huillier *et al.* [75] and by Corkum [59] in 1993.

At longer driving wavelengths, the cutoff scales as,

$$\hbar\omega_{\text{cutoff}} \simeq I_p + 3.17U_p \propto \lambda^2 I, \tag{1.38}$$

since the ponderomotive energy grows quadratically with the laser wavelength λ at fixed intensity I. This quadratic scaling makes it possible to reach much higher photon energies in the mid-infrared regime. However, the single-atom emission yield drops sharply with wavelength, typically as λ^{-5} to λ^{-6} in the tunneling regime, due to the spreading of the electron wave packet over its longer excursion time in the continuum. Consequently, while longer wavelengths extend the cutoff, they reduce efficiency, highlighting the importance of phase matching and macroscopic optimization in high-harmonic generation.

1.2.5 Wave Propagation in a Medium with Absorption

While the microscopic mechanism of HHG—typically described by the three-step model, is well understood, the generation of bright and coherent harmonics suitable for experimental applications relies heavily on the macroscopic phase matching conditions within the generation medium. Macroscopic phase matching refers to the constructive interference of harmonic fields emitted by individual atoms across the length of the interaction region. Achieving phase matching ensures that the generated harmonics add coherently, leading to a significant enhancement in the high harmonic yield.

The total harmonic signal generated in a gas target is determined by the coherent sum of the contributions from all atoms. This summation is strongly affected by the relative phase of the harmonic field emitted at different locations. When these phase differences are small or vary slowly along the propagation direction, the generated field interferes constructively, resulting in efficient buildup of the harmonic intensity. However, if the phase differences are large, destructive interference occurs, severely limiting the observed harmonic yield. Also, as the medium, where HHG occurs, can also absorb the generated XUV radiation.

First, we need to understand wave propagation in an absorptive medium. To analyze how absorption affects the propagation of an electromagnetic wave at the q$^{\text{th}}$-order harmonic, $\vec{E}_q(\vec{r}, t)$, in a dielectric medium, we start from the inhomogeneous wave equation [76] in three spatial dimensions, $\vec{r} = (x, y, z)$. In the time domain, this equation can be expressed as

$$\nabla^2 \vec{E}_q(\vec{r},t) - \frac{n^2}{c^2}\frac{\partial^2 \vec{E}_q(\vec{r},t)}{\partial t^2} = \mu_0 \frac{\partial^2 \vec{P}_{\mathrm{NL}}(\vec{r},t)}{\partial t^2}, \tag{1.39}$$

where $\vec{P}_{\mathrm{NL}}$ is the nonlinear polarization vector, which acts as the driving term for the generation of new frequencies, such as higher-order harmonics. Here, n is the refractive index of the medium, c is the speed of light, and μ_0 is the vacuum permeability.

To simplify the analysis, we separate the temporal and spatial dependencies of the fields. We also assume that the electric field can be decomposed along the three Cartesian axes and select the z-axis as the propagation direction. Since the fundamental laser field propagates with a different phase than the harmonic field, we introduce a phase factor $\exp(ik_1 z)$, where k_1 is the wavenumber of the fundamental field.

In the expansion of the harmonic field and the nonlinear polarization, we have explicitly written both the forward oscillating term and its complex conjugate (c.c.), since the physical field must be real. However, when solving the wave equation, we are usually interested in the propagation of the positive-frequency component of the field. The negative-frequency part, given by the complex conjugate, carries redundant information because it is simply the Hermitian counterpart of the positive-frequency solution.

Therefore, in the standard treatment, one keeps only the terms proportional to

$$\exp(ik_q z - i\omega_q t)$$

and neglects the complex conjugates during the derivation. At the end of the calculation, the full real physical field can always be reconstructed by adding the complex conjugate of the obtained solution.

$$E_q(z,t) = \frac{1}{2} E_q(z) e^{i(k_q z - \omega_q t)} \tag{1.40}$$

and

$$P_q(z,t) = \frac{1}{2} P_q(z) e^{i(q k_1 z - \omega_q t)} \tag{1.41}$$

where $k_1 = 2\pi n_1/\lambda_1$ is the wave number of the fundamental driving field, while k_q denotes the wave number of the q-th harmonic. In order to evaluate the source terms appearing in Eq. (1.39), we proceed by taking the necessary derivatives. First, the temporal derivative of the electric field envelope reads

$$\frac{\partial E_q(z,t)}{\partial t} = \frac{1}{2} E_q(z)(-i\omega_q) e^{i(k_q z - \omega_q t)}, \tag{1.42}$$

and the second-order time derivative becomes

$$\frac{\partial^2 E_q(z,t)}{\partial t^2} = -\frac{1}{2} E_q(z)\omega_q^2 e^{i(k_q z - \omega_q t)}. \tag{1.43}$$

Similarly, for the polarization we find

$$\frac{\partial^2 P_q(z,t)}{\partial t^2} = -\frac{1}{2} P_q(z)\omega_q^2 e^{i(qk_1 z - \omega_q t)}. \tag{1.44}$$

Since we restrict the problem to propagation along the longitudinal direction z, the Laplacian reduces to a derivative with respect to z. The first spatial derivative of the field envelope is then

$$\frac{\partial E_q(z)}{\partial z} = \frac{1}{2}\frac{\partial E_q(z)}{\partial z} e^{i(k_q z - \omega_q t)} + \frac{ik_q}{2} E_q(z) e^{i(k_q z - \omega_q t)}, \tag{1.45}$$

while the second-order derivative becomes

$$\frac{\partial^2 E_q}{\partial z^2} = \frac{1}{2} e^{i(k_q z - \omega_q t)} \left[\frac{\partial^2 E_q}{\partial z^2} + 2ik_q \frac{\partial E_q(z)}{\partial z} - k_q^2 E_q(z)\right]. \tag{1.46}$$

Substituting the time and space derivatives into Eq. (1.39), we obtain

$$\begin{aligned} \frac{1}{2} e^{i(k_q z - \omega_q t)} \left[\frac{\partial^2 E_q}{\partial z^2} + 2ik_q \frac{\partial E_q(z)}{\partial z} - k_q^2 E_q(z)\right] - \frac{n^2}{c^2}\left[-\frac{1}{2} E_q(z)\omega_q^2 e^{i(k_q z - \omega_q t)}\right] \\ = -\mu_0 \frac{1}{2} P_q(z)\omega_q^2 e^{i(qk_1 z - \omega_q t)}. \end{aligned} \tag{1.47}$$

Dividing both sides by $\frac{1}{2} e^{i(k_q z - \omega_q t)}$ and using the relation $k_q = n_q \omega_q / c$, we obtain

$$\frac{\partial^2 E_q(z)}{\partial z^2} + 2i \frac{n_q \omega_q}{c} \frac{\partial E_q(z)}{\partial z} = -\mu_0 \omega_q^2 P_q(z) e^{i(qk_1 - k_q)z}. \tag{1.48}$$

To further simplify this expression, we invoke the Slowly Varying Envelope Approximation (SVEA) [77], which assumes that the second derivative of the envelope is negligible compared to the first derivative, i.e.

$$|\partial_z^2 E_q(z)| \ll |k_q \, \partial_z E_q(z)|. \tag{1.49}$$

Defining the phase mismatch as $\Delta k = qk_1 - k_q$ and using the relation $\mu_0 = (\epsilon_0 c^2)^{-1}$, the equation reduces to

$$\frac{\partial E_q(z)}{\partial z} = i \frac{\omega_q}{2 n_q \epsilon_0 c} P_q(z) e^{i\Delta k z}. \tag{1.50}$$

From Eq. (1.50) we see, that the spatial dependence of the q$^{\text{th}}$ harmonic along the propagation axis is defined by the polarization vector and the phase mismatch, the causes of this mismatch is further elaborated in section 1.2.6. At this stage, we also take into account absorption of the harmonic radiation in the medium. According to Beer–Lambert's law [78, 79], the transmitted intensity decays exponentially with propagation distance:

$$I_q(z) = I_q(0)e^{-\alpha_q z}, \qquad \Rightarrow \qquad E_q(z) = e^{-\frac{\alpha_q}{2}z}\, E_q(0), \tag{1.51}$$

where α_q is the absorption coefficient. To consider the effect of absorption in Eq. (1.50), we modify it in the following manner relying on Eq. (1.51):

$$\frac{\partial E_q(z)}{\partial z} + \frac{\alpha_q}{2}E_q(z) = i\frac{\omega_q}{2n_q\epsilon_0 c}P_q(z)e^{i\Delta k z}. \tag{1.52}$$

Note that, in the absence of a source, the solution of the Eq. (1.52) results the Beer-Lambert law, as it defined in (1.51) Multiplying both sides by the integrating factor $\exp\!\left(\frac{\alpha_q}{2}z\right)$, the left-hand side can be written as a total derivative,

$$\begin{aligned}\frac{\partial}{\partial z}\left[e^{\frac{\alpha_q}{2}z}\, E_q(z)\right] &= e^{\frac{\alpha_q}{2}z}\frac{\alpha_q}{2}E_q(z) + e^{\frac{\alpha_q}{2}z}\frac{\partial E_q(z)}{\partial z}\\ &= i\frac{\omega_q}{2n_q\epsilon_0 c}P_q(z)e^{z(i\Delta k+\alpha_q/2)}.\end{aligned} \tag{1.53}$$

Assuming, that at the beginning of the gas medium there were no harmonics before the interaction, the boundary condition becomes $E_q(0) = 0$. One can assume homogeneity of the medium, resulting a constant nonlinear polarization $P_q(z) = P_q$, and introducing the absorption length as $L_{\text{abs}} = \alpha_q^{-1}$. The absorption length is inverse proportional to the ionization cross-section (σ_q), which can be found in databases and the density of the medium (ρ) which has to be measured, giving the expression as $L_{\text{abs}} = \dfrac{1}{\sigma_q\rho}$. We integrate the propagation equation over a medium of length L_{med}. The macroscopic polarization can be written as the product of the microscopic dipole response and the number density of emitters,

$$P_q = \rho\, d_q, \tag{1.54}$$

where ρ denotes the atomic (or molecular) density and d_q the single-atom dipole moment at harmonic order q.

$$e^{\frac{\alpha_q}{2}L_{\text{med}}}E_q(L_{\text{med}}) = \frac{\omega_q}{2n_q\epsilon_0 c}\rho\, d_q \int\limits_0^{L_{\text{med}}} e^{z(i\Delta k+\frac{1}{2L_{\text{abs}}})}\, dz. \tag{1.55}$$

Carrying out the integration yields

$$E_q(L_{\text{med}}) = i\frac{\omega_q}{2n_q\epsilon_0 c}\rho\, d_q e^{-\frac{L_{\text{med}}}{2L_{\text{abs}}}}\frac{e^{(i\Delta k+\frac{1}{2L_{\text{abs}}})L_{\text{med}}}-1}{i\Delta k+\frac{1}{2L_{\text{abs}}}}. \tag{1.56}$$

To calculate the observable harmonic yield, we consider the harmonic intensity, which is proportional to the square modulus of the electric field:

$$\begin{aligned}\frac{2}{\epsilon_0 c n_q} I_q(L_{\text{med}}) &= \left(\frac{\omega_{\text{q}}\,\rho\,d_{\text{q}}}{2n_{\text{q}}\epsilon_0 c}\right)^2 \frac{\left|e^{i\Delta k L_{\text{med}}} - e^{-\frac{L_{\text{med}}}{2L_{\text{abs}}}}\right|^2}{\Delta k^2 + \frac{1}{4L_{\text{abs}}^2}} \\ &= \frac{\left(\frac{\omega_{\text{q}}\,\rho\,d_{\text{q}}}{2n_{\text{q}}\epsilon_0 c}\right)^2}{\Delta k^2 + \frac{1}{4L_{\text{abs}}^2}} \left|-e^{-\frac{L_{\text{med}}}{2L_{\text{abs}}}} + \cos(\Delta k L_{\text{med}}) + i\sin(\Delta k L_{\text{med}})\right|^2 \\ &= \frac{\left(\frac{\omega_{\text{q}}\,\rho\,d_{\text{q}}}{2n_{\text{q}}\epsilon_0 c}\right)^2}{\Delta k^2 + \frac{1}{4L_{\text{abs}}^2}} \left[1 + e^{-\frac{L_{\text{med}}}{2L_{\text{abs}}}} - 2e^{-\frac{L_{\text{med}}}{2L_{\text{abs}}}}\cos(\Delta k L_{\text{med}})\right].\end{aligned} \tag{1.57}$$

Finally, it is convenient to introduce the coherence length, defined as $L_{\text{coh}} = \pi/|\Delta k|$, which characterizes the distance over which harmonic radiation builds up in a coherent manner. For clarity, we define

$$A_{\text{q}} \equiv \frac{\epsilon_0 c n_{\text{q}}}{2}\left(\frac{\omega_{\text{q}}}{2n_{\text{q}}\epsilon_0 c}\right)^2, \tag{1.58}$$

amplitude, which has units of W/C^2. With this definition, the harmonic intensity can be expressed in the compact form, introduced by Constant *et al.* [80]. This formalism provides a compact way to describe the macroscopic buildup of the harmonic field in an absorbing medium.

$$I_q = A_{\text{q}}\,\rho^2|d_{\text{q}}|^2 \cdot \frac{4L_{\text{abs}}^2}{1 + 4\pi^2\frac{L_{\text{abs}}^2}{L_{\text{coh}}^2}}\left[1 - 2e^{-\frac{L_{\text{med}}}{2L_{\text{abs}}}}\cos\left(\frac{\pi L_{\text{med}}}{L_{\text{coh}}}\right) + e^{-\frac{L_{\text{med}}}{L_{\text{abs}}}}\right]. \tag{1.59}$$

The most important property of this expression (Eq. (1.59)) — and what makes it easy to use it for optimization of harmonic signal — for a given intensity one can find the optimal gas density and medium length. To visualize the result, one can introduce substitutions, which simplify the equation. These substitutions [81]:

$$L = \frac{L_{\text{med}}}{2L_{\text{abs}}}, \qquad R_0 = \frac{2\pi L_{\text{abs}}}{L_{\text{coh}}}, \qquad S_{\text{max}} = A_q\rho^2|d_{\text{q}}|^2 4L_{\text{abs}}^2 \tag{1.60}$$

Substituting these relations gives

$$I_q = S_{max} \cdot \frac{4L_{\text{abs}}^2}{1 + R_0^2}\left[1 - 2e^{-L}\cos(R_0 L) + e^{-2L}\right]. \tag{1.61}$$

The term in the bracket can be written in a simple forms as:

$$\begin{aligned} 1-2e^{-L}\cos(R_0L)+e^{-2L} &= \left(1-e^{-L}\cos(R_0L)\right)^2+\left(e^{-L}\sin(R_0L)\right)^2 \\ &= \left|1-e^{-L+iR_0L}\right|^2 \end{aligned} \tag{1.62}$$

Substituting Eq. (1.62) into Eq. (1.61) yields:

$$I_q = \frac{S_{\max}}{1+R_0^2}\left|1-e^{-L+iR_0L}\right|^2, \tag{1.63}$$

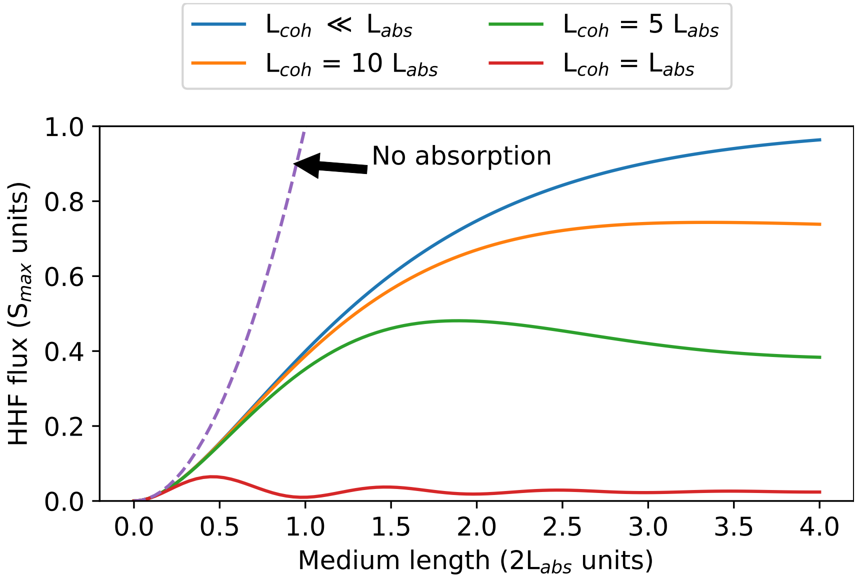

FIGURE 1.3: The harmonic flux normalized to the absorption-limited maximum flux $S_{\max}$ as a function of normalized medium length L for different ratios of the coherence- and absorption lengths, defined by R_0. [82]

Physically, $R_0 = \frac{2\pi L_{\text{abs}}}{L_{\text{coh}}}$ quantifies the relative strength of absorption with respect to phase mismatch. The resulting behavior is illustrated in Fig. 1.3. The dashed line corresponds to the absorption-free limit ($L_{\text{abs}} \to \infty$), where the signal grows quadratically with medium length ($I_q \propto L_{\text{med}}^2$). The other curves represent different phase matching scenarios. The ideal case with $L_{\text{coh}} \gg L_{\text{med}}$, where $R_0 = 0$. In this case, all the generated radiation can be added up coherently and the reabsorption is minimal. Although this is experimentally not feasible, the conditions can be chosen for the near-optimal case, where L_{coh} remains much larger than L_{abs}. The rule of thumb is that $L_{\text{coh}} > 3L_{\text{med}}$ or $R_0 > 2$ [80], in figure 1.3 two of this case had been shown, one with $L_{\text{coh}} = 10L_{\text{med}}$, with $R_0 = 0.62$ and $L_{\text{coh}} = 5L_{\text{med}}$, with $R_0 = 1.25$. When $L_{\text{coh}} \lessapprox L_{\text{abs}}$ optimal phase matching is not possible, resulting in low HHG yield, this represented in Fig. 1.3. This situation can and should be avoided by using this simple model during the design process of a HHG beamline.

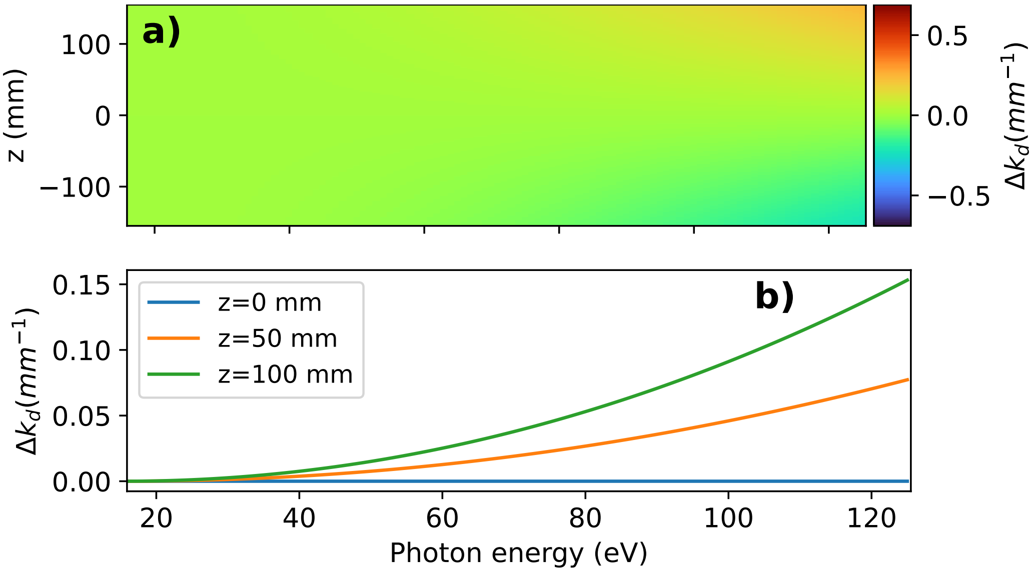

FIGURE 1.4: Calculated dipole induced phase mismatch. Panel (a) shows the z dependence of Δk_d, while (b) shows lineouts for a few selected z values.

1.2.6 Phase matching factors

Obtaining the coherence length L_{coh} is a crucial and relatively complex task, as phase matching depends on multiple factors, and through the relation [83]

$$L_{\text{coh}} = \pi / |\Delta k| \,, \tag{1.64}$$

coherence length also does. The total phase mismatch Δk in Eq. (1.64) is usually written as the sum of four factors [83]

$$\Delta k = \Delta k_d + \Delta k_g + \Delta k_n + \Delta k_p \,, \tag{1.65}$$

representing the phase mismatch due to dipole (Δk_d)- and geometric phases (Δk_g), along with neutral (Δk_n)- and plasma dispersion (Δk_p) [82–84].

The dipole-induced phase mismatch Δk_d can be calculated as the phase (Φ_d) accumulated by the electron in the continuum [84, 85]:

$$\Delta k_d = \frac{\partial \Phi_d}{\partial I(z)} \frac{\partial I(z)}{\partial z} \,, \tag{1.66}$$

with the textbook expression of on-axis intensity variation $I(z)$ of Gaussian beams, giving

$$\Delta k_{d,i} = -\frac{2z\beta_d(z)}{L_R^2 + z^2}, \tag{1.67}$$

where

$$\beta_{d,i}(z) = \alpha_{d,i} I(z) - \frac{\gamma_{d,i}}{I(z)} \left(\omega_q - \frac{I_p}{\hbar} \right)^2 . \tag{1.68}$$

The index i can be representing values belonging to short or long trajectories, α is the polarizability, I_p is the ionization potential, γ for short trajectories equal to 0.22 $cm_e/(\alpha\lambda)$ and -0.19 $cm_e/(\alpha\lambda)$ for the long trajectories and related to the group delay dispersion of the harmonic radiation, λ is the wavelength of the harmonic order, c is the speed of light and m_e is the mass of the electron. It is also important to note, that the $\Delta k_{d,i}$ sign changes before and after the iteration.

Peak intensity of $I_0 = 2 \times 10^{14}\,\mathrm{W/cm^2}$ had been applied and Rayleigh length of L_R =192 mm, both values originating from the experimental conditions detailed in section 2.2.1. For the results in figure 1.4 only the contributions from the short trajectories had been considered, which are usually the dominant one. It is important to note, that after focus (e.g. z=0) Δk_d takes only positive values.

The geometric phase mismatch in high-harmonic generation arises from the focusing properties of the driving laser beam. For a Gaussian beam, this phase variation is governed by the Gouy phase shift, which is defined as

$$\zeta(z) = \tan^{-1} \left(\frac{z}{z_R} \right) , \tag{1.69}$$

where z is the propagation coordinate along the beam axis and z_R is the Rayleigh length [84]. The Gouy phase represents the additional phase acquired by the beam as it passes through the focal region, amounting to a total shift of π radians from $z \to -\infty$ to $z \to +\infty$.

In the context of HHG, variations in the fundamental field's phase directly affect the phase matching between the driving infrared (IR) laser and the generated harmonic field. When considering only the defocusing effect of the IR beam and neglecting contributions from the harmonic beam's divergence, the geometrical phase mismatch can be expressed as

$$\Delta k_g(z,q) = q \frac{d\zeta(z)}{dz} = -\frac{q z_R}{z^2 + z_R^2} . \tag{1.70}$$

Here, q denotes the harmonic order, and the negative sign reflects the fact that the Gouy phase contribution generally opposes perfect phase matching. This term becomes most significant near the focal region, where the derivative $d\zeta/dz$ reaches its maximum magnitude.

Figure 1.5 shows the calculated geometrical phase mismatch Δk_g as a function of propagation distance for different harmonic orders. The results correspond to the HHG process in the HHG1 gas cell described in Section 2.2. As can be seen, higher harmonic orders exhibit proportionally larger geometric phase mismatch, which can strongly limit

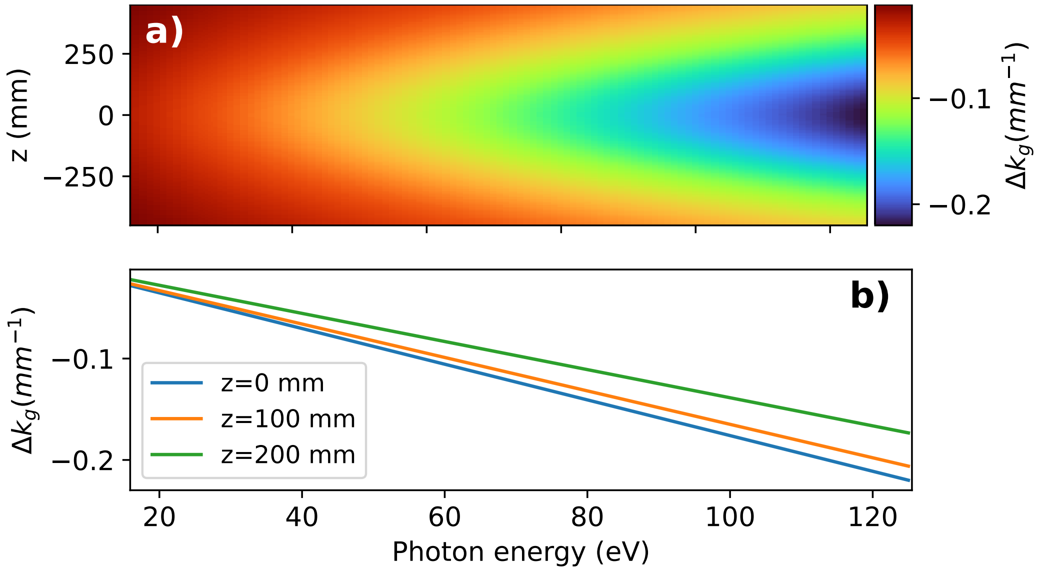

FIGURE 1.5: Geometrical phase mismatch $\Delta k_g(z, q)$ for selected harmonic orders, calculated using the beam parameters of the HHG1 gas cell. The mismatch is largest near the focus ($z = 0$) and scales linearly with the harmonic order q. Panel (a) shows the z dependence of Δk_g, while (b) shows lineouts for a few selected z values.

the coherence length unless compensated by other phase matching contributions such as plasma or neutral gas dispersion. Neutral dispersion also causes phase mismatch, Δk_n, which depends on the refractive index of the generation medium at the wavelength of the generating field and the generated XUV according to Eq. (7) of Ref. [83], that is

$$\Delta k_n = q\frac{\omega_1}{c}(n_1 - n_q)\,, \tag{1.71}$$

Refractive index n_1 for the central wavelength of $\lambda = 840\,\mathrm{nm}$ was obtained from Ref. [86]. In case of XUV photon energies, the refractive index n_q was calculated based on expressions in Ref. [87] using atomic scattering form factors from NIST [88]. In case of both refractive indices $n^2 \approx 1$, n_1 and n_q, it stands that $(n^2 - 1) \sim \rho$ (3.14), or simpler $(n - 1) \sim \rho$ that is their difference from 1, is proportional to the number density.

The resulting phase mismatch is plotted in Figure 1.6 as a function of photon energy for the highest number density involved in this study, $\rho = 2.4 \times 10^{18}\,1/\mathrm{cm}^3$. The ionization — and the plasma generated — is a key factor tuning phase matching through the term Δk_p. This phase mismatch term was calculated using Eq. (8) of Ref. [83], which reads as

$$\Delta k_p = q\frac{\omega_1}{c}(n_1^e - n_q^e)\,, \tag{1.72}$$

defined by the plasma refractive index $n_q^e = \sqrt{1 - N_e/N_c}$, where $N_e = \Gamma\rho$ is the number density of free electrons (Γ being the ionization ratio and ρ the atom number density).

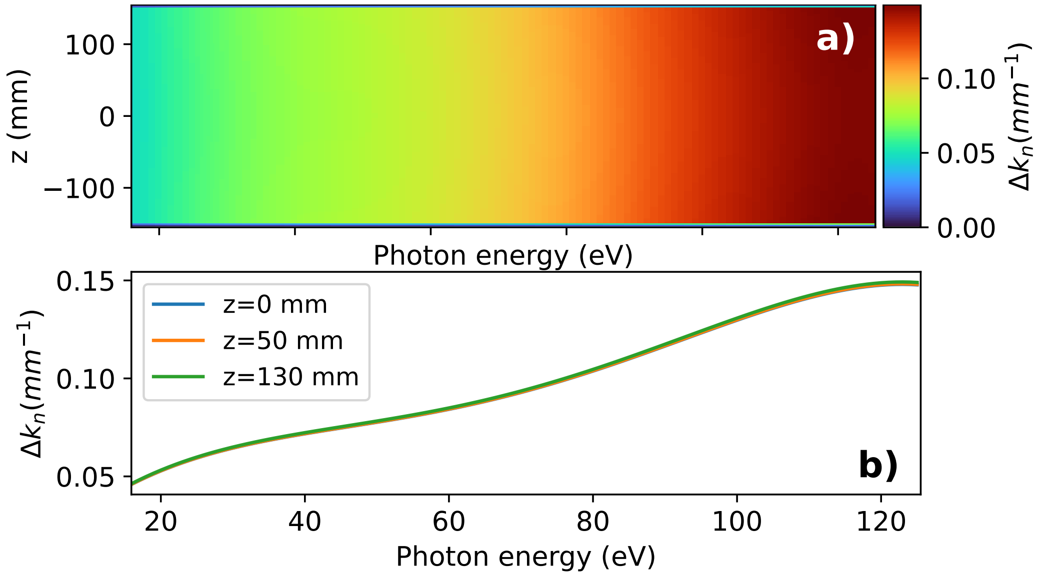

FIGURE 1.6: Calculated phase mismatch due to refractive index of the natural atoms in the medium. As this is not dependent strongly on the z position, all three lines overlap. Panel (a) shows the z dependence of Δk_n, while (b) shows lineouts for a few selected z values.

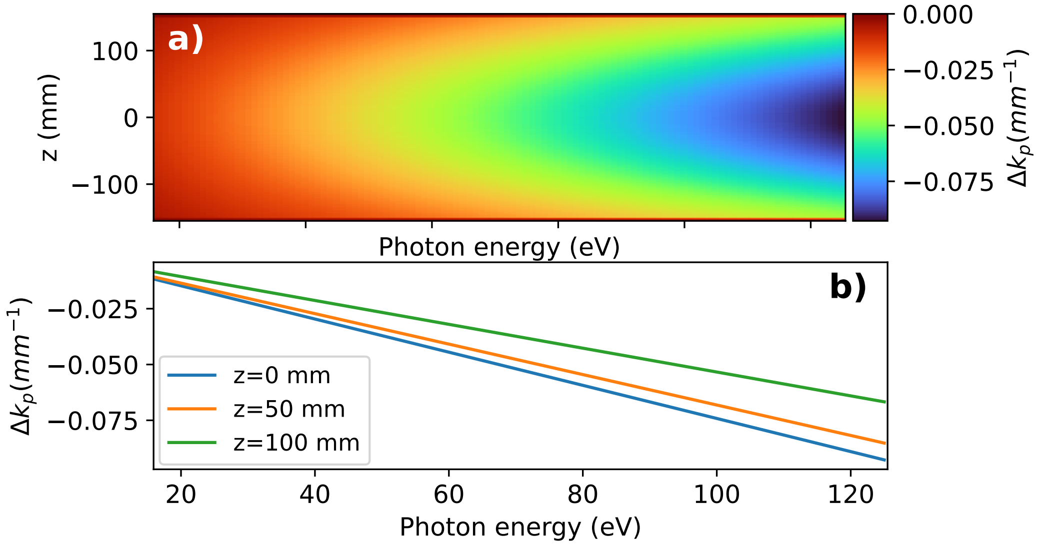

FIGURE 1.7: The calculated phase mismatch arising from free electrons in the medium exhibits its largest negative value at the focus ($z = 0$) where the intensity is highest, and gradually approaches zero at positions farther from the focus, which lies at the center of the gas medium. Panel (a) shows the z dependence of Δk_p, while (b) shows lineouts for a few selected z values.

The photon energy dependence of plasma refractive index appears through the critical density $N_c = \varepsilon_0 m\omega^2/e^2$. The resulting values of Δk_p are plotted in Figure 1.7 as a function of photon energy for $\rho = 2 \times 10^{18}\,1/\text{cm}^3$ density and an ionization ratio of $\Gamma = 5\%$ (this choice of ionization ratio will be explained later). This phase mismatch term is proportional both to density and ionization ratio [82], that is $\Delta k_p \sim \rho\Gamma$ (see

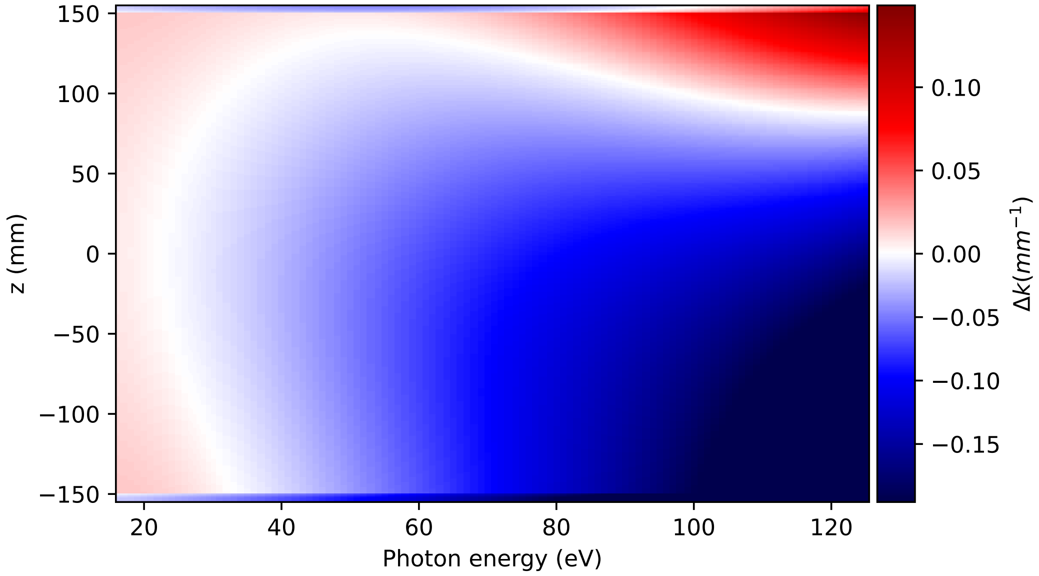

FIGURE 1.8: Calculated total phase mismatch $\Delta k(z)$ for the HHG1 gas cell configuration. The focus is placed at the center of the cell, resulting in favorable phase matching for low-order harmonics at the entrance and for higher-order harmonics near the exit.

explicit expressions for both Δk_n and Δk_p in Ref. [82]). Phase matching in high-harmonic generation is achieved when the total phase mismatch, defined as the sum of all relevant contributions in Eq. (1.65), approaches zero. In this situation, the phase velocity of the generated harmonic field is matched to that of the driving infrared field, allowing the harmonic emission from different positions along the medium to interfere constructively.

The coherence length is inverse proportional to the phase mismatch (Eq. (1.64)), in the special case where $\Delta k = 0$, the coherence length becomes formally infinite, meaning that the generated harmonic field can build up coherently over the entire interaction region without destructive interference. In practice, perfect phase matching is rarely achieved over long distances, but partial compensation of phase mismatch can still significantly enhance the HHG yield.

Figure 1.8 illustrates the spatial dependence of the total phase mismatch $\Delta k(z)$ for the specific configuration where the laser focus is positioned at the center of the gas cell (z=0). Under these conditions, lower-order harmonics are efficiently generated near the entrance of the cell, where the phase mismatch is small and positive, while higher-order harmonics tend to be generated closer to the exit of the cell, where the phase mismatch changes sign and compensates other dispersive effects. This spatial separation of optimal generation zones reflects the interplay between geometric, dispersive, and plasma-induced contributions to the phase mismatch.

The total HHG yield can be calculated using Eq. (1.59), together with the previously defined coherence length. This approach allows us to model different experimental scenarios, the results of which are presented in Section 2.3.

1.2.7 Pressure and length dependence of phase matching

Maximum harmonic generation occurs when $L_{\mathrm{coh}} \gg L_{\mathrm{med}}$, meaning that efficient phase matching is maintained over the entire length of the medium. In contrast, shorter coherence lengths lead to partial destructive interference and thus a reduced yield. When the phase mismatch is very small ($L_{\mathrm{coh}} \gg L_{\mathrm{abs}}$, or equivalently $\frac{\pi}{L_{\mathrm{coh}}} \ll \frac{1}{2L_{\mathrm{abs}}}$, i.e. $\Delta k \to 0$), absorption becomes the dominant limiting factor. In this regime, using the form introduced in Eq. (1.63), the term R_0 vanishes, and the expression simplifies to

$$I_q = S_{\max} \left|1 - e^{-L}\right|^2, \tag{1.73}$$

where $L = L_{\mathrm{med}}/(2L_{\mathrm{abs}})$. As for optimal HHG conditions, $L \ll 1$ the exponential can be expanded into a Taylor series around L=0 (the small absorption limit), we obtain

$$1 - e^{-L} = 1 - (1 - L + \dots) = L - \dots \tag{1.74}$$

and, keeping only the first-order term, the HHG flux can be approximated as

$$I_q = A_q\, \rho^2 |d_q|^2\, L_{\mathrm{med}}^2 \equiv (N_0 L_{\mathrm{med}})^2 \propto (P L_{\mathrm{med}})^2. \tag{1.75}$$

The equation shows that when the pressure is large, the medium length should be short to ensure optimal yield and vice versa. This quadratic dependence on both the pressure and the medium length is the central result discussed in Section 2, where the corresponding simulations and experimental results are presented.

1.2.8 Temporal phase of ultrashort pulses

The temporal form of an electric field can be obtained from the inverse Fourier transform of its spectral amplitude and spectral phase [89]:

$$E(t) = \mathcal{F}^{-1}\left[E(\omega) e^{-i\phi(\omega)} e^{i\omega t}\right]. \tag{1.76}$$

The spectral phase $\phi(\omega)$ can be expanded in a Taylor series around the central frequency ω_0:

$$\phi(\omega) = \phi(\omega_0) + \left.\frac{d\phi}{d\omega}\right|_{\omega_0} (\omega - \omega_0) + \frac{1}{2}\left.\frac{d^2\phi}{d\omega^2}\right|_{\omega_0} (\omega - \omega_0)^2 + \dots, \tag{1.77}$$

where the coefficients of the first and second derivatives introduce important temporal characteristics of the pulse. We define

$$\phi_{GD} = \left.\frac{d\phi}{d\omega}\right|_{\omega_0}, \qquad \phi_{GDD} = \left.\frac{d^2\phi}{d\omega^2}\right|_{\omega_0}, \tag{1.78}$$

which are referred to as the *group delay* and the *group delay dispersion*, respectively.

In general, the center of the temporal pulse envelope and the phase of the carrier wave are not perfectly synchronized. The phase of a short Gaussian laser pulse can be approximated by the carrier-envelope phase (CEP) [90]:

$$\phi_{CEP} = \phi_{GD}\,\omega_0 - \pi_0 - \tfrac{1}{2}\arctan\left(\frac{4\ln 2\,\phi_{GDD}}{\tau_{p0}^2}\right), \tag{1.79}$$

which characterizes the offset between the carrier oscillations and the pulse envelope.

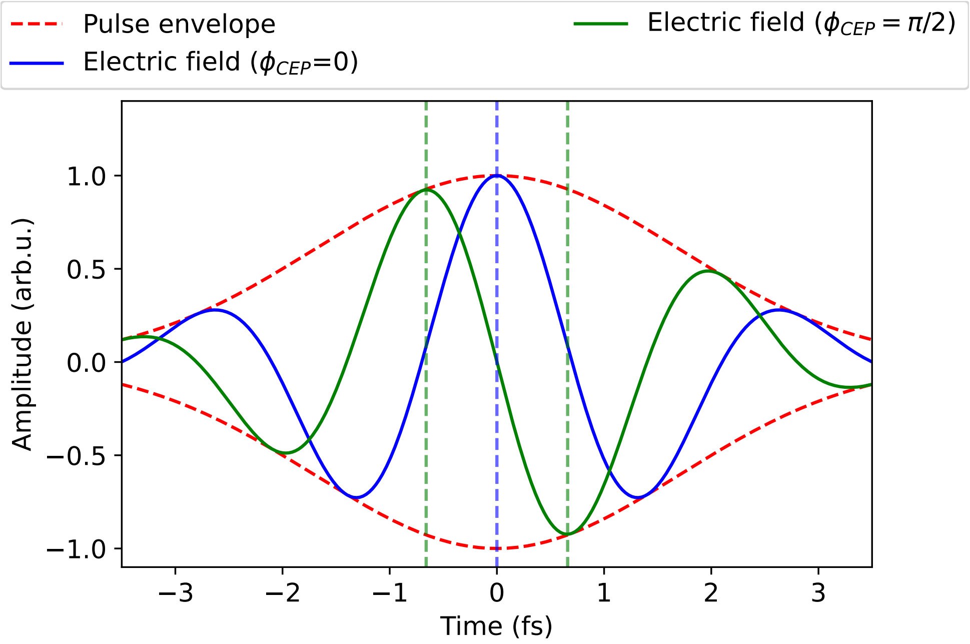

Figure 1.9: Electric field and pulse envelope of a 4 fs pulse shown for two different CEP values. The vertical dashed lines indicate the time at which the electric field reaches its peak for each case.

This phase difference becomes particularly important in the case of few-cycle laser pulses. For instance, in the single-cycle limit, a cosine field ($\phi_{CEP} = 0$) reaches its maximum only once (blue vertical dashed line figure 1.9), whereas a sine field ($\phi_{CEP} = \pi/2$) reaches its maximum twice (green vertical dashed line figure 1.9). Consequently, isolated attosecond pulses can be generated only in the cosine case, making CEP stability a critical requirement for such experiments.

The measurement of the CEP is the central theme of Chapter 4. In this chapter, two techniques are introduced: stereo ATI, which enables absolute CEP measurement, and the f–2f method, which allows tracking of relative CEP variations. Further details on these techniques are provided in Section 4.1.

1.3 Macroscopic phase matching simulation code

To interpret and complement experimental findings in HHG, we carry out detailed large-scale numerical simulations that incorporate the full macroscopic response of the nonlinear medium. These simulations are essential for elucidating the interplay between laser pulse propagation, ionization dynamics, and harmonic generation mechanisms. In particular, they allow us to accurately capture key physical effects such as plasma-induced defocusing, nonlinear refractive index modulation, absorption of both the fundamental and harmonic fields, and phase matching conditions—each of which critically influences the overall efficiency and spectral profile of HHG.

To this end, we utilize a comprehensive three-dimensional (3D) non-adiabatic macroscopic simulation scheme, formulated in accordance with the modeling approaches described in Refs. [81, 91, 92]. This framework enables a time-resolved and spatially resolved treatment of the interaction between the intense driving laser field and the ionizing, cylindrically symmetric, gaseous medium. The simulation evolves through a sequence of three interconnected computational stages. In the initial stage, the propagation of the linearly polarized laser pulse $\vec{E}(\vec{r}_L, t)$ through the nonlinear medium is governed by a modified scalar wave equation that accounts for spatiotemporal variations in the refractive index. The governing equation reads

$$\nabla^2 \vec{E}(\vec{r}_L, t) - \frac{1}{c^2} \frac{\partial^2 \vec{E}(\vec{r}_L, t)}{\partial t^2} = \frac{\omega_0^2}{c^2} \left[1 - n_{\text{eff}}^2(\vec{r}_L, t)\right] \vec{E}(\vec{r}_L, t), \tag{1.80}$$

where $\vec{r}_L$ represents the cylindrical coordinate system aligned along the axis of laser propagation. The effective refractive index $n_{\text{eff}}(\vec{r}_L, t)$ encapsulates both linear and nonlinear contributions and is explicitly defined as

$$n_{\text{eff}}(\vec{r}_L, t) = n + \bar{n}_2 I(\vec{r}_L, t) - \frac{\omega_p^2(\vec{r}_L, t)}{2\omega_0^2}, \tag{1.81}$$

where n is the linear refractive index of the neutral medium, $\bar{n}_2$ is the nonlinear refractive index coefficient (associated with the Kerr effect), and $I(\vec{r}_L, t) = \frac{1}{2}\epsilon_0 c |\tilde{E}(\vec{r}_L, t)|^2$ denotes the instantaneous intensity of the laser pulse, derived from the complex-valued electric field envelope $\tilde{E}(\vec{r}_L, t)$. The plasma frequency ω_p is a function of the local free-electron density $n_e(\vec{r}_L, t)$, given by the relation $\omega_p(\vec{r}_L, t) = \sqrt{n_e(\vec{r}_L, t) e^2/(m\epsilon_0)}$. This formulation allows us to account simultaneously for self-focusing due to Kerr nonlinearity, defocusing induced by plasma generation, and frequency-dependent dispersion. Absorptive losses due to ionization are modeled through time-dependent ionization rates, following the prescription outlined in Ref. [93]. To simplify the numerical treatment of wave propagation, we adopt the paraxial approximation and assume cylindrical symmetry about the propagation axis. By transforming Eq. (1.80) into the frequency domain via a temporal Fourier transform and introducing a co-moving reference frame, we obtain a reduced wave equation of the form

$$\begin{aligned}\left(\frac{\partial^2}{\partial r_L^2}+\frac{1}{r_L}\frac{\partial}{\partial r_L}\right)E(r_L,z_L,\omega)-\frac{2i\omega}{c}\frac{\partial E(r_L,z_L,\omega)}{\partial z_L}\\=\frac{\omega^2}{c^2}\mathscr{F}\left[\left(1-n_{\text{eff}}^2(r_L,z_L,t)\right)E(r_L,z_L,t)\right],\end{aligned}\tag{1.82}$$

where $\mathscr{F}$ denotes the Fourier transform with respect to time. This equation is numerically integrated using an implicit Crank–Nicolson finite-difference scheme, which ensures numerical stability and accuracy over the simulation domain. The initial laser field profile at the entrance of the medium is constructed using the ABCD-Hankel formalism, as described in Refs. [94, 95], which provides an accurate representation of the spatial beam profile under realistic focusing conditions. In the second stage of the simulation, we compute the microscopic response of individual atoms to the local laser field using the well-established Lewenstein strong-field approximation [64]. This model yields the single-atom dipole $D(t)$, from which we construct the macroscopic nonlinear polarization field. To account for ionization-induced depletion of the ground state, we include a damping factor in the macroscopic polarization expression, resulting in

$$P_{\text{nl}}(t)=n_aD(t)\exp\left[-\int_{-\infty}^{t}w(t')\,dt'\right],\tag{1.83}$$

where n_a denotes the neutral atomic number density and $w(t)$ is the instantaneous ionization rate, evaluated using the hybrid antisymmetrized coupled channels (haCC) framework [96]. This method has been benchmarked against standard models such as the Ammosov–Delone–Krainov (ADK) theory [97] and demonstrates consistent accuracy across a wide range of intensities. The final stage involves solving the inhomogeneous scalar wave equation to describe the propagation of the generated high-order harmonics. The harmonic electric field $E_h(\vec{r}_L,t)$ evolves according to

$$\nabla^2E_h(\vec{r}_L,t)-\frac{1}{c^2}\frac{\partial^2E_h(\vec{r}_L,t)}{\partial t^2}=\mu_0\frac{\partial^2P_{\text{nl}}(t)}{\partial t^2},\tag{1.84}$$

where μ_0 is the vacuum permeability. The numerical method used for solving Eq. (1.84) mirrors that of the driving field, with the key difference being the known source term on the right-hand side, which enables direct evaluation of the field response. Propagation in the XUV domain is influenced by dispersion and absorption, both of which are modeled through a complex refractive index. The real component of this index governs the phase velocity of the harmonics, while the imaginary part describes attenuation due to photoabsorption. Material-specific parameters are obtained from tabulated atomic scattering factors [87], ensuring a physically accurate representation of XUV light–matter interactions.

This code was applied in Section 2.3 to study how the high-harmonic flux depends on the pressure and length of the generation medium. In Section 3.9, it was demonstrated that variations in gas density within the medium can lead to noticeable fluctuations in the HHG flux. Finally, in Section 4.2, the CEP dependence of gas high-harmonic generation was investigated for both short and long driving pulses, highlighting how pulse duration influences CEP sensitivity.

1.4 Introduction to HHG in Bulk Solids

High-harmonic generation in solid-state materials has quickly established itself as both a source of ultrafast light and a probe for electron dynamics in condensed matter. While HHG was originally discovered and extensively studied in atomic and molecular gases, extending the process to crystalline solids has opened entirely new avenues in attosecond science, strong-field physics, and materials spectroscopy. When an intense femtosecond or mid-infrared laser pulse interacts with a solid, the nonlinear motion of electrons within the periodic potential of the lattice produces high-order harmonics of the driving field. The first clear demonstration of this effect in a bulk crystal came from Ghimire *et al.* [47], who observed harmonic emission from ZnO driven by mid-infrared pulses. Since that work, solid-state HHG has become a rapidly growing field, offering routes to compact coherent EUV sources, attosecond pulse generation directly from solids, and new tools for ultrafast band-structure spectroscopy.

The microscopic physics of HHG in solids differs [98, 99] in essential ways from the gas-phase case. In gases, the semiclassical three-step model—tunnel ionization, acceleration in the laser field, and recombination with the parent ion—provides a remarkably accurate picture. In solids, however, the collective response of electrons in the periodic lattice potential governs the process, making the band structure, scattering, and interband coherence central to the dynamics. Two mechanisms are usually distinguished: *intraband dynamics*, where electrons undergo nonlinear motion within a single energy band, and *interband transitions*, where electrons excited across the band gap can coherently recombine with their parent holes to emit harmonics. Both contributions are necessary to fully describe HHG in crystals.

A numerical framework for treating this problem was introduced by Plaja and co-workers [100], who solved TDSE on a Bloch-state basis. For a linearly polarized laser field along the optical axis, the system can be reduced to an effectively one-dimensional model. In the velocity gauge, the TDSE takes the form

$$i\hbar\frac{\partial}{\partial t}\left|\psi(t)\right\rangle = \left(\frac{\hat{p}^2}{2m} + V(\hat{x}) + \frac{e}{m}A(t)\hat{p}\right)\left|\psi(t)\right\rangle, \tag{1.85}$$

where $\hat{p}$ is the momentum operator, $V(\hat{x})$ the periodic lattice potential, and $A(t)$ the vector potential of the laser. Because the wavelengths of interest are much larger than the lattice spacing, the field can be treated as spatially uniform within a unit cell, i.e., $A(\hat{x},t) \simeq A(t)$. The vector potential is connected to the electric field by

$$A(t) = -\int_{-\infty}^{t} E(t')dt'. \tag{1.86}$$

The eigenstates of an electron in a periodic potential are Bloch functions,

$$\psi_{\vec{k}}(\vec{r}) = e^{i\vec{k}\cdot\vec{r}}u_{\vec{k}}(\vec{r}), \tag{1.87}$$

with $\vec{k}$ the crystal momentum and $u_{\vec{k}}(\vec{r})$ a lattice-periodic function. Expanding the wave function in this basis [101],

$$\left|\psi_k(t)\right\rangle = \sum_n a_k^n(t)\left|\xi_k^n\right\rangle, \tag{1.88}$$

leads to equations of motion for the band coefficients $a_k^n(t)$. The Bloch states $\left|\xi_k^n\right\rangle$ satisfy the stationary Schrödinger equation,

$$\left(\frac{\hat{p}^2}{2m} + V(\hat{x})\right)\xi\phi_k^n = E_n(k)\left|\xi_k^n\right\rangle, \tag{1.89}$$

where n labels the bands and $E_n(k)$ their dispersion.

The laser–solid interaction generates a macroscopic current density obtained by summing over all $\vec{k}$ values in the Brillouin zone [101, 102],

$$\vec{j}(t) = -\frac{e}{m}\int_{\mathrm{BZ}}\left[\mathrm{Re}\left(\left\langle\psi_k(t)\right|\hat{p}\left|\psi_k(t)\right\rangle\right) + e\vec{A}(t)\right]dk. \tag{1.90}$$

The harmonic spectrum is then given by the Fourier transform of $\vec{j}(t)$. This formalism captures both intraband and interband dynamics and has become a standard microscopic description of HHG in solids.

Although compact, the velocity gauge does not always make the physical roles of the different contributions transparent. The length gauge often provides clearer separation, since the external field couples directly through the dipole interaction:

$$i\hbar\frac{\partial}{\partial t}\left|\psi'(t)\right\rangle = \left(\frac{\hat{p}^2}{2m} + V(\hat{x}) + e\vec{E}(t)\cdot\hat{\vec{r}}\right)\left|\psi'(t)\right\rangle . \tag{1.91}$$

Expanding again in Bloch states,

$$\left|\psi'_k(t)\right\rangle = \sum_n C_k^n(t)\left|\phi_k^n\right\rangle , \tag{1.92}$$

the resulting equations naturally separate into intraband and interband terms. The total macroscopic current can then be written as [103]

$$\vec{j}(t) = \vec{j}_{\text{intra}}(t) + \vec{j}_{\text{inter}}(t), \tag{1.93}$$

with the intraband contribution,

$$\vec{j}_{\text{intra}}(t) = -e\sum_n \int_{\text{BZ}} |C_k^n(t)|^2 \nabla_k E_n(k) dk, \tag{1.94}$$

and the interband contribution,

$$\vec{j}_{\text{inter}}(t) = -\frac{e}{\hbar}\frac{d}{dt}\sum_{n\neq m}\int_{\text{BZ}} C_k^n(t) C_k^m(t)\vec{d}_{nm}(k) dk, \tag{1.95}$$

where $\nabla_k E_n(k)$ is the band velocity and $\vec{d}_{nm}(k) = \langle\phi_k^n|\,\hat{\vec{r}}\,|\phi_k^m\rangle$ the interband dipole matrix element.

This decomposition provides a clear physical interpretation: intraband currents reflect the nonlinear Bloch oscillations of electrons and holes within individual bands, while interband currents arise from coherent electron–hole recombination across different bands. The observable spectrum follows from the Fourier transform of the total current,

$$S(\omega) \propto \left|\int dt e^{i\omega t}\vec{j}(t)\right|^2 , \tag{1.96}$$

with lower-order harmonics typically dominated by intraband dynamics and the plateau–cutoff region shaped by interband recombination.

The properties of solid-state high-harmonic generation are the central focus of Chapter 4, and a key aspect of this topic is understanding the mechanisms by which interband and intraband harmonics are generated. In this context, the effects of the CEP on the solid based HHG yield are also illustrated through simulations. These simulations, while providing valuable insight into the underlying physics, fall outside the scope of this thesis and are therefore only discussed in a supporting role.

Chapter 2

High Harmonic generation yield dependence on medium length

2.1 Phase matching consideration for HHG beamlines

The design of a beamline for laser-driven HHG requires careful consideration of several parameters, particularly when aiming for optimal conversion efficiency. One of the foundational approaches in this process involves the application of scaling laws to estimate and refine experimental conditions that maximize harmonic yield [83, 104, 105]. Typically, the properties of the driving laser—such as pulse duration, central wavelength, repetition rate, and energy—are predetermined. Therefore, the optimization strategy must revolve around achieving the appropriate intensity at the focal point, which lies within the range that supports efficient HHG.

While theoretical models, such as the Lewenstein model, provide useful predictions regarding the single-atom response and optimal laser intensity, practical implementations must also account for macroscopic propagation effects. Among these, phase matching plays a critical role in determining the total harmonic output, as it governs the coherent buildup of the generated harmonics along the propagation axis. Phase matching in gaseous media is influenced by several parameters, including gas pressure, interaction length, focusing geometry, and ionization-induced dispersion. Recent advancements in the analytical treatment of these effects have led to the development of comprehensive phase matching models. In particular, the work by Weissenbilder *et al.* [84] provides an analytical framework that highlights the existence of phase matching conditions not as isolated points, but rather as continuous loci—specifically, hyperbolic curves—within the parameter space of gas pressure and medium length. This model reveals that for a given driving laser intensity, multiple pressure-length combinations exist along a hyperbola that result in comparably efficient phase matching, thereby allowing experimental flexibility.

The key expression derived for phase matching optimization is given by [84]:

$$(p - p_0)\, L_{\mathrm{med}} = \frac{\zeta k_{\mathrm{B}} T f_{\mathrm{i}}}{\sigma_{\mathrm{abs}}}, \tag{2.1}$$

where

$$f_i = \frac{z_R^2}{z^2 + z_R^2}\left(1 + \frac{2z\beta_i(z)}{q z_R}\right) \tag{2.2}$$

Here L_{med} denotes the medium length, p is the gas pressure, p_0 represents the minimum pressure for phase matching at zero ionization, $\zeta \approx 3$ is a fit parameter, which depends on the coherence length, k_{B} is the Boltzmann constant, T is the gas temperature, f_{i} is a correction factor accounting for ionization-induced phase mismatch, and σ_{abs} is the absorption cross-section of the medium. The $\beta_i(z)$ is defined as Eq. (1.68), which depends on the intensity and central wavelength of the laser and the ionization potential of the atom. The term p_0 itself can be expressed as:

$$p_0 z_R = \frac{2\epsilon_0 c k_B T f_i}{\omega(\alpha_0 - \alpha_q)}, \tag{2.3}$$

where z_R is the Rayleigh range, ϵ_0 is the vacuum permittivity, c is the speed of light, ω is the laser angular frequency, and α_0, α_q are the dispersion coefficients of the fundamental and harmonic frequencies, respectively.

According to these equations, one can achieve similar HHG efficiency using a high pressure gas jet with short medium or low pressure long gas cells. However, it is not possible to get any spatial information from this model, which is an important factor to reach to smallest XUV focal size possible and consequently highest XUV intensities in the interaction region.

To validate these theoretical predictions, a collaborative experimental campaign was conducted with a research group from Lund University. The primary objective of this experiment was to empirically map the phase matching behavior and evaluate the pressure-length hyperbolic relationship predicted by the analytical model. Our specific contribution to the project involved the comprehensive preparation, alignment of the experimental apparatus and the execution of the measurements, including the gas delivery system, vacuum chamber, beam-focusing optics, and diagnostic tools. The experimental setup and methodology are described in detail in this chapter, along with the results obtained from the user experiment. These findings provide further insight into the practical applicability of the phase matching model and offer guidance for future optimization of HHG sources in laboratory-scale and facility-level environments.

2.2 Experimental results

The experimental measurements were conducted using the SYLOS GHHG Long beamline [106], located at the ELI ALPS [107–109] research facility. This state-of-the-art beamline was conceptualized and designed by the research group led by Anne L'Huillier at Lund University. As conversion efficiency, the ratio of the IR pulse energy and the generated XUV energy, for gas HHG is low (10^{-5}-10^{-6}), with higher IR energy higher XUV flux can be reached. This is especially important in the case of experiments with isolated attosecond pulses, such as XUV-XUV pump-probe or nonlinear XUV measurement, where high XUV energy is necessary.

An ideal experiment for such beamline would be 2 photon double ionization of atoms in attosecond timescale such as helium, which was conceptualized long ago, but never could be realized. While it shares a foundational design philosophy with the Intense XUV Beamline developed at the Lund Laser Centre [110], the SYLOS GHHG Long beamline has been significantly scaled and adapted to accommodate the operation of high-energy laser systems under two distinct focusing configurations:

- **HHG1:** A 20-meter focusing geometry optimized for use with the SYLOS2 and SEA laser systems, each delivering pulse energies in the vicinity of 30 mJ.
- **HHG2:** A 55-meter focusing geometry designed for the more powerful SYLOS3 laser system, which can operate at pulse energies around 125 mJ.

Due to the need for rapid transitions between these two operational configurations—driven by the high-throughput demands of the user facility—the beamline does not employ conventional spherical mirrors for infrared focusing. Instead, a deformable mirror system is implemented, enabling dynamic adjustment of the focusing geometry without mechanical realignment of optics. Each HHG configuration is equipped with a dedicated gas target system. For HHG1, an adjustable-length gas cell is employed, allowing variation of the interaction length between 32 cm and 72 cm. In contrast, HHG2 utilizes a custom-designed, modular gas cell composed of fifteen individual 40 cm segments, which can be combined to form a continuous interaction region up to 6 m in total length. This modularity offers flexibility in optimizing phase matching and absorption conditions across a range of experimental parameters.

A three-dimensional rendering of the SYLOS GHHG Long beamline layout is presented in Fig. 2.1, providing a visual overview of the infrastructure and experimental configuration. The dark shaded panels list the laser parameters of the two alternative drivers of the beamline, and the cyan panels, at their natural location, indicate the different functional elements of this multipurpose beamline developed at ELI ALPS.

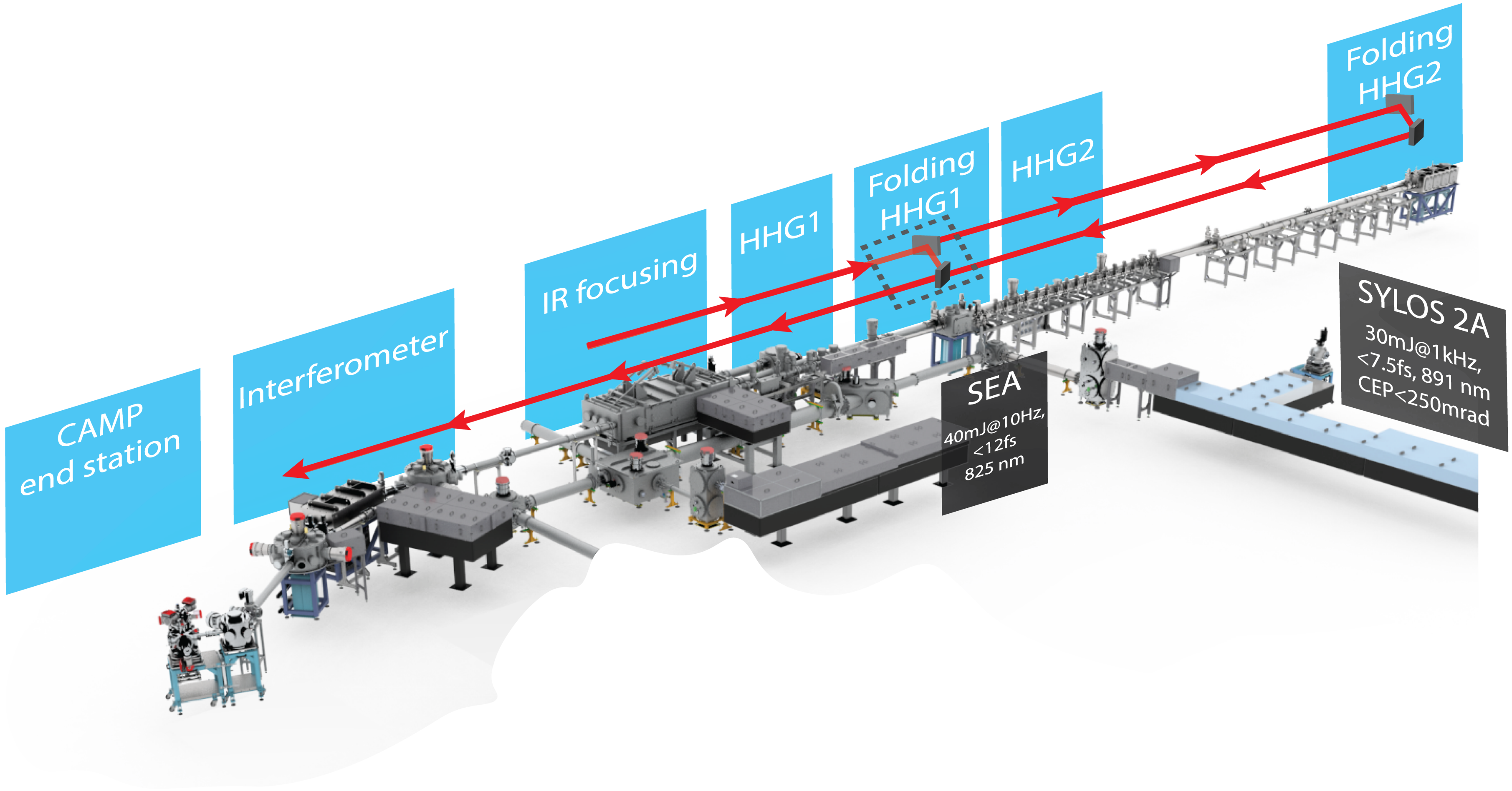

Figure 2.1: SYLOS GHHG Long Beamline at ELI ALPS [111]. High-power IR laser pulses from **SEA**, **SYLOS2A**, or **SYLOS3** are focused using a deformable mirror (**IR**, **focusing**). Two configurations are available: a shorter focusing geometry with an effective focal length of 19 m to the **HHG1** cell, or a longer focusing geometry with a 55 m effective focal length to the **HHG2** cell system. Due to spatial constraints, the beam path is folded by two retro-reflectors in each configuration, denoted as **Folding**, **1** for the short-focus case, where the folding mirrors are marked with a dashed box, and **Folding**, **2** for the long-focus case. For pump–probe experiments, the beam is split in the **Interferometric**, **chamber** using a holey mirror: the XUV beam passes through the center, while the reflected IR beam serves as a reference. After recombination by a second holey mirror, the two beamlets propagate collinearly and are focused into a gas target in the **CAMP**, **chamber** using a Wolter optic system, where the resulting photoelectrons are detected with a time-of-flight electron spectrometer.

To support the experiments presented in this work, as well as related studies, we developed a dedicated gas target chamber, specifically designed to accommodate shorter gas cells and gas jets, as illustrated in Fig. 2.2 (b). This chamber enables flexible testing of various gas target geometries under well-controlled conditions. The gas cell is mounted on a motorized 1-inch mirror mount, which permits fine adjustment of the incidence angle relative to the incoming laser beam. This mount is further integrated into a three-axis vacuum manipulator, allowing precise positioning of the target in the horizontal, vertical, and longitudinal directions with respect to the laser propagation axis.

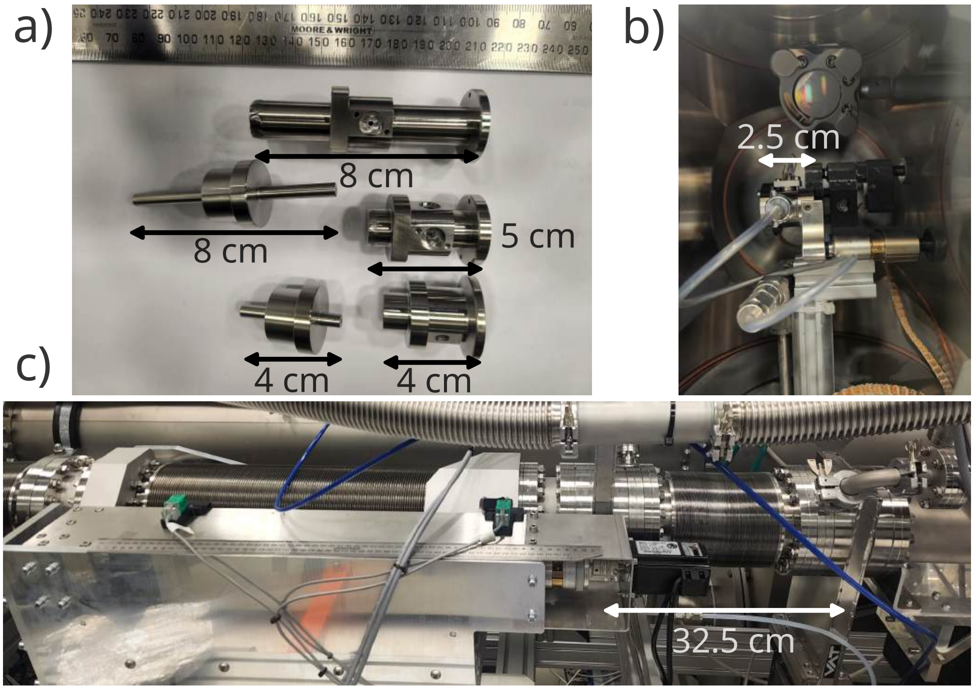

FIGURE 2.2: Different gas cell designs used for high-order harmonic generation in the LONG beamline. Panel (a) shows capillary designs and versions with a gas buffer of 4 cm, 5 cm, and 8 cm, corresponding to 0.17 z_R, 0.21 z_R, 0.34 z_R respectively. Panel (b) depicts an installed gas cell in the beamline, mounted on a mirror holder with tip-tilt adjustment capability. Panel (c) corresponds to HHG1, a variable-length gas cell equipped with a large gas buffer and controllable pressure. This in house developed gas cell is motorized, enabling to optimize medium length between 32 cm to 72 cm, corresponding to 1.6 z_R-3.6 z_R in an automatized way.

The cell, currently installed in the chamber, has an interaction length of 2.5 cm as shown in Fig. 2.2 (b). As the Rayleigh range is around 20 cm for the experiment, this corresponds to 0.1 z_R. For comparative studies, a series of additional gas cells ranging from 4 cm to 12 cm with lengths fabricated and used for HHG, a few of these shown in Fig. 2.2 (a), the 12 cm and the 15 cm long medium was realized, by changing the bellow to a fix length tube in figure Fig. 2.2 (c).

In addition to standard cells design with gas buffer, capillary-type gas cells of 4 cm and 12 cm length were also tested to investigate the influence of different gas distribution profiles on the HHG yield and beam quality. The main difference between the two approaches is the gas density distribution inside the gas medium. As for the analytical model, detailed in section 1.2.6, homogeneous number density was considered, for these experiments we used only buffer type gas cells.

Figure 2.2 (c) depicts the main variable-length gas cell used in the HHG1 configuration. This cell is constructed from two counteracting edge-welded bellow, enabling continuous and stable tuning of the effective cell length. The laser propagates from right to left in the image, and as such, two gate valves are incorporated into the entrance-side bellow to act as both the beam entrance and exit apertures. Both ends of the gas cell are mounted on precision linear translation stages, enabling sub-millimeter alignment with respect to the laser axis. The length of the cell is controlled by a motorized actuator, which facilitates automated scans to optimize the interaction length for maximum high-harmonic output under varying experimental conditions.

The determination of the gas pressure, or more precisely the gas density, in the interaction region of a gas cell presents a non-trivial experimental challenge. This difficulty arises from the fact that, unlike in open-jet or effusive source configurations, where the density can be inferred directly from nozzle parameters and pumping speeds, the confined geometry of a gas cell leads to complex spatial pressure profiles, that are not directly measurable at the point of laser–gas interaction.

In certain beamline designs, particularly those, where the reference infrared IR beam for the pump is separated from the HHG beam prior to the generation stage, it is possible to estimate the local gas density via the phase shift, induced by the gas medium. This is typically achieved by recombining the reference and HHG-driving beams downstream of the generation point and measuring the accumulated phase difference. Such interferometric approaches can yield precise in-situ density measurements; however, in our present experimental configuration, this technique is not feasible due to beamline layout constraints and the absence of a co-propagating reference beam.

In the case of the HHG1 gas cell, shown in Fig. 2.2 (c), a vacuum gauge is installed directly inside the cell volume, enabling a relatively accurate and direct measurement of the local static pressure. This cell is integrated into a system, equipped with a solenoid-controlled valve (Pfeiffer Vacuum RME 005 A), which can operate in a closed-loop feedback mode with the internal gauge. This configuration allows precise pressure control and reproducible pressure scanning during experiments, an essential feature for optimizing phase matching conditions and harmonic yield.

For smaller-volume gas cells, depicted in Fig. 2.2 (a) and Fig. 2.2 (b), direct pressure measurement inside the cell is not possible due to the compact geometry and limited optical access. Instead, the pressure is monitored at two points: in the gas supply line feeding the cell and in the surrounding vacuum chamber, which experiences a small rise in background pressure during operation. From these measurements, the local gas pressure distribution and spatial profile within the cell can be reconstructed using computational fluid dynamics simulations. In our work, this was performed using a SolidEdge-based modeling tool, which accounts for the cell geometry, inlet flow characteristics, and molecular flow regime. The accuracy of this approach depends on both the calibration of the upstream pressure sensor and the fidelity of the geometric model.

In this configuration, gas delivery is controlled via a precision gas dosing valve (Pfeiffer Vacuum EVN 116), which allows fine adjustment of the inlet pressure and, consequently, the density profile inside the cell. While this indirect approach is less precise than in-cell gauge measurements, it provides a reliable means to estimate and control gas density in experimental scenarios where direct probing of the interaction region is not possible. This method has proven sufficient for reproducible HHG measurements and pressure-dependent optimization studies.

2.2.1 IR characterization

During our experimental campaign, we employed the SYLOS Experiment Alignment (SEA) laser system [112], a high-performance ultrafast laser source developed by EKSPLA Ltd with Light Conversion. This system was specifically designed to support experimental alignment and beamline commissioning tasks within ELI ALPS facility, and it closely replicates the operational parameters of the primary SYLOS laser system as described in [113].

The SEA laser delivers pulses with a peak power exceeding 2 TW and a pulse duration shorter than 15 fs, operating at a repetition rate of 10 Hz. These parameters make it well-suited not only for alignment purposes, but also for driving various secondary sources. Notably, the SEA system has been successfully utilized to drive attosecond pulse generation experiments at both the SYLOS GHHG Compact and SYLOS GHHG Long beamlines. Additionally, it plays a critical role in particle acceleration studies, including the Low-Energy Ion Acceleration (LEIA) experiment, which is aimed at laser-based neutron generation. Future applications of the SEA laser are anticipated to include advanced acceleration experiments such as laser-driven wakefield acceleration within the eSylos platform, as well as HHG for surface plasma studies.

The SEA system offers flexible energy tuning capabilities, allowing the pulse energy to be continuously varied between 10 mJ and 35 mJ. Importantly, this variation is achieved while maintaining other key laser parameters constant, such as the pulse duration and

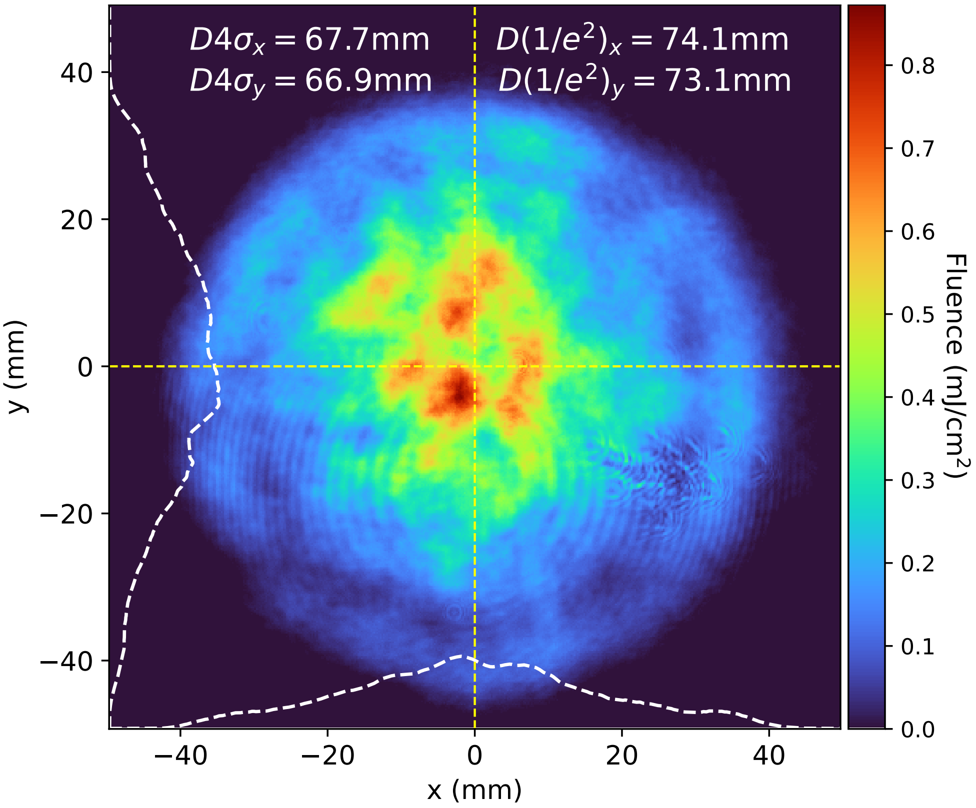

Figure 2.3: Near-field beam profile of the SEA laser, recorded at the entrance of the beamline after beam transport. The color scale indicates the estimated fluence in units of mJ/cm^2, which is an important parameter for assessing and preventing laser-induced damage to the optical components.

beam quality. This feature enables controlled testing and optimization of experimental conditions without introducing unintended variations in pulse characteristics.

A representative beam profile of the SEA laser, acquired during beam transport diagnostics (near-field), is presented in Figure 2.3. To ensure accurate spatial characterization, the system's demagnification was calibrated using a motorized iris aperture of known dimensions. Pulse energies were measured with a calibrated Gentec energy meter head [114], allowing for reliable absolute energy readings.

It is crucial to maintain a relatively large beam diameter throughout the beam transport and at the experimental interaction points. This is done deliberately to reduce the peak fluence on optical components, thereby avoiding damage to mirrors and other sensitive optics used in the beamline infrastructure. The transverse size of the laser beam was determined using two distinct methods, both widely used in laser diagnostics, depending on the shape and quality of the beam. These approaches allow for complementary insight into the spatial intensity distribution and are particularly important when characterizing beams that deviate from ideal Gaussian behavior. The first method relies on calculating the $D4\sigma$, or second moment width, which is defined as four times the standard deviation of the energy distribution in the transverse spatial dimensions. This metric is computed separately in the x and y directions, using the beam's intensity distribution $I(x, y)$. The formula for the $D4\sigma$ diameter is given by:

$$D4\sigma = 4\sigma = 4\sqrt{\frac{\int\limits_{-\infty}^{\infty}\int\limits_{-\infty}^{\infty} I(x,y)(x-\bar{x})(y-\bar{y})\,dx\,dy}{\int\limits_{-\infty}^{\infty}\int\limits_{-\infty}^{\infty} I(x,y)\,dx\,dy}}, \tag{2.4}$$

where $\bar{x}$ and $\bar{y}$ represent the centroid positions in the horizontal and vertical directions, respectively. These are calculated as:

$$\bar{x} = \frac{\int\limits_{-\infty}^{\infty}\int\limits_{-\infty}^{\infty} I(x,y)\,x\,dx\,dy}{\int\limits_{-\infty}^{\infty}\int\limits_{-\infty}^{\infty} I(x,y)\,dx\,dy}, \quad \text{and} \quad \bar{y} = \frac{\int\limits_{-\infty}^{\infty}\int\limits_{-\infty}^{\infty} I(x,y)\,y\,dx\,dy}{\int\limits_{-\infty}^{\infty}\int\limits_{-\infty}^{\infty} I(x,y)\,dx\,dy}. \tag{2.5}$$

This second moment approach is mathematically rigorous and yields reliable estimates for beam diameters, particularly when the beam has a Gaussian profile. However, the method is also sensitive to the energy content in the tails of the intensity distribution. Even low-level noise or background intensity in the peripheral regions of the beam can significantly influence the result, which must be carefully considered when interpreting the measurements.

The second method is based on a more direct and intuitive definition. It involves identifying the points along the beam profile where the intensity falls to $1/e^2$ of the peak value and measuring the distance between these two edges. This diameter is often referred to as the full width at $1/e^2$, and is widely used in experimental setups due to its simplicity and speed. This method is less sensitive to noise in the beam wings compared to the $D4\sigma$ calculation and the evaluation can be done even manually by selecting the points at the corresponding values with simple tools, such as ImageJ [115].

However, this simplicity comes at the cost of precision in certain cases. The $1/e^2$ method assumes a roughly Gaussian or smoothly varying intensity distribution. In cases where the beam exhibits a flat-top profile, hot spots, or irregular structures, this measurement can overlook critical spatial features and yield an inaccurate representation of the beam size. Therefore, while both techniques are valid, the choice between them depends on the specific shape and quality of the beam under investigation, as well as the level of accuracy required for subsequent experiments or beamline alignment.

The beam is pre-compressed using bulk glass elements at the output of the laser system, while the final compression is performed at the beginning of the beamline using chirped mirrors. This configuration is implemented to prevent damage to the beam transport mirrors and to avoid propagating the fully compressed pulse through glass, which

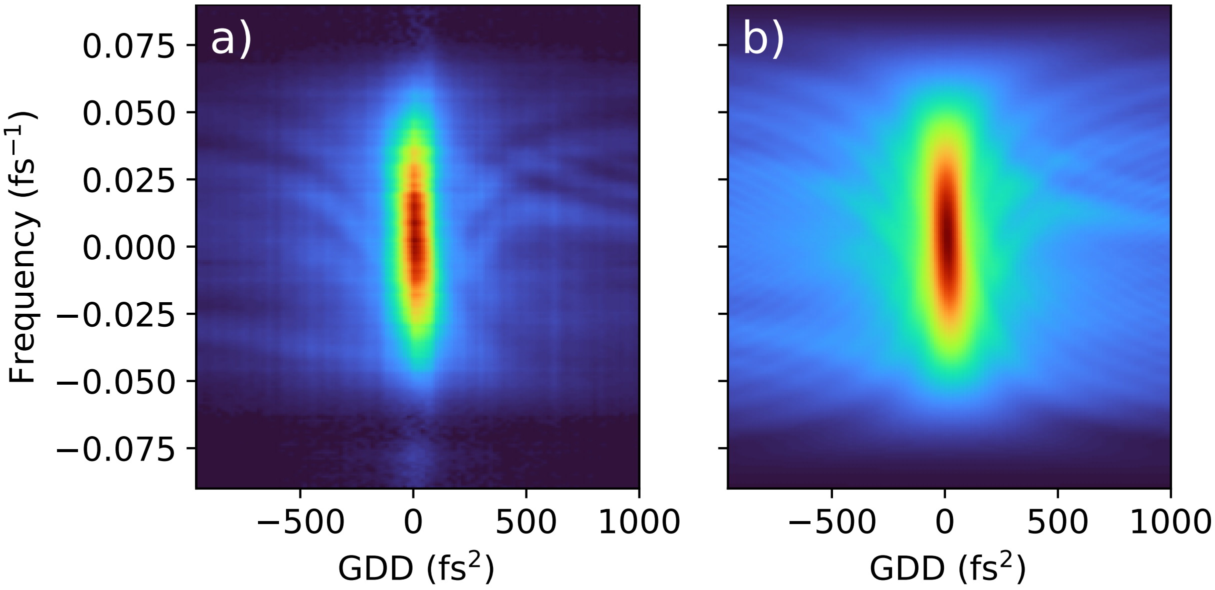

Figure 2.4: Measured (a) and retrieved (b) dispersion scan traces. The dispersion had been modulated by a DAZZLER [116] and the resulted SHG spectra had been recorded with a commercial spectrometer. The retrieval algorithm used is based on the iterative method detailed in [117], when the measured and retrieved traces are matching the spectral phase and the pulse duration can be calculated. The retrieved trace resulting in a pulse duration of 11.8 fs, as it shown later in this chapter.

could lead to undesirable nonlinear effects. To measure the pulse duration of the laser, we used the chirp scan technique [117], which is similar to the dispersion-scan (d-scan) technique [118], a widely adopted and conceptually accessible method for the full characterization of ultrashort laser pulses, particularly in the few-cycle regime. The method is based on the deliberate introduction of a controlled scan of group delay dispersion (GDD) which is equivalent to the introduction of chip in the time domain. By scanning through a well-defined set of GDD values, the input pulse is temporally stretched and compressed in a controlled way, allowing access to its phase structure.

For each imposed chirp value, we generate the corresponding second-harmonic (SH) spectrum by directing the pulse into a nonlinear medium — a 90 µm thick BBO (Beta Barium Borate) crystal — exhibiting second-order susceptibility. These SH spectra, which are highly sensitive to the temporal structure of the driving pulse, are recorded using a spectrometer and constitute the primary dataset for phase retrieval.

The process results in a two-dimensional trace, as shown in Figure 2.4 (a), where each row corresponds to the SH spectrum of a pulse with a specific applied quadratic phase. This trace serves as the input to a numerical retrieval algorithm that reconstructs the spectral phase of the original pulse [117]. The algorithm iteratively minimizes the discrepancy between the measured and simulated SH spectra, yielding both the amplitude and phase of the pulse in the spectral domain (Figure 2.4 (b)). From this information,

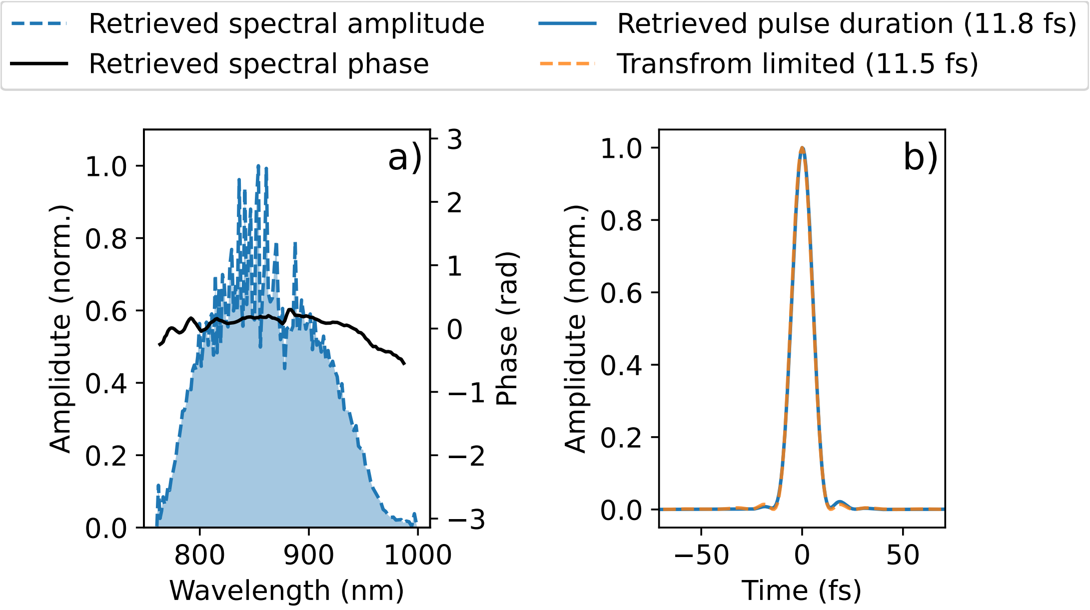

Figure 2.5: Temporal characterization results for the SEA laser. Panel (a) shows the measured spectral amplitude together with the retrieved spectral phase, while panel (b) presents the Fourier-transform-limited pulse compared to the retrieved pulse normalized to 1.

a complete temporal reconstruction of the pulse can be derived, including its spectral amplitude and phase (Figure 2.5 (a)), and temporal profile (Figure 2.5 (b)). This method offers several advantages compared to commercial solutions, as it only requires second-harmonic generation, which can be performed under vacuum. The GDD parameter can be varied using a DAZZLER (an Acousto-Optic Programmable Dispersive Filter developed by FastLite) [116], which is a standard tool for dispersion control in ultrashort laser systems.

To achieve the laser intensities required for high-order harmonic generation, typically in the order of $10^{14}\,\mathrm{W/cm^2}$, a focusing geometry with a focal length of approximately 20 meters is necessary. This focal distance ensures that the beam can be sufficiently concentrated to reach the nonlinear interaction threshold while maintaining a large Rayleigh range, which is beneficial for phase matching and interaction length control.

Such a long focal length can be realized, by directly using a deformable mirror (DM), which serves not only as the focusing optic but also as an active wavefront control element. Unlike conventional spherical mirrors, the deformable mirror offers enhanced flexibility in beam shaping. By dynamically adjusting the mirror surface, it is possible to correct low-order and high-order aberrations introduced by imperfections in the optical system or environmental instabilities. This level of control enables the formation of a near-ideal far-field focal spot with minimal aberrations and improved spatial coherence.

The ability to fine-tune the wavefront using the deformable mirror is particularly advantageous in the context of HHG, where the spatial intensity distribution at focus

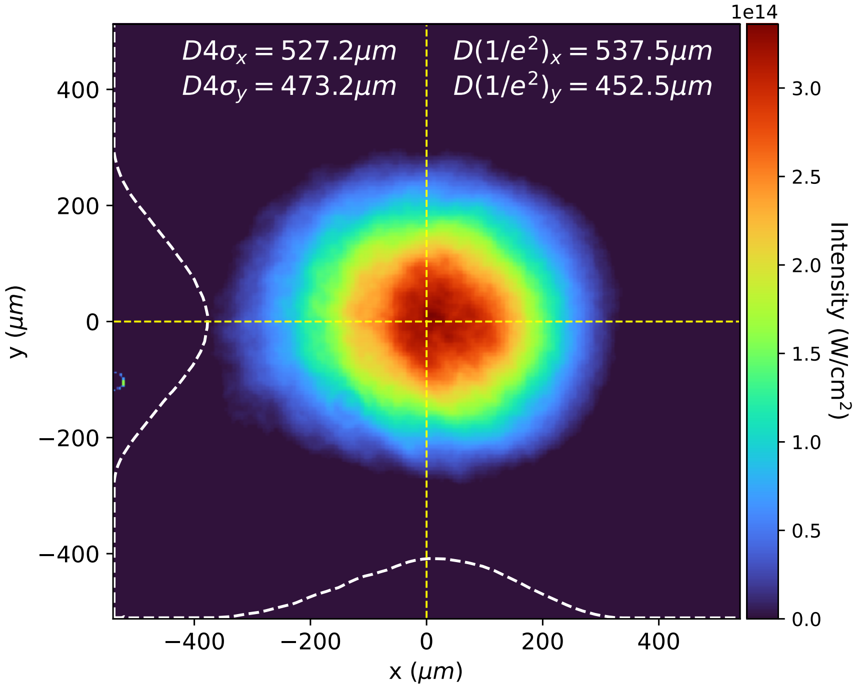

Figure 2.6: Far-field focal spot optimized using the deformable mirror. The intensity is estimated from the measured temporal duration and the measured laser energy.

plays a critical role in the efficiency and spectral quality of the generated harmonics. An example of the resulting focal spot, optimized using the deformable mirror, is shown in Figure 2.6.

This configuration allows for precise control over both the beam divergence and the spatial phase, which are essential parameters for achieving reproducible and efficient harmonic generation. The laser intensity can be reduced accurately with a motorized iris before the deformable mirror by optimizing the generated harmonic signal, as the IR beam is truncated the energy of the IR is reduced and focal spot size is increased at the same time.

2.2.2 XUV characterization

After the high-order harmonic generation process, the residual fundamental infrared beam must be effectively suppressed in order to isolate and transmit only the generated extreme ultraviolet radiation. This filtering is implemented in two stages to ensure high attenuation of the IR while maintaining reasonable transmission or reflectivity in the XUV spectral region.

The first stage of filtering is integrated directly into the beamline and consists of dielectric-coated fused silica plates. These optics are designed such that their reflective coatings significantly reduce the intensity of the residual IR beam, while maintaining

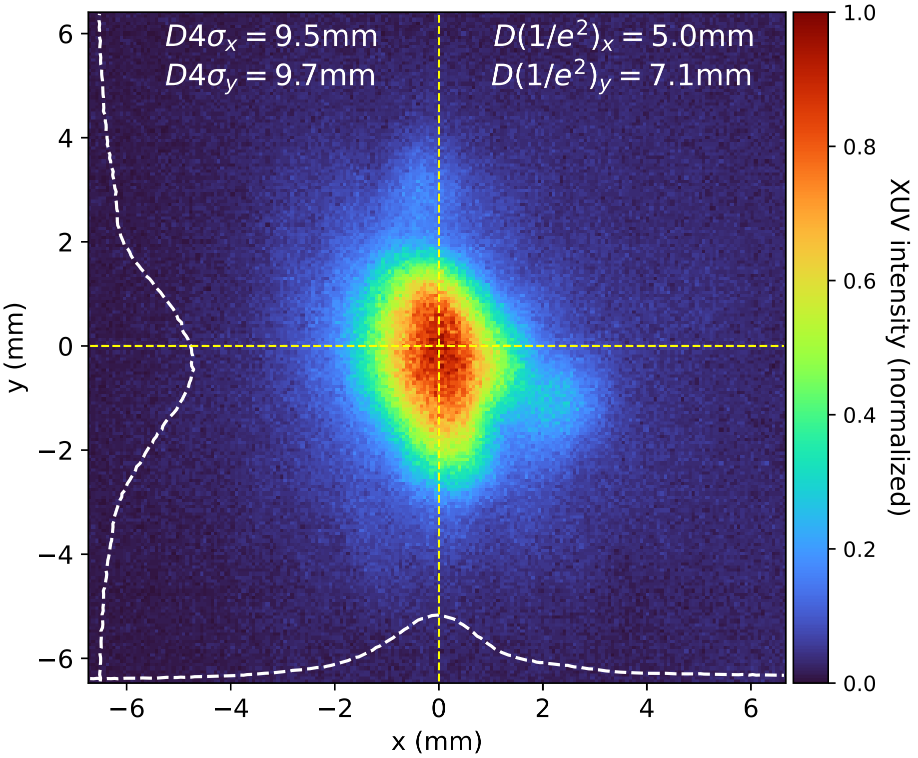

Figure 2.7: Recorded XUV beam profile using a microchannel plate detector and phosphor screen in the Interferometric chamber after 13 meter propagation from the generation point.

a moderate reflectivity—typically around 50%—for the XUV spectral components. This selective reflection relies on the difference in material response and coating behavior across the IR and XUV spectral ranges, allowing for partial spectral separation without the need for transmissive optics that could introduce losses or damage under high-intensity conditions.

To further attenuate any remaining IR radiation, a thin metallic filter is employed downstream. Specifically, a 200 nm thick aluminum foil is used, which acts as an effective high-pass filter for the XUV. At this thickness, the filter provides strong reflection of IR wavelengths while allowing XUV photons—typically in the 16 to 70 eV energy range—to be transmitted with reasonable efficiency. The aluminum filter is supported on a mesh to avoid deformation and maintain stability under vacuum.

The spatial profile of the XUV beam after filtering is shown in Figure 2.7. This profile was recorded using a 25 mm diameter impedance-matched microchannel plate (MCP) detector assembly, consisting of a pair of MCPs coupled to a phosphor screen. The detector used was the BOS-25 model by Beam Imaging Solutions [119], optimized for XUV detection under vacuum conditions. The phosphor screen converts the XUV-induced electron cascade into visible light, which is subsequently imaged using a CMOS camera placed outside the vacuum chamber, observing the screen through an optical viewport.

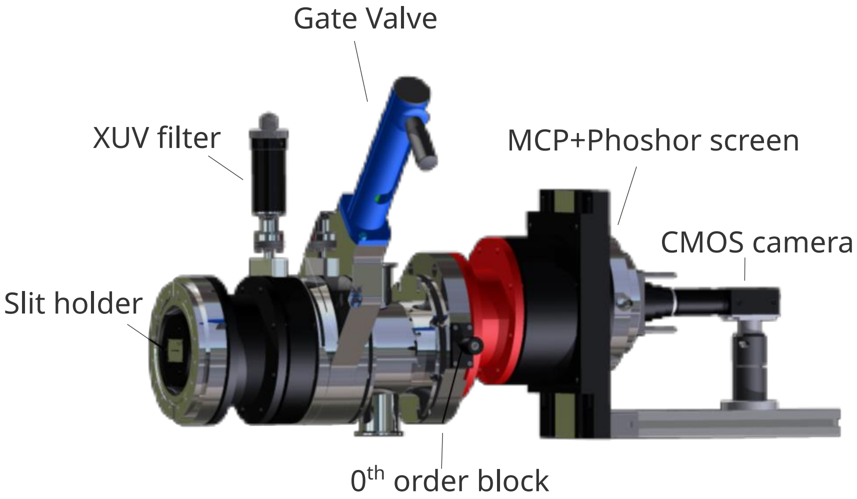

Figure 2.8: Schematic of the XUV spectrometer, manufactured by UltraFast Innovations GmbH, which served as the primary diagnostic tool for the presented experimental results.

The recorded beam profile after free propagation shows its natural divergence and, in the far field, takes on a slightly elliptical shape. This ellipticity suggests a minor degree of astigmatism, most likely arising from the focusing geometry or residual aberrations in the driving infrared beam. Such imperfections can result from off-axis optical elements or uncompensated wavefront distortions introduced before or during the HHG process. Monitoring and analyzing the shape of the XUV beam profile provides important feedback for optimizing the alignment and wavefront quality of the IR beam in future experimental runs.

The spectrum of the XUV beam was recorded using a flat-field grazing-incidence spectrometer, developed at Ludwig-Maximilians-Universität (LMU) in Garching and manufactured by UltraFast Innovations GmbH. The design of the spectrometer enables efficient dispersion and detection of XUV radiation over a broad spectral range, optimized specifically for HHG diagnostics under vacuum conditions.

At the heart of the spectrometer is a concave holographic grating with aberration-corrected geometry, manufactured by Shimadzu Corporation. The grating features a line density of 1200 grooves/mm, and it is designed to operate in a flat-field configuration, which allows measuring linear spatial dispersion of wavelengths along the detector plane. This geometry ensures that the spectral lines are focused in one dimension without requiring additional focusing optics, simplifying alignment, and improving efficiency. The grating provides a dispersion of approximately 1.08 nm/mm and covers a spectral range from 8 to 80 nm, depending on the entrance slit geometry and detector dimensions.

The dispersed XUV radiation is detected using a double-stack MCP detector coupled to a phosphor screen. When XUV photons strike the MCP surface, they generate an electron cascade, which is amplified through the stacked channels, and the resulting electron

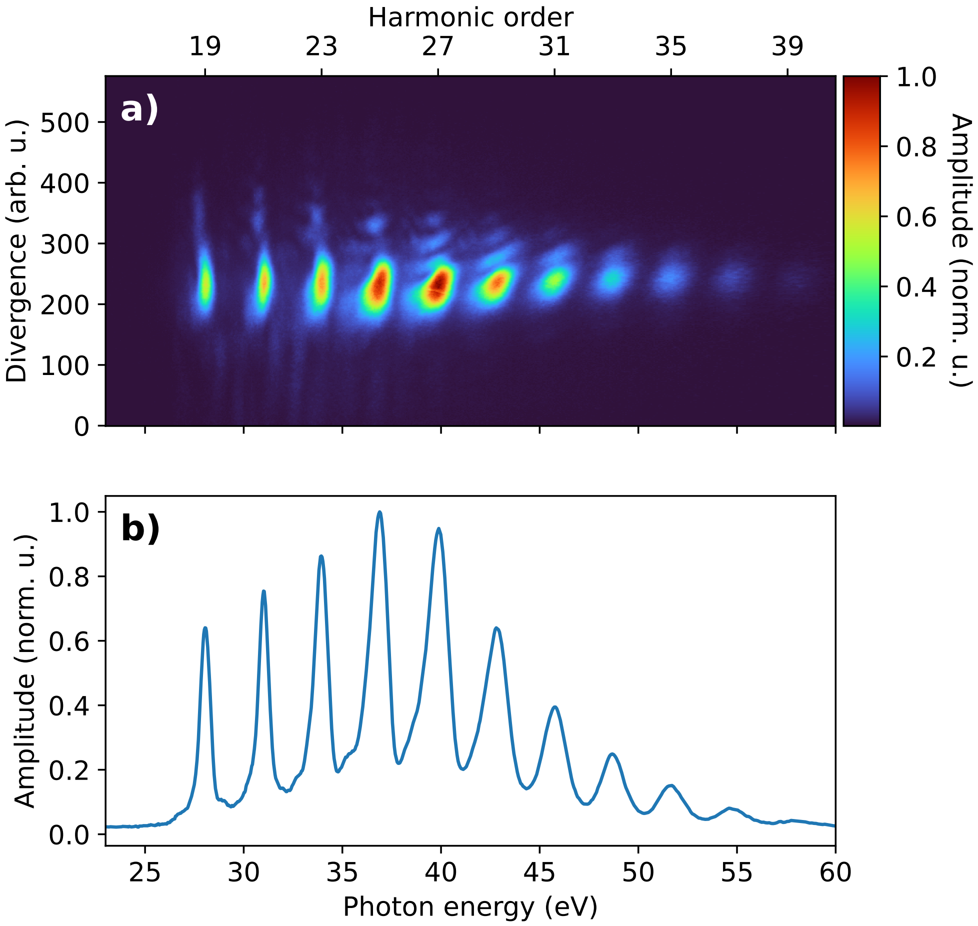

Figure 2.9: High-order harmonic spectrum recorded with the flat-field spectrometer, covering harmonics from roughly the 19th to the 39th order. (a) shows the measured 2D spectrum of the generated XUV light, while (b) presents a line-out taken along its maximum.

signal is converted into visible light by the phosphor screen. This light is then imaged by a CCD or CMOS camera positioned outside the vacuum chamber. The double-stack configuration provides sufficient gain for single-photon sensitivity in the XUV range, making it ideal for low-flux harmonic measurements. The size of the MCP detector defines the effective spectral window that can be recorded in a single acquisition.

Figure 2.9 shows a representative HHG spectrum obtained using the spectrometer configuration described above. The recorded spectrum covers a photon energy range from approximately 25 eV to 60 eV, which corresponds to wavelengths between 20 nm and 50 nm. In this measurement, the harmonic cutoff is observed between the 37th and 39th harmonic orders of the driving laser. This range is in good agreement with the values predicted from the estimated peak intensity of the driving pulse and the phase matching conditions expected under the given experimental parameters.

The two-dimensional spectral image presented in Figure 2.9 (a) reveals that the harmonic lines are not perfectly horizontal, but instead exhibit a slight tilt and distortion.

This effect is caused by an angular chirp in the driving infrared beam, meaning, that different spectral components of the pulse propagate at an angle $\phi(\lambda)$ with respect to the central propagation axis [120]. Such angular dispersion introduces a correlation between wavelength and emission angle in the HHG process, leading to a visible tilt in the harmonic features on the detector plane. After the completion of this measurement campaign, the angular chirp was compensated by introducing a pair of optical wedges into the beam path, thereby removing the residual angular dispersion in the driving pulse prior to HHG.

To compare measurements, one needs to obtain a 1 dimensional spectrum. Usually there are two approaches to this, either integrate the signal along the divergence axis or select a lineout from the distribution. As the harmonics are tilted, the lineout is more representative, considered the optical axis, where the XUV emission is maximal. Hence, we selected the lineout accordingly, represented in Figure 2.9 (b)).

2.2.3 Pressure dependence of HHG

HHG depends on the gas pressure, or more precisely on the number density, in two main ways. First, a higher atom density increases the number of potential emitters. Second, efficient collective emission requires proper phase matching, which is itself pressure dependent. In Section 1.2.6, these contributions are discussed in detail: briefly, the dispersion from neutral atoms contributes positively, while the dispersion from the plasma contributes negatively.

A representative pressure-dependent scan is shown in Fig. 2.10 (a). The spectrum was recorded with a flat-field spectrometer, where each row corresponds to a line-out. The total yield, obtained by integrating the signal, is presented in Fig. 2.10 (b). These results clearly demonstrate that, for a given laser condition (primarily the intensity), HHG exhibits a well-defined optimum pressure for a fixed medium length.

The primary objective of the user experiment was to investigate the dependence of HHG yield on the medium length and gas pressure. To this end, high-order harmonics were generated using gas cells of different lengths, as illustrated in Figure 2.2. Coupling the IR driving beam into the gas cell is a nontrivial task, and in practice, the actual laser energy coupled into the interaction region varies slightly from one cell geometry to another. Consequently, for each cell length, the HHG process was optimized individually to account for these differences. Once optimal conditions for a given gas target were established, a pressure scan was performed in a manner analogous to the procedure described in Section 2.2.3, and the corresponding spectra were recorded.

The MCP detector used in these measurements exhibits a linear response for relatively low photon count rates, as reported in Ref. [121], thereby ensuring, that the recorded data are directly comparable across different experimental runs. The resulting relationship

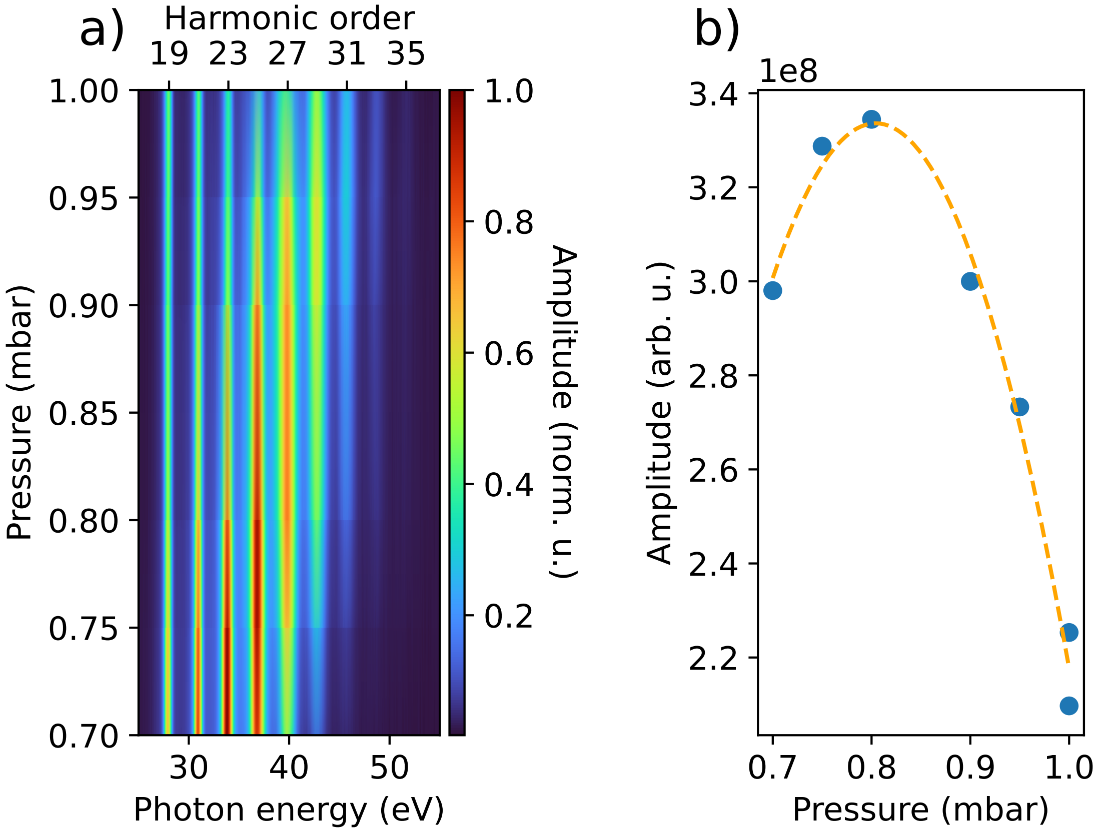

FIGURE 2.10: Measured dependence of the HHG yield on the gas pressure in the generation cell. (a) shows the measured XUV spectrum, while (b) shows the integrated signal.

between HHG yield, gas pressure, and medium length is shown in Figure 2.11, which reveals a characteristic hyperbolic dependence. This measured trend is in good agreement with the theoretical model described by Equation (2.1).

The observed hyperbolic behavior indicates that efficient HHG can be realized under two distinct experimental regimes. The first regime corresponds to a short interaction medium, represented by the vertical branch of the hyperbola, while the second regime corresponds to a long interaction medium, represented by the horizontal branch. At both regimes optimal HHG is possible as similar efficiencies, but in the short medium significantly higher, in our case at least 4 times higher pressure is necessary to ensure optimal phase matching compared to the long cell case.

A detailed theoretical discussion of this phenomenon lies beyond the scope of this thesis; however, it is thoroughly addressed in the work of Weissenbilder et al. [84] and in the associated publication containing the experimental results [P3].

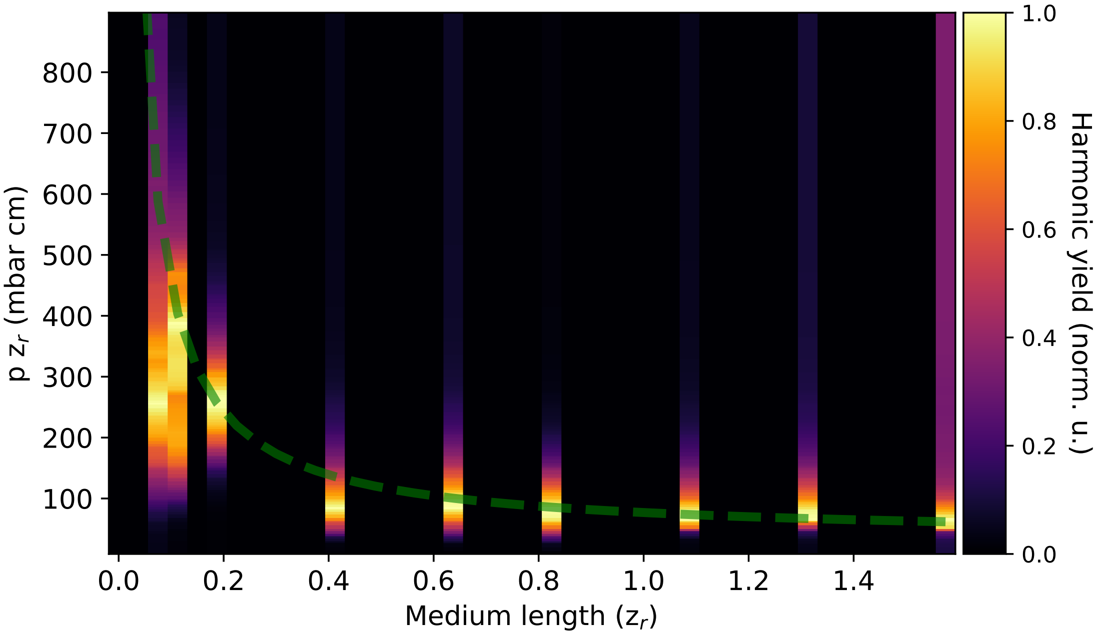

Figure 2.11: Measured dependence of HHG yield of order 27 on medium length in z_R and gas pressure. The measured scans had been normed individually as there are small differences in the coupling into the cells, the crosses showing the maximum yield for each medium length and the dashed line shows the result of the theoretical model given by Equation (2.1).

2.3 Simulated results

Simulations aimed at evaluating phase matching efficiency, which were initially performed by our collaborators from Lund University, using a simplified theoretical framework, as described in Ref. [84]. This model offers a computationally efficient means of estimating optimal phase matching conditions; however, it relies on several approximations and does not incorporate all macroscopic propagation effects—such as nonlinear mode reshaping, plasma-induced refraction, and absorption—that can significantly influence the high-harmonic yield in practical experimental scenarios. One can understand the behavior of the HHG inside gas medium, even by using this model. The description of the method in detail can be found in section 1.2.6.

Simulations were carried out for the two different regimes mentioned in this work. For the long cell case 13 femtosecond long 10 mJ pulse energy laser pulses had been considered at 840 nm central wavelength. To the 32 cm long cell 1 mbar argon gas was maintained.

The resulting HHG output is visualized on figure 2.12. To calculate the resulting strength of the HHG radiation, the Constant model had been used, which is introduced in section 1.2.5 with the coherence length as shown in section 1.2.6. There was an exponential pressure decay considered at the edges of the gas source, although this is not contributing significantly to the result with the long medium.

For the short-medium case, a gas jet was considered with parameters similar to those

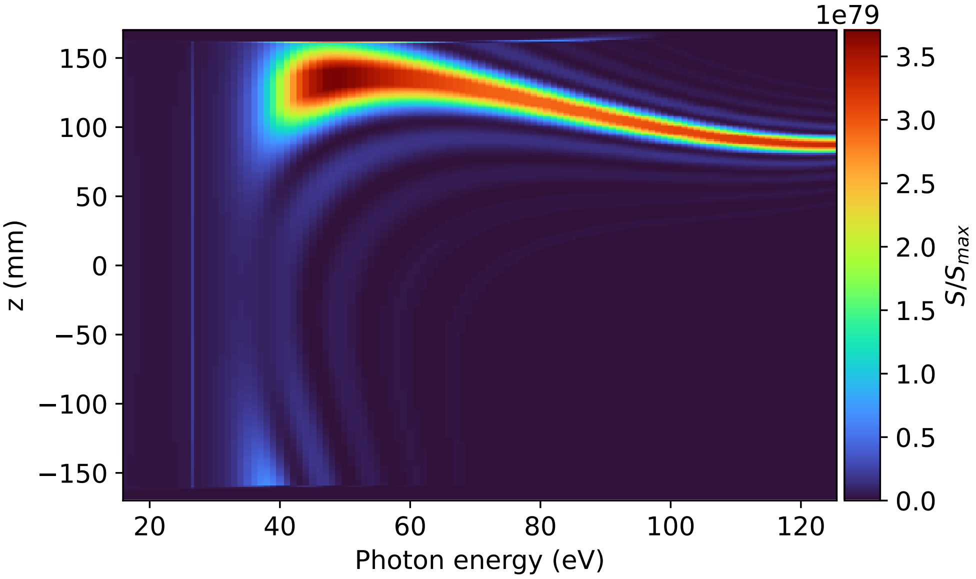

FIGURE 2.12: Simulated high-harmonic yield for a medium length of 300 mm. The plot reveals that harmonics of different wavelengths are not generated uniformly within the cell: lower orders are produced throughout the medium, while higher orders emerge predominantly near the end of the cell.

introduced in Section 3.9. The medium length was approximately 0.5 mm, with a Gaussian gas distribution. In this configuration, a slightly higher driving pulse energy of 13 mJ was used for HHG. The number density in the short-medium case was also significantly higher—about twenty times greater than in the long-medium case—based on the measurements presented in Section 3.6. The simulation was performed for a gas jet geometry, matching the experimental setup described earlier. The resulting HHG flux is shown in Fig. 2.13.

The purpose of these calculations is not to provide an exact quantitative reproduction of the experimental results, but rather to capture the essential qualitative behavior of the process. Even within this simplified framework, the simulations clearly demonstrate that, under optimized generation conditions, the harmonic yield reaches the same order of magnitude for both phase matching regime, as observed experimentally, illustrated in Fig. 2.11. This model helps to understand the underlying principles of phase matching, but to get more accurate results, we have to consider the propagation effects for both the IR and the XUV beams. As this calculation is computationally expensive, and it is difficult to retrieve similar results, the full three-dimensional (3D) macroscopic propagation code, as outlined in Ref. [91] had been used only to validate the hyperbolic behavior, predicted by the Lund group [84].

This more comprehensive approach accounts for the spatiotemporal evolution of the driving laser field and the generated harmonics within the medium, including the effects of plasma formation, dispersion, and nonlinear phase accumulation. The simulated de-

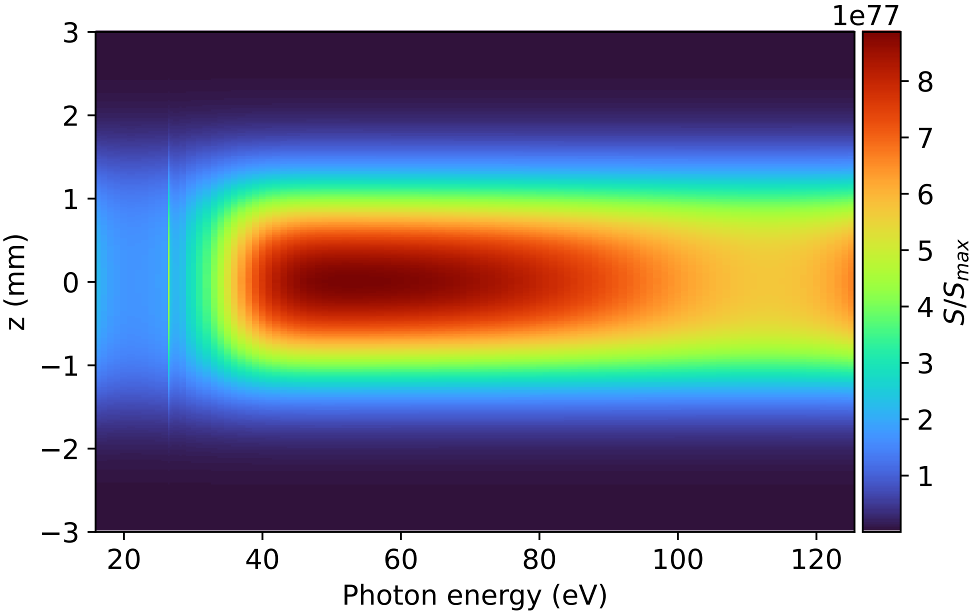

FIGURE 2.13: Simulated high-harmonic yield for a short medium. Under loose focusing conditions, the laser properties remain nearly unchanged across the gas medium, resulting in a uniform generation of all harmonic orders.

pendence of harmonic yield for harmonic order 27 on medium pressure for various gas cell lengths is shown in Fig. 2.14. Due to the significant computational cost associated with this full 3D model, the number of parameter points explored in the simulations was necessarily limited. To optimize resource usage, the simulation grid was chosen such that shorter medium lengths were investigated with higher resolution, while simulations for longer interaction lengths were performed with a coarser sampling of the parameter space, therefore smoothing was applied on the data. Despite these limitations, the results provide valuable insight into the interplay between gas pressure, interaction length, and phase matching conditions in high-harmonic generation. The dashed line shows a hyperbolic curve, similar like on figure 2.11, but the parameters were fitted to the simulation.

A clear difference in the spatial profile of the generated XUV radiation can be also observed, as shown in Fig. 2.15. The simulated near-field profile (Fig. 2.15 (a)) was obtained by combining contributions from orders 13, 19, 21, 31, and 41, whereas the measured profile was integrated over orders 13 to 39 (Fig. 2.15 (b)). In both cases, the lineouts are normalized to the maximum value of each curve. The XUV radiation was measured with an MCP, as described previously in the context of Figure 2.7.

For long cells, the profile remains close to Gaussian. This can be attributed to the off-axis emission, which is predominantly driven by long trajectories and becomes increasingly divergent as the laser intensity rises. This behavior is particularly relevant for pump–probe measurements, since a Gaussian beam can be focused to a smaller spot size with the same focusing geometry, thereby enhancing the intensity.

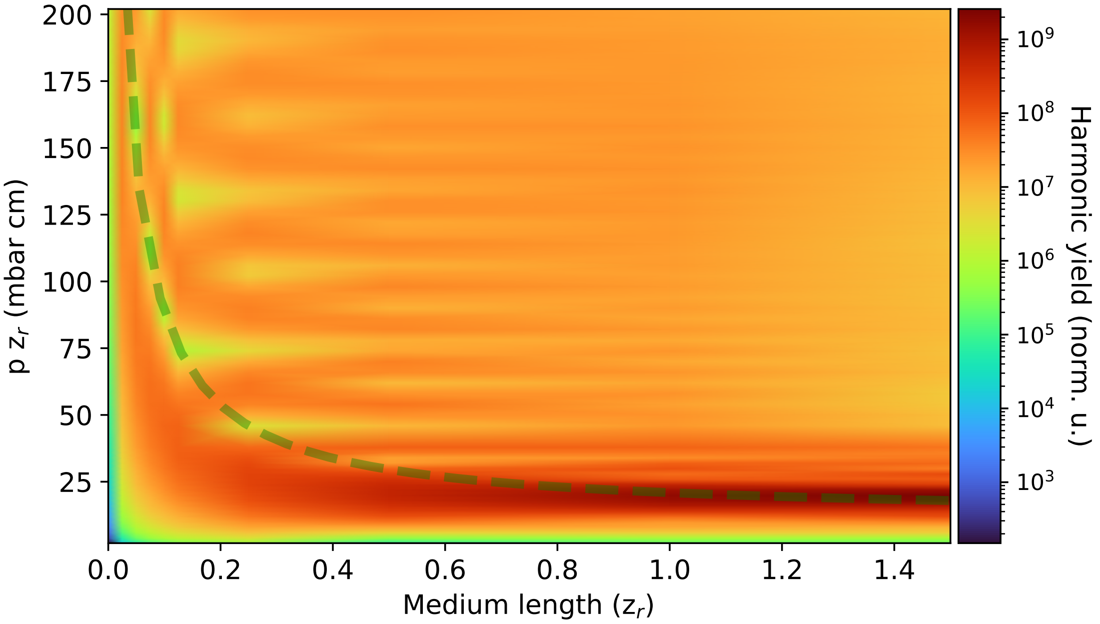

FIGURE 2.14: Simulated high-harmonic yield for the 27th order as a function of medium length and pressure. Because of the lower sampling rate, a smoothing function was applied to the spectra. The green dashed line represents the analytical approximation of the optimal curve.

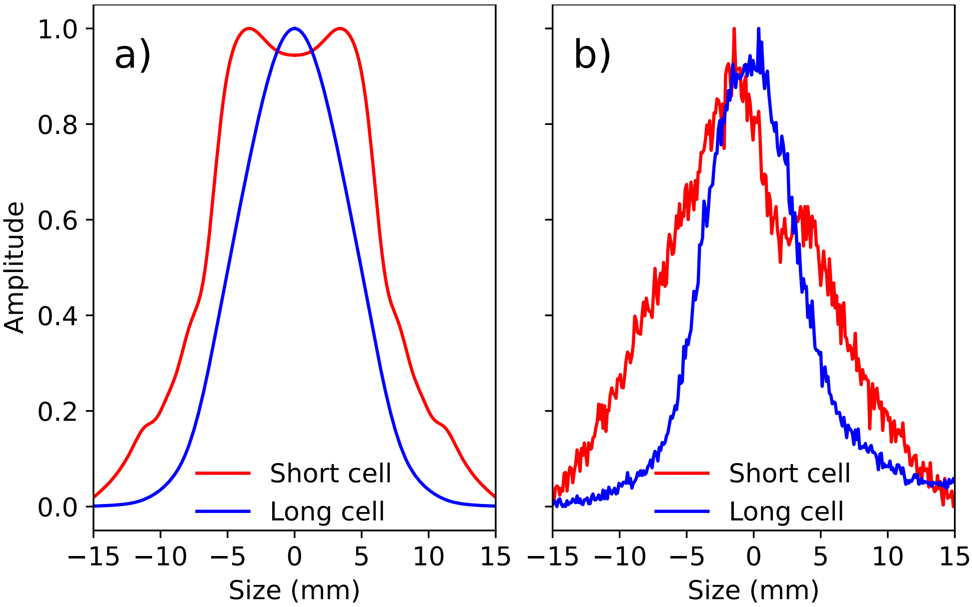

FIGURE 2.15: Spatial distribution of simulated harmonics (a), and a lineout of the measured harmonic profile across the full bandwidth (b). In both panels, blue corresponds to the long cell (1.5 z_R), while red corresponds to the short cell (0.1 z_R).

In contrast, for short cells both short and long trajectories contribute, leading to a degradation of beam quality at higher intensities [122]. The resulting reduction in XUV intensity can, however, be compensated by tighter focusing when high intensities are required, such as in XUV–XUV pump–probe experiments. Furthermore, in short media the IR beam is focused more tightly during HHG, which produces a smaller XUV source. This, in turn, enables the generation of particularly small XUV focal spots for certain applications [123].

The comparison between the experimental results, the predictions of the simplified analytical model and the outcomes of the macroscopic numerical simulations demonstrate a strong qualitative agreement between the two theoretical approaches. Both the simplified model and the full macroscopic code reproduce the observed trends in HHG yield as a function of medium length and gas pressure, capturing the essential features of the dependence and the transition between the short- and long-medium regimes, as similar level of conversion efficiency can be achieved with both high pressure gas jets and low pressure gas cells. This agreement provides confidence in the applicability of the simplified model for rapid estimations and conceptual understanding, while also confirming the accuracy and reliability of the macroscopic simulation framework for detailed quantitative predictions under experimentally relevant conditions.

2.4 Summary

T1 Part of the results presented in this thesis point were obtained during a user experiment with a research group from Lund University, investigating the dependence of high-order harmonic generation on medium length and gas pressure. For this experiment, I prepared the beamline and ensured that all subsystems were operating under optimal conditions. I characterized both the temporal and spatial properties of the driving infrared pulse and measured the characteristics of the generated XUV radiation. I optimized the generation conditions for the selected gas targets by adjusting the alignment, focusing geometry, and gas pressure. I also assembled, installed, and configured the gas cells, making sure they were suitable for the required medium lengths and buffer gas conditions. As part of the preparation, I performed preliminary measurements to verify the stability and performance of the setup. During the experimental campaign, I actively assisted the users with their measurements and supported them in analyzing and interpreting the recorded data.

The results confirm that there is an equivalence in terms of HHG yield between a short high pressure and a long low pressure medium. This predicted hyperbolic behavior of the medium length-pressure dependence had been confirmed. The model is not too sensitive to the laser intensity, which also confirmed by the measurements, since without it, it would have been difficult to tackle the issue with the energy loss due to the coupling of the laser beam into the cell between the different experimental cells. The difference between the XUV beamprofile in different medium length was also confirmed.

These findings are important during the designing phase of a new HHG beamline. When the XUV beam profile is not important as the high flux of photons, short high pressure jets has the advantage. Also, these are easier to implement compared to the generation in gas cell to loose focusing condition, and it can be the better choice when the laser energy is lower. The advantage of using long gas cells is that the XUV beam quality is better, and it is less sensitive to the pressure changes in the gas jets, and it is easier to implement a stable generation medium. This result had been published at [P3].

Chapter 3

Characterization of gas jet for High harmonic generation

The landscape of laser-based applications continues to evolve rapidly, propelled by groundbreaking advancements, such as laser wakefield acceleration of electrons and the generation of attosecond pulses through HHG. Both of which are now being achieved at high repetition rates. In these cutting-edge demonstrations, continuous gas cells have served as the primary medium for interaction; however, they present inherent limitations in terms of accessible gas density due to the accumulation of residual gas within the vacuum chamber, which can hinder performance and scalability. A promising solution to this challenge lies in the implementation of high repetition rate gas jet targets equipped with carefully designed nozzle geometries, which allow for more precise control over gas density and spatial profiles. There are several advantages to pulsed jets, as the gas release takes place for a few µs in every event, it is consuming less gas, while creating high gas densities in the interaction zone. This can reduce the cost, while using expensive targets and needing less amount of samples to synthesize. Another advantage is the lowered risk of handling toxic or flammable gas targets. As less amount of gas enters the vacuum environment, the vacuum system can be simpler and less powerful vacuum pumps can handle the gas load, compared to a gas cell or a continuous stream. While pulsed valves capable of operating at very high pressures and gas densities have been successfully demonstrated, they typically function at relatively low repetition rates.

Accurate metrology of the gas jets produced by such valves is crucial, as the spatial and temporal evolution of the gas density must be thoroughly characterized to ensure optimal performance across different applications. As the gas jet distribution is nontrivial, while simulating HHG, when both the IR and XUV pulse propagates through the medium, it is not possible without characterizing these gas targets.

The increasing availability of intense laser systems operating at repetition rates of 1 kHz and beyond further amplifies the potential of high repetition rate gas jets, enabling the transition of recent innovations—such as the generation of multi-millijoule terahertz (THz) pulses [124] and relativistic single-cycle mid-infrared (MIR) pulses—into regimes of high average power [125]. This transition is not merely a technical milestone, but a gateway to a broad spectrum of novel applications in ultrafast science and strong-field physics.

The use of commercially available solenoid-type valves, such as Even-Lavie [126, 127] or Parker valves [128], albeit limited to repetition rates usually not higher then 1 kHz, has already demonstrated considerable utility in applications like high harmonic spectroscopy of molecules and transient absorption spectroscopy, underscoring the broader relevance of gas jet technologies across multiple experimental platforms.

For high repetition rate applications, where high gas density is not necessary, piezo-cantilever-based gas sources provide a viable alternative to the solenoid-type valves. Current technology enables these pulsed valves to reach operational frequencies of up to 5 kHz, representing a significant step forward for applications requiring both high pressure and high repetition. This study aims to optimize the conditions for efficient HHG, providing essential insights, that can drive further progress in ultrafast and high-field research domains.

Validation of the gas jet system is achieved through interferometric gas density measurements and HHG experiments at ELI ALPS facility [107–109]. Our findings indicate that for optimal HHG, the high-intensity laser interaction must be precisely timed to occur shortly after the valve opens. The evolution of gas density we measured aligns well with both the total flux of generated harmonics and with advanced three-dimensional simulation results, underscoring the critical role of precise gas metrology in these experiments.

3.1 Mach-Zehnder Interferometric Measurement of Gas Density

The Mach-Zehnder interferometer (MZI) is a powerful tool used in various fields of optics, including the precise measurement of gas density [129]. The principle of the interferometer is to split a coherent light beam into two paths, pass one or both paths through a region with varying gas density, and then recombine the beams to produce an interference pattern. The phase shift introduced by the gas in one arm of the interferometer can be used to determine the gas density.

3.1.1 Principle of the MZI

The MZI consists of two beam splitters and two mirrors arranged in such a way that a single light beam is split into two paths, which are then recombined to produce interference. The setup is shown schematically in Figure 3.6 (a)). When a coherent light source with an electric field E_0 is input into the MZI, it is split into two beams at the first beam splitter. The electric fields in the two arms can be described as E_1 and E_2:

$$E_1 = \frac{E_0}{\sqrt{2}} e^{i(\omega t + \varphi_1)}, \tag{3.1}$$

$$E_2 = \frac{E_0}{\sqrt{2}} e^{i(\omega t + \varphi_2)}, \tag{3.2}$$

where φ_1 and φ_2 are the phase shifts accumulated in each arm. When one of the beams passes through a gas cell, it acquires an additional phase shift $\Delta\varphi$ due to the presence of the gas. The electric field in the arm passing through the gas cell becomes:

$$E_2 = \frac{E_0}{\sqrt{2}} e^{i(\omega t + \varphi_2 + \Delta\varphi)}. \tag{3.3}$$

When the beams are recombined at the second beam splitter, they interfere, and the resulting electric field E_D at the detector can be expressed as:

$$E_D = \frac{1}{\sqrt{2}}(E_1 + E_2) = \frac{E_0}{2}\left(e^{i(\omega t + \varphi_1)} + e^{i(\omega t + \varphi_2 + \Delta\varphi)}\right). \tag{3.4}$$

3.1.2 Interference Pattern and Phase Measurement

The intensity I_D at the detector is given by the square of the magnitude of the electric field E_D:

$$I_D = |E_D|^2 = \frac{E_0^2}{4}\left|e^{i(\omega t + \varphi_1)} + e^{i(\omega t + \varphi_2 + \Delta\varphi)}\right|^2. \tag{3.5}$$

Using Euler's formula, the intensity can be further simplified:

$$I_D = \frac{E_0^2}{4}\left(2 + 2\cos(\varphi_1 - \varphi_2 - \Delta\varphi)\right). \tag{3.6}$$

Thus, the interference intensity at the detector is:

$$I_D = \frac{E_0^2}{2}\left(1 + \cos(\Delta\varphi)\right), \tag{3.7}$$

where $\Delta\varphi = \varphi_2 - \varphi_1 + \Delta\varphi$ is the total phase difference between the two arms of the interferometer. The cosine term in the intensity equation leads to an interference pattern, where the maximum and minimum intensities correspond to constructive and destructive interference, respectively.

3.1.3 Inverse Abel transform

The Abel transform is an integral transform, that arises in the analysis of radially symmetric functions, especially in problems involving cylindrical or spherical symmetry. It is particularly useful in areas such as plasma diagnostics, spectroscopy, and tomography, where it helps reconstruct three-dimensional data from line-of-sight projections.

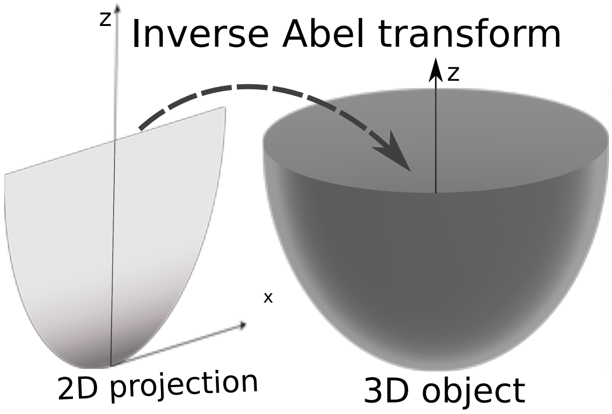

FIGURE 3.1: Illustration of the inverse Abel transform. In this case, the 3D object is a gas distribution, measured through its 2D projection onto a CMOS sensor.

Given a function $f(r)$ that is radially symmetric, the Abel transform $A(y)$ is defined as [130]

$$A(y) = 2\int_y^\infty \frac{f(r)r}{\sqrt{r^2 - y^2}}\,dr, \quad \text{for } y \geq 0. \tag{3.8}$$

This integral expresses the projection of a cylindrically symmetric function along a line of sight, such as the optical line in a physical experiment. The function $A(y)$ corresponds to the observed projection data, and the goal is to recover the original function $f(r)$ from this data (figure 3.1). To perform this recovery, one uses the inverse Abel transform. The inverse transform allows the reconstruction of $f(r)$ from the projected data $A(y)$ and is given by the formula

$$f(r) = -\frac{1}{\pi}\int_r^\infty \frac{dA}{dy}(y) \cdot \frac{dy}{\sqrt{y^2 - r^2}}. \tag{3.9}$$

This equation assumes that the derivative $\frac{dA}{dy}$ exists and is well-defined. In practice, numerical methods are often employed to approximate this derivative and compute the integral, especially when dealing with experimental data that may be noisy or discretely sampled. An alternative formulation, assuming $A(y)$ is sufficiently smooth, involves integrating by parts, yielding

$$f(r) = -\frac{1}{\pi}\frac{d}{dy}\int_r^\infty \frac{A(y)}{\sqrt{y^2 - r^2}}\,dy. \tag{3.10}$$

In this formulation, the inverse transform is written as the derivative of an integral, which can in some cases improve numerical stability. However, the inverse Abel transform is a well-known example of an ill-posed problem [131, 132] in the sense of Hadamard [133, 134]: even small amounts of noise or perturbations in the measured data $A(y)$ can produce large errors in the reconstructed function $f(r)$ [135]. For this reason, practical applications require special care, and stabilization methods such as regularization are commonly employed to obtain reliable results.

3.1.4 The Lorenz-Lorenz Expression

The phase shift $\Delta\varphi$ introduced by the gas is related to the refractive index n of the gas and the length L of the gas cell. The refractive index n depends on the gas density ρ, and the phase shift can be expressed as [136]:

$$\Delta\varphi = \frac{2\pi L}{\lambda}(n-1), \tag{3.11}$$

where λ is the wavelength of the light. From this expression, n can be calculated as:

$$n = \frac{\lambda}{2\pi}\frac{\Delta\varphi}{L} + 1 \tag{3.12}$$

In our case inverse Abel transform takes place, the result of it gives $\Delta\varphi/L$ directly, the rest is a constant value during the experiments.

The Lorenz-Lorenz expression [137] relates the refractive index n of a dielectric medium to its molecular polarizability α and number density $N = \rho/m$, where m is the mass. It provides a bridge between the macroscopic optical property of refractive index and the microscopic property of polarizability. The starting point is the Clausius-Mossotti relation [138, 139], which connects the dielectric constant ε_r of a material to the molecular polarizability:

$$\frac{\varepsilon_r - 1}{\varepsilon_r + 2} = \frac{N\alpha}{3\varepsilon_0} \tag{3.13}$$

where ε_0 is the vacuum permittivity. For non-magnetic materials at optical frequencies, the dielectric constant is approximately related to the refractive index by $\varepsilon_r \approx n^2$. Substituting this into the Clausius-Mossotti relation gives:

$$\frac{n^2 - 1}{n^2 + 2} = \frac{N\alpha}{3\varepsilon_0} \tag{3.14}$$

This is the Lorenz-Lorenz expression. It shows that the quantity $(n^2-1)/(n^2+2)$, often called the Lorenz-Lorenz function, is proportional to the molecular polarizability per unit volume. The derivation assumes that the local electric field acting on a molecule can be approximated by the Lorentz local field, which includes the effect of nearby dipoles and the macroscopic field. The inverse form of the expression is also useful, allowing one to calculate the refractive index from the polarizability:

$$n^2 = \frac{1+2R}{1-R}, \quad \text{where} \quad R = \frac{N\alpha}{3\varepsilon_0} \tag{3.15}$$

This formulation is widely used in physical chemistry [140] and materials science [141] for estimating molecular polarizability from refractive index data or vice versa, particularly in gases and dilute liquids where the assumptions underlying the derivation are most valid.

3.2 Simulation of Interferometric Phase Retrieval for Low Refractive Index Media

The refractive index of the noble gases commonly used in high-order harmonic generation is close to unity, resulting in very small optical path differences even at elevated backing pressures. Consequently, extracting meaningful phase information from such low-index media requires highly sensitive diagnostic techniques. Two general approaches exist for optical phase measurement: wavefront sensing [142] and interferometry [143]. While wavefront-based techniques, such as those using Shack-Hartmann sensors, offer the advantage of simpler experimental implementation, their phase reconstruction algorithms are often proprietary and tailored to specific hardware, limiting their applicability in universal and automated systems, such as beamline diagnostics.

In contrast, interferometric methods offer greater flexibility and transparency in analysis. A classical implementation involves a Mach-Zehnder interferometer, in which two coherent replicas of a laser beam are generated. One of these beams is directed through the target medium, thereby accumulating a phase shift due to the refractive index variation [144], while the other serves as a reference. When the two beams are recombined, the resulting interference pattern encodes the relative phase difference induced by the medium. Since experimental data consist of two-dimensional interferograms recorded under non-ideal conditions, a robust and quantitative retrieval of the phase requires proper validation. For this purpose, a numerical simulation was conducted to investigate the sensitivity and accuracy of the Fourier filtering method under varying experimental parameters. The simulation accounts for realistic fringe distortions, noise sources, and the specific characteristics of the gas jet geometry. The gas jet is formed by a conical nozzle operating in the subsonic regime, as described in [145], which leads to a transverse gas density profile that can be approximated by a two-dimensional Gaussian function. In the simulation, the fringe pattern is modeled by superimposing a Gaussian-shaped phase distribution onto a sinusoidal carrier wave. The resulting intensity pattern $I(x, y)$ is given by the following expression:

$$I(y,z) = A\cos\left(2\pi\nu(y,z) + B\exp\left(-\frac{(y-y_0)^2+(z-z_0)^2}{2\sigma^2}\right) + n_\phi(y,z)\right) + n_a(y,z), \tag{3.16}$$

where A is the amplitude of the carrier wave, $\nu(y, z)$ represents its spatial frequency (typically constant across the field), and B and σ characterize the amplitude and width of the Gaussian phase modulation, respectively.

This can be written simpler in a form:

$$I(y,z) = a(y,z) + b(y,z)\cos\left[2\pi f_0 x + \phi(y,z)\right], \tag{3.17}$$

where f_0 is the spatial-carrier frequency, a(y,z) and b(y,z) are amplitudes, which we are not interested.

The terms $n_\phi(x, y)$ and $n_a(x, y)$ denote additive phase and amplitude noise, both modeled as normally distributed random variables to mimic experimental uncertainties.

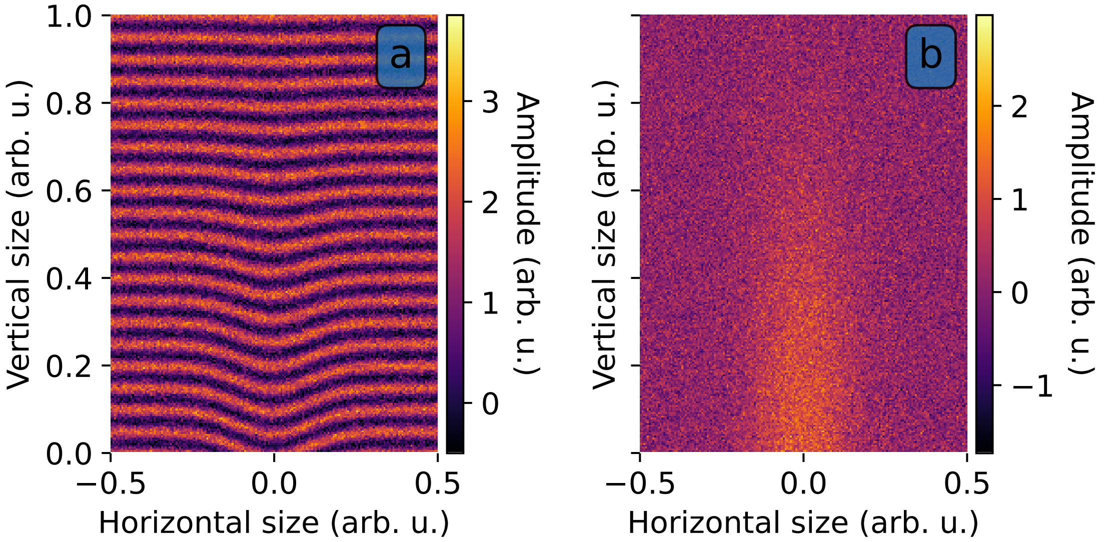

FIGURE 3.2: Simulated interference pattern. Panel (a) shows the generated fringes, bent by the applied phase profile, while panel (b) presents the corresponding phase introduced by the gas jet. Gaussian noise in both amplitude and frequency was added to test the retrieval algorithm.

Figure 3.2 (a)) displays a simulated fringe pattern based on this formulation, where the Gaussian-shaped phase profile, representing the refractive index variation induced by the gas jet, is shown in Figure 3.2 (b)).

Because the refractive index of noble gases is very close to one, the actual phase shifts encountered experimentally are quite small; for visualization purposes, the values used in the simulation are scaled up to enhance contrast. The primary goal of this simulation is to develop a robust and automated algorithm for retrieving the phase distribution from raw interferometric data. The algorithm must function without manual intervention and be computationally efficient enough to support real-time data processing. This capability is essential for integration into beamline control software, allowing users to dynamically adjust experimental parameters such as backing pressure, timing synchronization, and exposure duration based on live feedback.

To retrieve the embedded phase information, Fourier filtering is employed. For fringe patterns with nearly horizontal orientation, as illustrated in Fig. 3.2 (a), the two-dimensional Fourier transform yields two prominent vertical peaks corresponding to the carrier frequency, as expressed in Eq. (3.17).

Using Euler's formula, $\cos(x) = \frac{1}{2}\big(e^{ix} + e^{-ix}\big)$, the fringe intensity can be written as [146]:

$$I(y,z) = a(y,z) + c(y,z)\, e^{2\pi i f_0 y} + c^*(y,z)\, e^{-2\pi i f_0 y}, \tag{3.18}$$

where

$$c(y,z) = \tfrac{1}{2}\, b(y,z)\, e^{i\phi(y,z)}. \tag{3.19}$$

After applying the Fourier transform with respect to y, we obtain

$$\tilde{I}(f_y,z) = \tilde{a}(f_y,z) + \tilde{c}(f_y - f_0, z) + \tilde{c}(f_y + f_0, z), \tag{3.20}$$

where f_y denotes the spatial frequency along the y-direction. As a(y,z), b(y,z) and ϕ(y,z) vary much slower than f_0, they can be separated in Fourier space. By isolating one of the sidebands $\tilde{c}$ in Fourier space and transforming back, the phase information can be retrieved as the argument of $c(y,z)$ defined in Eq. (3.19).

Finally, this formulation can be directly applied to the measured data, where the Fourier-transformed intensity can be expressed as:

$$\widetilde{I}(k_y,k_z) \;=\; \mathcal{F}\{I\}(k_y,k_z) \;=\; \iint_{\mathbb{R}^2} I(y,z)\, e^{-i(k_y y + k_z z)}\, \mathrm{d}y\, \mathrm{d}z. \tag{3.21}$$

This filtering process involves selecting one of the carrier peaks—along with a small surrounding region of spatial frequencies—and shifting it to the origin of a new frequency array. This effectively removes the carrier modulation, enabling the extraction of the underlying phase. However, the finite size of the selection window imposes a constraint on the accuracy of the inverse transform. For instance, a Gaussian profile in the spatial domain transforms into another Gaussian in the frequency domain. Approximating such profiles using a limited set of discrete frequencies introduces distortions. To reduce these artifacts, smooth window functions such as the Blackman or Hamming windows

$(H(k_y, k_z))$ are applied to the selected region. This can be written in a form of:

$$H(k_y, k_z) \;=\; h(k_y)\, h'(k_z), \tag{3.22}$$

where

$$h(k_y) = 0.54 - 0.46 \cos\left(\pi \frac{k_y - k_{y,\mathrm{min}}}{k_{y,\mathrm{max}} - k_{y,\mathrm{min}}}\right), \tag{3.23}$$

and similarly:

$$h'(k_z) = 0.54 - 0.46 \cos\left(\pi \frac{k_z - k_{z,\mathrm{min}}}{k_{z,\mathrm{max}} - k_{z,\mathrm{min}}}\right), \tag{3.24}$$

These functions minimize spectral leakage and edge effects, thereby improving the accuracy of the phase reconstruction. The concept of the selection process is illustrated in Figure 3.3, which displays the Fourier transform of the simulated interferogram (Figure 3.2). To select part of the array, one can define a rectangle function with Δ interval as

$$\mathrm{rect}\left(\frac{u}{\Delta}\right) = \begin{cases} 1, & |u| \leq \frac{\Delta}{2}, \\ 0, & \text{otherwise.} \end{cases} \tag{3.25}$$

The white box overlaid on the image indicates a typical region of interest chosen for filtering. This sort of rectangular selection with Δk_y and Δk_z size edges, which centered around (k_{y0}, k_{z0}) from the center and can be defined as

$$S^{\mathrm{rect}}_{\mathbf{k}_0}(k_y, k_z) = \mathrm{rect}\left(\frac{k_y - k_{y0}}{\Delta k_y}\right)\, \mathrm{rect}\left(\frac{k_z - k_{z0}}{\Delta k_z}\right). \tag{3.26}$$

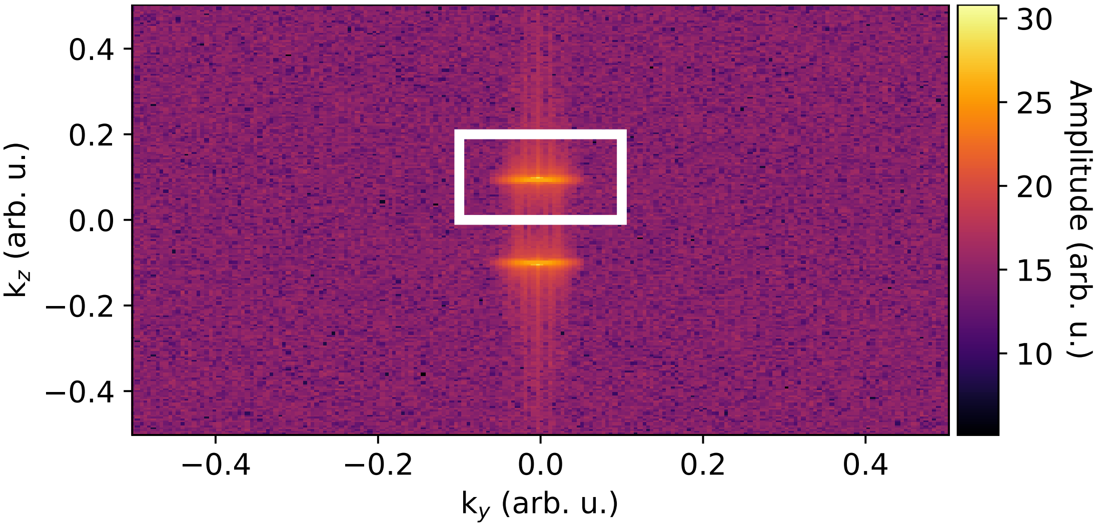

FIGURE 3.3: Fourier transform of the interferogram. The white box represents the selection area with edge length of Δk_x and Δk_y.

The Hamming window and the selection mask applied to the original array as:

$$\widetilde{I}_{\text{sel}}(k_y, k_z) \;=\; \widetilde{I}(k_y, k_z)\; S^{\text{rect}}_{\mathbf{k}_0}(k_y, k_z)\; H(k_y, k_z). \tag{3.27}$$

Once the desired frequency component has been isolated in the Fourier domain, it is shifted to the original center.

$$\widetilde{I}_{\text{shift}}(k_y, k_z) = \widetilde{I}_{\text{sel}}(k_y - k_{y0}, k_z - k_{z0}) \tag{3.28}$$

To retrieve the signal one needs to perform an inverse Fourier transform on the array as:

$$I_{\text{f}}(y, z) \;=\; \mathcal{F}^{-1}\{\widetilde{I}_{\text{shift}}\}(y, z) \;=\; \frac{1}{(2\pi)^2} \iint_{\mathbb{R}^2} \widetilde{I}_{\text{shift}}(k_y, k_z)\, e^{\,i(k_y y + k_z z)}\, \mathrm{d}k_y\, \mathrm{d}k_z. \tag{3.29}$$

After performing the inverse transform, the complex-valued result contains both amplitude and phase information as $I_{\text{f}}(y, z) = A(y, z)\, e^{\,i\phi(y,z)}$, where $A(y, z)$ is the amplitude and and $\phi(y, z)$ as phase, these can be extracted simply as

$$A(y, z) \;=\; |I_{\text{f}}(y, z)| \;=\; \sqrt{\big(\operatorname{Re}[I_{\text{f}}(y, z)]\big)^2 + \big(\operatorname{Im}[I_{\text{f}}(y, z)]\big)^2}, \tag{3.30}$$

and

$$\phi(y, z) \;=\; \arg\big(I_{\text{f}}(y, z)\big) \;=\; \operatorname{atan2}\big(\operatorname{Im}[I_{\text{f}}(y, z)]\,,\, \operatorname{Re}[I_{\text{f}}(y, z)]\big). \tag{3.31}$$

Figure 3.4 presents a side-by-side comparison between the original Gaussian phase distribution used in the simulation and the phase retrieved through the Fourier filtering method. In this case, no additional noise was introduced in Equation (3.16) to isolate the effect of the filtering process itself. As Fourier filtering inherently acts as a low-pass filter, high-frequency components—such as those introduced by noise—are suppressed. This explains the smoothness observed in the retrieved phase.

The right-hand panel of Figure 3.4 demonstrates that the algorithm successfully reconstructs the spatial shape and amplitude of the original phase profile, validating the accuracy of the method under ideal conditions. This provides a strong foundation for its application to experimental data, where additional noise-reduction techniques may be necessary to maintain similar fidelity.

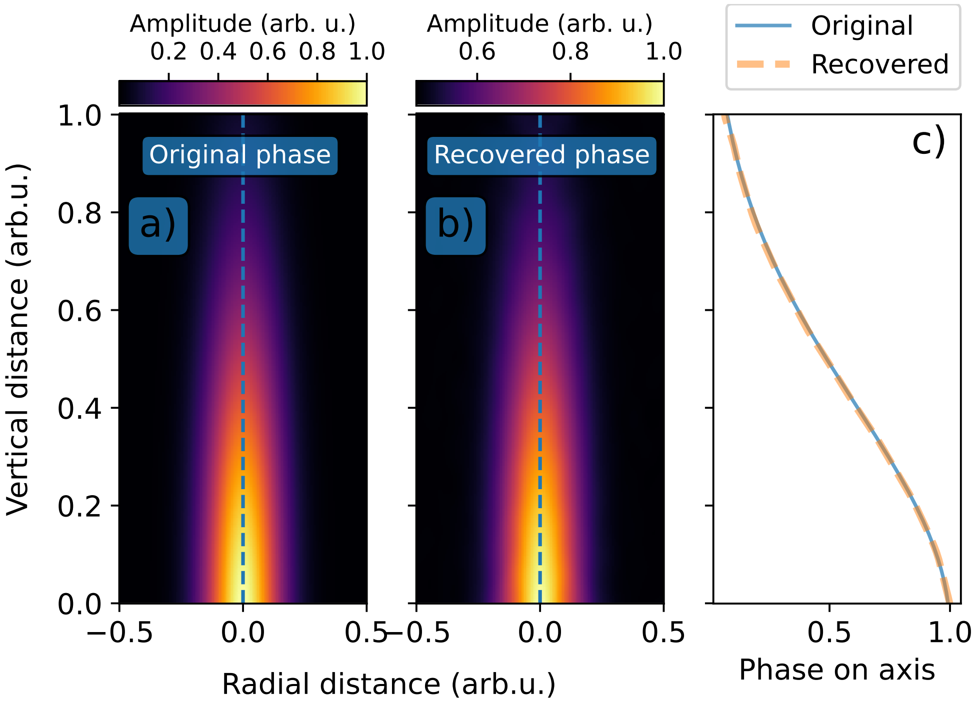

FIGURE 3.4: Comparison of the original Gaussian phase distribution (a) and the recovered phase using Fourier filtering (b). Panel (c) depicts the phase evolution along the central axis of the jet, represented by a dashed line in (a) and (b).

3.3 Experimental Apparatus for the interferometric measurement

For the experimental tests, seen in figure 3.5 (a)., an Amsterdam Piezo Valve (ACPV3 model) was employed (figure 3.5 (b)). This valve utilizes a cantilever-type piezoelectric actuator in conjunction with a nozzle of 500 µm diameter. Cantilever piezo actuators are particularly advantageous in high-speed gas delivery applications due to their capability to produce relatively large mechanical displacements—ranging from several hundred micrometers up to nearly 1 mm—while operating reliably at repetition rates of up to 5 kHz. A distinguishing feature of cantilever-based piezo actuators, as compared to traditional disk-shaped piezos, is the ability to tune the mechanical response by adjusting the free length of the cantilever beam. This tuning enables direct control over the actuator's displacement characteristics: reducing the free length leads to a sharp decrease in displacement, while simultaneously increasing the resonant frequency of the system [147].

A schematic representation of the experimental setup is provided in Figure 3.6, which outlines the optical layout and key components used in the interferometric measurements. As a coherent light source, a stabilized Helium-Neon (HeNe) laser was employed. These

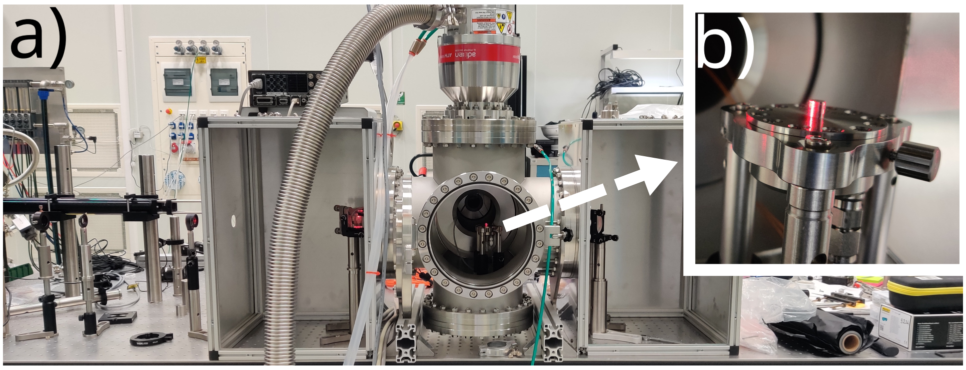

Figure 3.5: Experimental setup for gas-jet characterization. Panel (a) shows an overview of the vacuum chamber and optical components, while panel (b) provides a close-up view of the target piezo-driven gas valve. A schematic drawing of the setup is presented in Fig. 3.6.

lasers are well known for their excellent temporal coherence, long-term wavelength stability, and low amplitude noise, making them ideal for high-precision interferometry and long-duration measurements where phase stability is critical.

To expand the laser beam and ensure uniform illumination over the region of interest, a Keplerian telescope configuration was implemented. The telescope was designed to enlarge the beam sufficiently to cover the full extent of the gas jet as projected in the object plane. Additionally, a spatial filter consisting of a pinhole placed at the focal point of the first lens was included to suppress spatial noise and improve beam uniformity. Although the input beam quality was already reasonably good, the spatial filter proved beneficial in reducing high-frequency noise components, particularly those introduced by residual diffraction effects or imperfections in the laser output.

The core of the interferometric measurement system is a Mach-Zehnder interferometer, constructed using two non-polarizing beam splitter cubes. This design allows for the splitting and later recombination of the laser beam into two coherent arms. Ideally, the optical path segment between the beam splitters—where the gas interaction occurs—should be maintained under vacuum to minimize disturbances from air fluctuations. However, due to spatial constraints within the available vacuum chamber, full vacuum isolation was not feasible. To mitigate the influence of environmental air movement, the exposed beam path was enclosed in a protective box. Although this reduced the impact of air currents, it could not entirely eliminate phase noise introduced by refractive index variations in the ambient air.

Both interferometric arms propagate through a vacuum chamber that houses the gas target, with the two beam splitters positioned as close as possible to the entrance and exit windows. This arrangement minimizes the optical path in air and helps maintain precise alignment. Furthermore, since the two arms of the interferometer remain in close proximity throughout the system, it is possible to record reference images with the gas

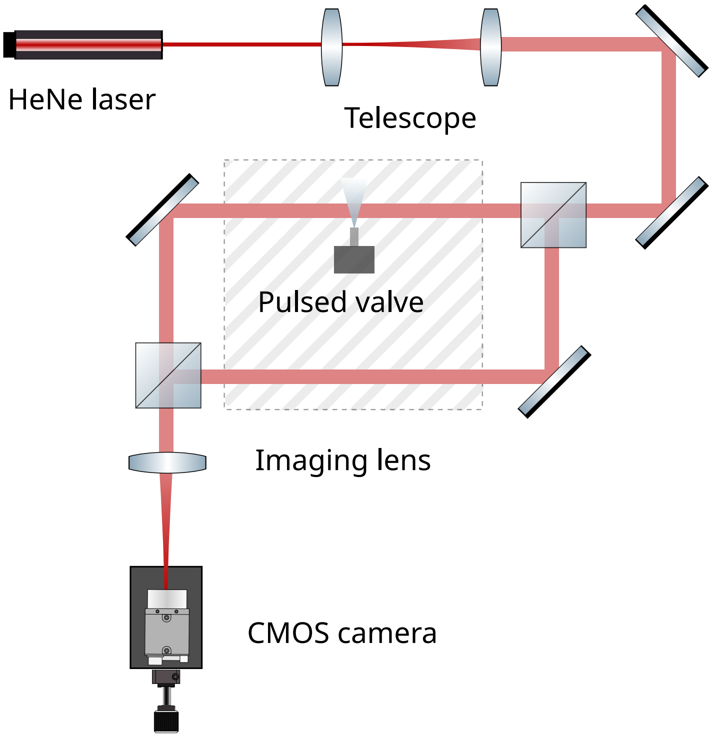

FIGURE 3.6: Experimental setup corresponding to that shown in Figure 3.5. The HeNe laser beam is expanded with a Kepler telescope and then split into two paths by a beam splitter cube. Both arms enter the vacuum chamber, but only one interacts with the gas jet. After recombination at a beam splitter cube, the jet is imaged onto a CMOS camera chip using a lens.

jet turned off and use them for background subtraction in data processing, significantly improving the signal quality and enabling precise phase retrieval. After recombination of the two beams at the second beam splitter, the central plane of the gas nozzle was imaged onto the camera sensor using a high-quality lens. To achieve a shallow depth of field and ensure spatial selectivity in the imaging plane, a lens with a short focal length was chosen. The imaging optics were optimized to capture the entire width of the gas jet while minimizing out-of-focus contributions, which is essential for accurately resolving small-scale phase features. The magnification of the system is 1.61, this allows up to 3.6 µm spatial resolution, as the pixel size of the sensor is 4.4 µm, although the phase retrieval algorithm reducing the resolution significantly, due to the Fourier filtering.

Figure 3.7 illustrates two representative interferometric measurements. The left panel shows the recorded interference pattern in the absence of the gas jet, serving as a reference frame, while the right panel displays the modified interference fringes in the presence of the jet, demonstrating the measurable phase shift induced by the gas.

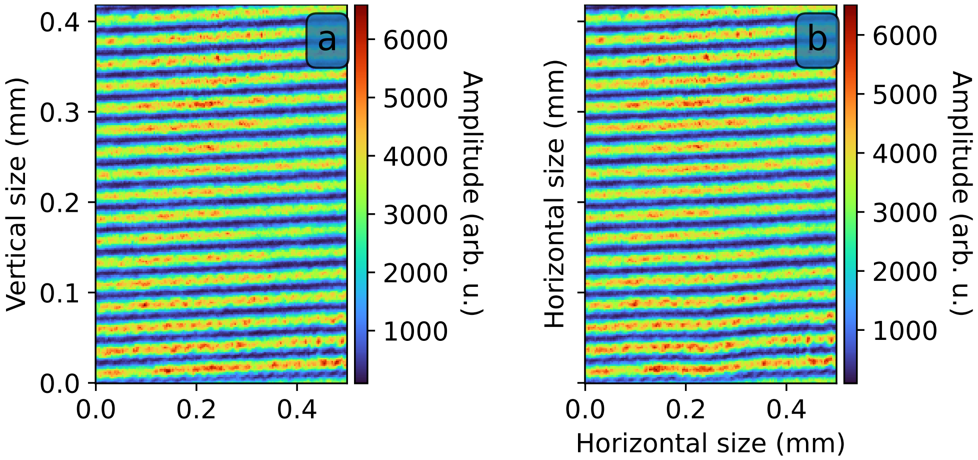

Figure 3.7: Measured interferograms, (a) show the case when the gas valve turned off, while (b) shows the interferogram in the presence of the gas jet.

3.4 Software development for the jet characterization setup

As the gas jet only introduces an optical path difference, much lower than the wavelength of the laser, finding the signal and optimizing it for long scans is not a trivial task. As the vacuum system on the test setup has limited capacity, the repetition rate of the gas jet and the acquisition has to be lowered. As all these changes have an effect on each other, a control graphical user interface (GUI) had been developed with the necessary functionality for these measurements. This GUI was developed under Python using Qt5 wrapper, controlling the camera, the delay generator, the pulsed valve controller and can monitor the pressure in the vacuum chamber. The data analysis are relying on standard Python packages, such as Numpy [148], Scipy [149] and OpenCV [150].

The acquisition device during these experiments is a Basler acA1440-73gm camera, the raw image from the sensor can be seen of figure 3.8 (b). The camera settings must be adjusted in real time. During optimization the signal was often too weak, which required longer exposure times, whereas time-dependent scans demanded much shorter exposures to preserve temporal resolution. This made it necessary to iteratively adjust both the camera parameters and the experimental setup (Fig. 3.8 (a)). It is useful to retrieve the momentary phase online, this is computationally heavy, which can be lowered by reducing the calculational area (figure 3.8 (c)). The phase profile from the selected region can be seen on figure 3.8 (e). The repletion rate of the jet will determine the residential pressure in the chamber, to have a clear transition between the jet and vacuum this should be minimized at each shot. On figure 3.8 (d) a readout from a gas gauge on the chamber can be seen at each event, this pressure changing from $1 \cdot 10^{-6}$ mbar to the peak at $2 \cdot 10^{-5}$

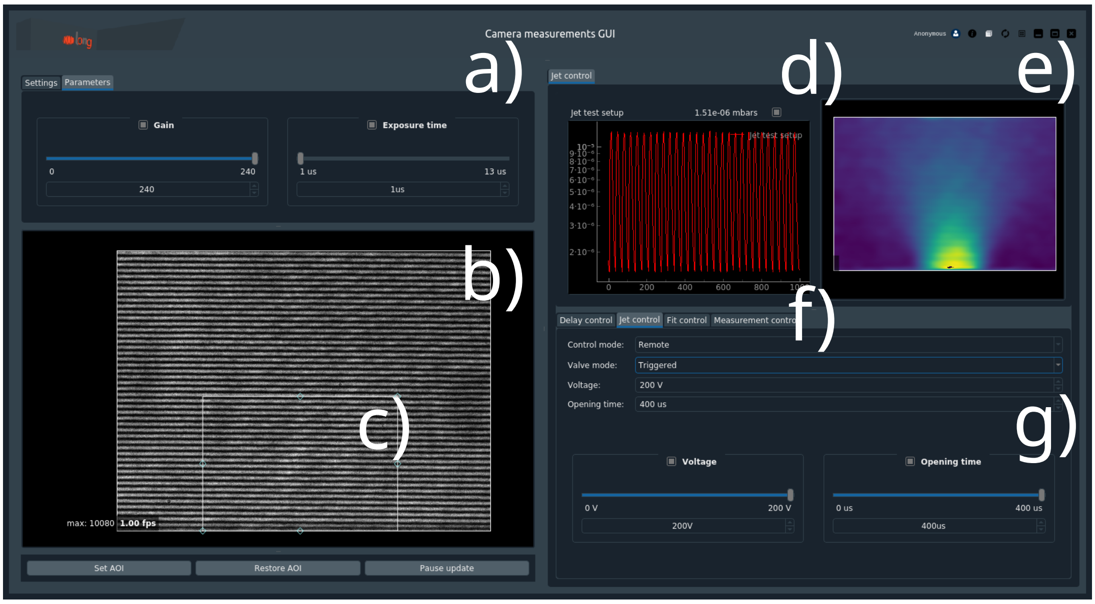

Gain: 240

Exposure time: 1us

Control mode: Remote

Valve mode: Triggered

Voltage: 200 V

Opening time: 400 us

Voltage: 200V

Opening time: 400us

FIGURE 3.8: Current version of the graphical user interface, developed in PyQt, used to control the measurement instruments: camera (a–c), jet controller (g), delay generator (f), and pressure gauge (d). A basic level of data processing is implemented to enable online monitoring of the phase measurement (e).

mbar.

The parameters for the measurements are separated to different panels, this includes the delay generator settings (figure 3.8 (g)), the parameters for the data processing, the parameters for the pulsed jet such as the open time and voltage on the piezo and how long the recording would take place at which delay steps (figure 3.8 (f)).

3.5 Phase Retrieval from Measured Interferograms

The methodology, used to retrieve the phase information from the interferometric data, is based on the numerical procedure outlined in Section 3.2, where the underlying algorithm was initially introduced and tested using simulated data. However, in the case of experimental measurements, additional considerations must be taken into account due to the presence of background phase contributions, originating from optical imperfections, vibrations, or systematic environmental effects that are superimposed on the measured signal.

To isolate the phase shift attributable solely to the gas jet, a background subtraction technique is employed. Unlike the simulated case where a clean reference is assumed, in the experimental setup, the background contains meaningful phase information that needs to be carefully removed to obtain an accurate reconstruction of the gas-induced phase shift. To achieve this, the experimental procedure involves synchronized acquisition using a high-speed camera that records images at twice the operating frequency of the piezoelectric gas valve. This alternating capture strategy ensures that each phase image taken with the gas jet active is immediately followed or preceded by a reference image acquired under identical optical conditions but with the valve in its closed (inactive) state.

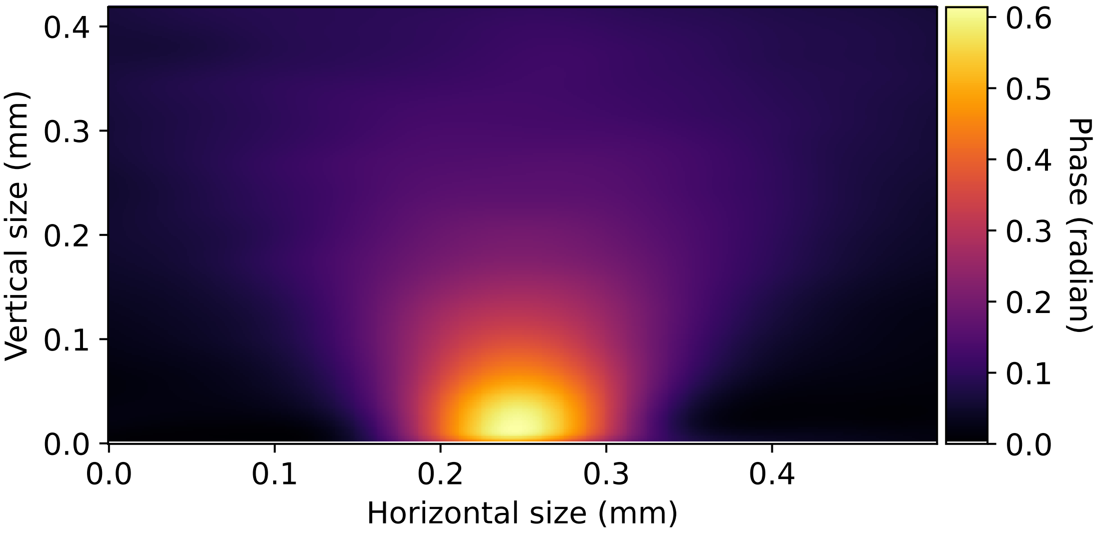

Figure 3.9: 2D map of the recovered phase, shown on the camera chip. The axes correspond to the pixel dimensions.

By pairing each measurement image with a corresponding reference, it becomes possible to subtract the background phase contribution on a frame-by-frame basis, resulting in a differential phase image that reflects only the changes induced by the gas jet. This technique effectively suppresses static and slowly varying background noise, allowing for precise retrieval of the dynamic phase profile associated with the transient gas density distribution. The final processed phase map, obtained after background correction and numerical phase retrieval, is shown in Figure 3.9.

From this phase map, several conclusions can be drawn. First, the interaction point should not be placed more than 200 µm (around 400 µm considering the magnification) above the nozzle exit, as the gas density decreases rapidly with height. Second, a certain distance must be maintained from the nozzle exit due to the laser focus spot size. Even at 100 µm (200 µm with magnification) above the exit, the region of highest density amplitude extends only about 300 µm (600 µm with magnification) in the horizontal direction, which therefore constrains the allowable focal spot size.

The distribution has cylindrical symmetry - this is expected as the nozzle has cylindrical symmetry as well - this simplifies the number density retrieval. The gas expanding from a reservoir through a nozzle into a vacuum initially undergoes a *subsonic free-jet expansion*. In this regime, the pressure ratio across the nozzle is insufficient to accelerate the flow to supersonic speeds, and the gas velocity remains below the local speed of sound.

The resulting jet expands into the vacuum with a smooth density gradient, without the formation of shock structures that characterize supersonic jets. [151]

3.6 Reconstruction of the Gas Density Profile

The phase shift measured through interferometric techniques represents a line-integrated quantity, corresponding to the two-dimensional projection of the gas density distribution along the optical path of the probe beam. This measurement inherently integrates the refractive index variations, caused by the gas medium across the entire thickness of the jet, yielding a projected phase profile over the transverse plane. In the case of gas jets formed

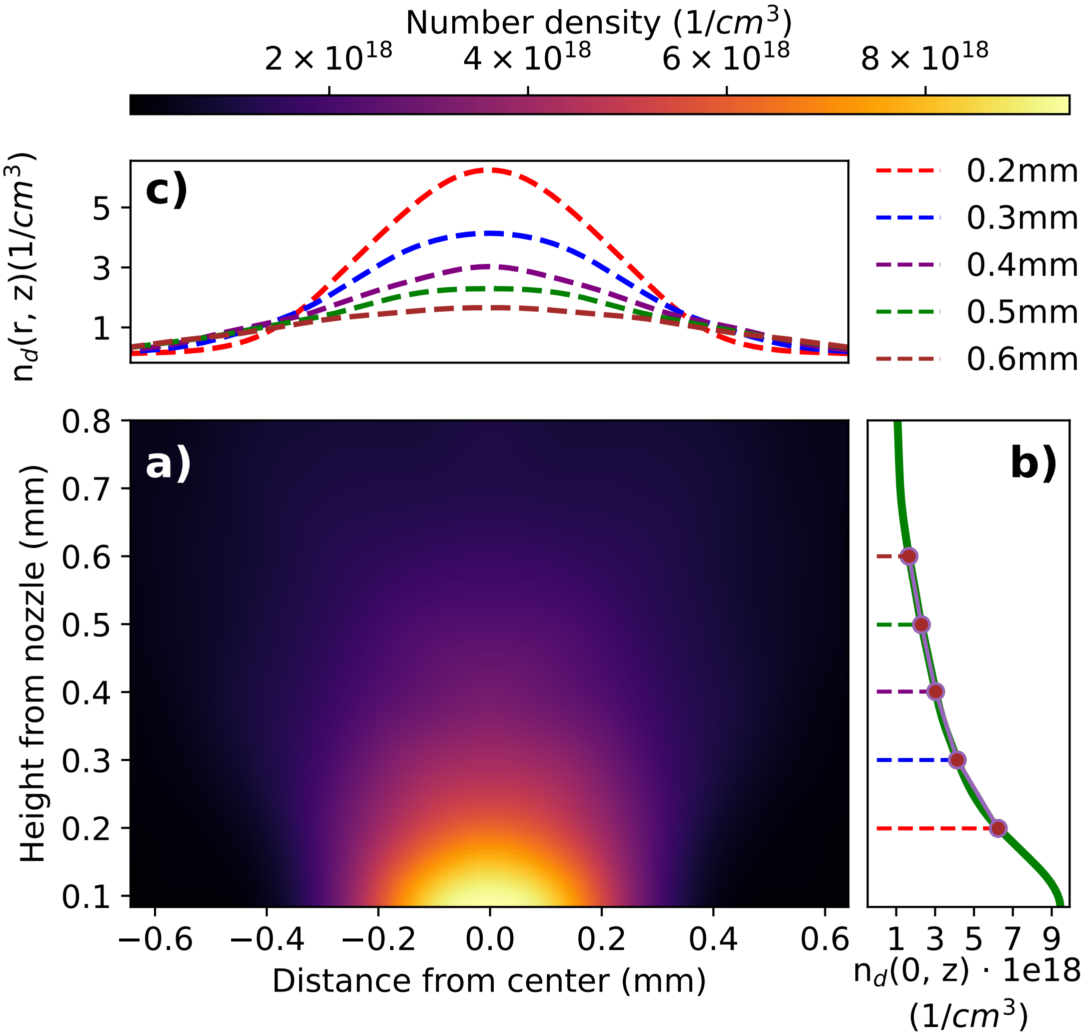

FIGURE 3.10: Retrieved number density of the gas jet at an arbitrary time delay after the cantilever opening. Panel (a) shows the radial dependence of the gas density at different heights above the nozzle. Panel (b) presents the axial dependence, with markers indicating the positions corresponding to the heights in panel (a). Panel (c) displays the vertical profile of the jet at the same selected heights as in panel (b).

by cylindrical nozzles, it is reasonable to assume cylindrical symmetry of the density distribution. This assumption allows for the application of the inverse Abel transform to recover the underlying three-dimensional radial distribution of the refractive index from the two-dimensional projection. The inverse Abel transformation is a mathematical technique that deconvolves the path-integrated data under the assumption of axial symmetry, thus providing access to the local radial values of the phase shift. A more detailed discussion of the implementation and theoretical background of this transform is presented in Section 3.1.3.

Once the radial distribution of the refractive index has been obtained, it becomes possible to convert this optical information into a physical quantity—namely, the number density of the gas (n_d). This conversion is performed using the Lorenz-Lorenz expression, at equation (3.15), which relates the refractive index of a medium to its molecular polarizability and number density under the assumptions of linear optics and dilute gases. The theoretical foundation and derivation of the Lorenz-Lorenz relation are provided in Section 3.1.4. By applying this procedure to the experimental data, a full spatial map of the gas number density can be reconstructed from the original phase measurements. The final result of this analysis, showing the numerically reconstructed number density profile, is presented in Figure 3.10. This result is critical for accurate modeling of gas-target interactions in high-intensity laser experiments, as well as for validating numerical simulations of jet dynamics.

3.7 Temporal evolution of the gas density

The temporal dynamics directly influence the effective number density of the gas during the laser-gas interaction, which in turn affects both the phase matching and the overall efficiency of the HHG process.

Time dependence had been measured by delaying the acquisition of the camera compared to the opening of the jet using a delay generator. A few selected number density arrays from the measurement is shown on figure 3.11.

Figure 3.12 illustrates the temporal evolution of the gas number density during the opening period of the piezo-driven gas valve, which can extend up to 600 µs. The measurement reveals considerable fluctuations in the density, with variations reaching as much as 40% between the peak and valley values. Such deviations are particularly important when the exposure time of the imaging system is not sufficiently short or if it is not synchronized with the temporal peak of the gas pulse—the moment when the laser interaction is most effective. Failure to account for this synchronization can lead to substantial errors in the inferred number density, ultimately compromising the accuracy of the experimental results and any associated simulations or diagnostics. Therefore, precise timing and

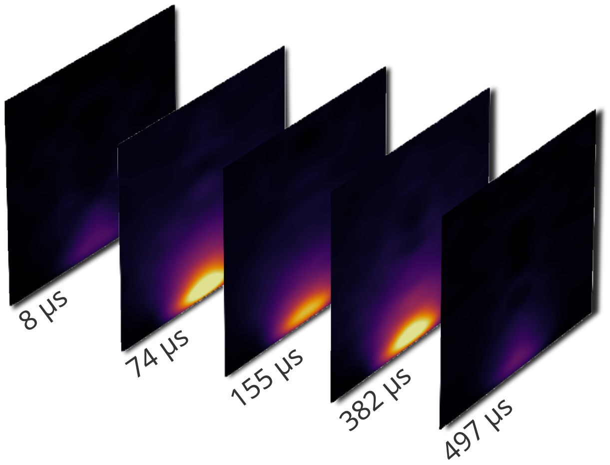

Figure 3.11: Measured number density profiles at different time delays. It is visible, that the gas density is reaching the maximal value at two different time, while decreasing in-between these maxima.

control of the exposure window are essential to ensure that the measurements faithfully represent the gas conditions during high-intensity laser interaction.

These fast fluctuations, which were surprising originally, are present only with cantilever type pulse valves. The valve consists of a thin piezoelectric sheet mounted as a cantilever that seals a small orifice. When a voltage is applied, the piezoelectric element bends due to the inverse piezoelectric effect. The applied electric field induces strain in the crystal lattice, causing the sheet to deflect. This bending lifts the cantilever from its seat, opening the orifice and allowing a burst of gas to expand into vacuum.

The piezo element behaves mechanically like a cantilever beam with well-defined eigenfrequencies (typically in the range of a few kHz to several tens of kHz, depending on dimensions, stiffness, and mounting). When driven near resonance, the cantilever exhibits oscillatory motion; however, in valve operation it is usually driven by short voltage pulses, so that the deflection corresponds to a rapid opening and closing rather than sustained oscillation. The transient response is thus determined by the eigenfrequency and damping of the cantilever, which govern the achievable pulse duration and reproducibility. This eigenfreqency can be determined from the measurement with Fourier transform, yielding 5.7 kHz.

3.8 Backing pressure dependence of the gas density

The pressure in the gas valve support tube is a key parameter, as experimentally it provides the simplest way to control the gas output. The gas cylinders are equipped with pressure regulators, and in the following results only the regulator setting was varied. The results of the measurements are presented in Figure 3.13. Under normal operating

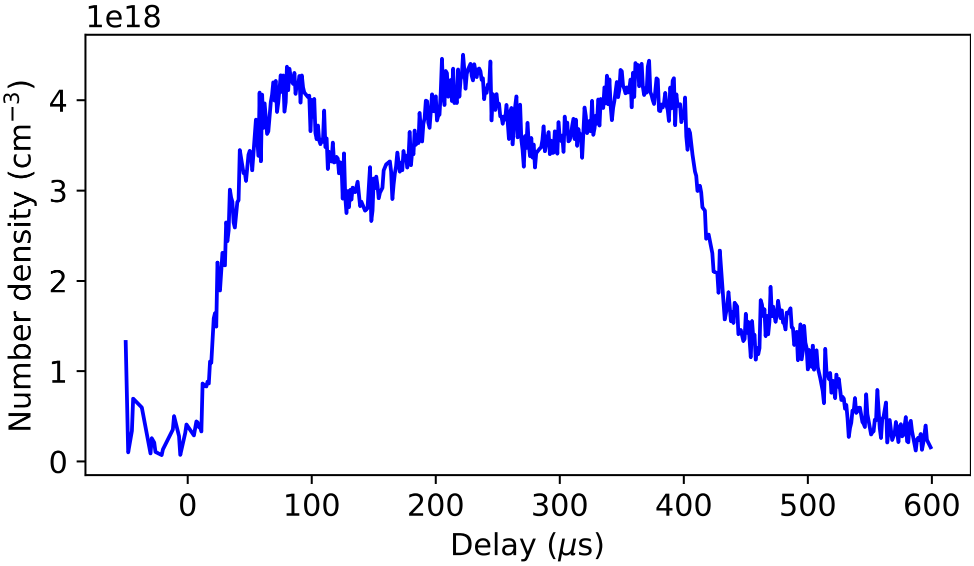

FIGURE 3.12: Temporal evolution of the number density measured with the interferometric technique. The nozzle opens at time zero and remains open for 600 µs. The curve shows that the maximum number density is reached after approximately 80 µs, followed by pronounced oscillations.

conditions, the valve functions at a pressure of 3–5 bar (i.e., 2–4 bar above atmospheric pressure). For this study, the measurements were conducted at 3.5 bar, alongside the HHG experiment, corresponding simulations, and interferometric measurements. As shown in the figure, the number density increases exponentially with the backing pressure. This exponential trend is represented by the dashed line in the graph.

To investigate the temporal behavior of the gas jet, time-resolved measurements were conducted by introducing a controlled delay between the activation of the gas valve and the acquisition window of the detection system. This delay was implemented using a precision delay generator, which allowed the synchronization of the camera shutter with respect to the opening of the pulsed gas jet valve. By systematically varying the delay, the temporal evolution of the gas flow dynamics could be captured and analyzed with high temporal resolution.

Typically, the valve operates within a backing pressure range of 3 to 5 bar. For consistency and reproducibility in subsequent experiments, a nominal backing pressure of 3.5 bar was selected as the standard operating condition. All high-harmonic generation measurements, numerical simulations, and interferometric diagnostics were performed under this fixed pressure condition to ensure comparability and to minimize experimental variability.

The choice of 3.5 bar represents a balance between achieving sufficient gas density for efficient nonlinear optical interaction and maintaining operational stability of the pulsed valve system. This controlled approach to timing and pressure regulation is essential for precise characterization of the jet parameters and their impact on the high-harmonic

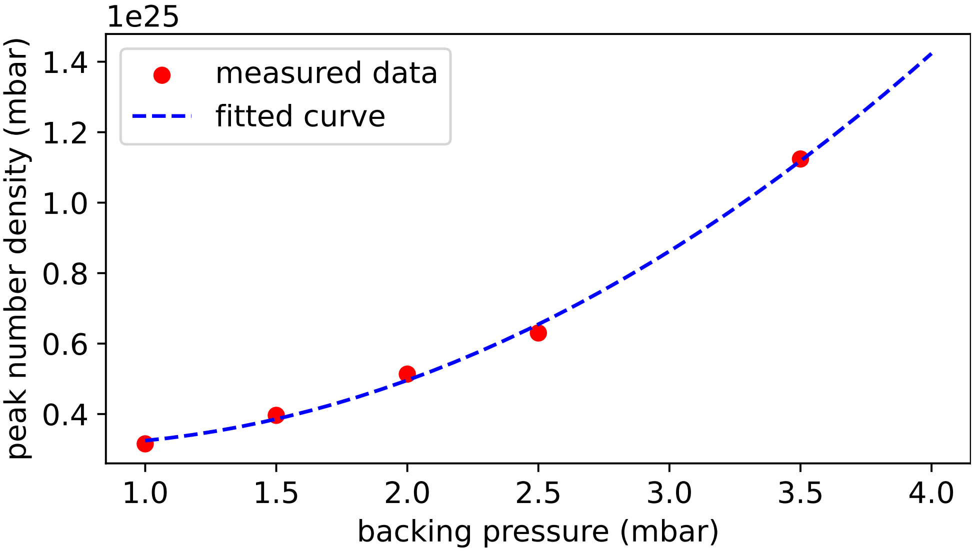

FIGURE 3.13: Backing pressure dependence of peak number density. The measured data (red dots) show exponential growth, with the fitted exponential trend represented by the blue dashed line.

generation process.

For these backing pressures, time-dependent measurements were carried out, and the results are shown in Fig. 3.14. In this case, the valve opening time was only 300 µs, compared to 600 µs in Fig. 3.12, yet two density oscillations are still visible. Small differences can be observed in the timing of the maximum number density and in the overall distribution. The main conclusion is that varying the backing pressure primarily affects the peak number density, while leaving the other parameters largely unchanged."

3.9 Experiment with SYLOS GHHG Compact

The SYLOS GHHG Compact beamline [152–154] is designed to deliver high-flux radiation in the vacuum ultraviolet (VUV) and extreme ultraviolet spectral regions through high-order harmonic generation in a loosely focused geometry. Utilizing either a gas jet or a gas cell as the nonlinear medium, the system supports efficient upconversion of intense infrared pulses into coherent short-wavelength radiation. The beamline is optimized to produce attosecond or few-femtosecond pulse durations, covering a broad range of photon energies that span from the VUV to the XUV domain, while ensuring high spectral brightness and reliable long-term operation.

A comprehensive schematic of the SYLOS GHHG Compact beamline, illustrating its modular layout and key functional units, is shown in Figure 3.15.

The beamline architecture is organized into several distinct but seamlessly integrated sections. It begins with the laser beam alignment stage, which ensures the precise delivery of the driving IR pulse into the interaction region. This is followed by the infrared focusing

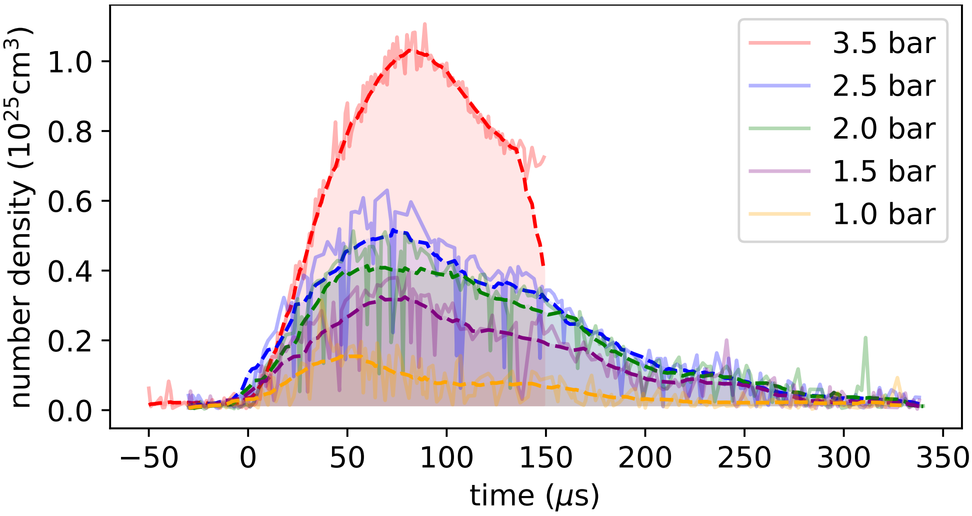

FIGURE 3.14: Effect of backing pressure on the temporal dynamics of the jet number density. In this case, the jet was opened for 200 µs. At a backing pressure of 1 bar (equal to the ambient pressure), the number density reaches its maximum approximately 50 µs after opening. At higher pressures, the temporal profile remains similar across all cases.

section, which compresses and concentrates the beam to the intensity regime required for efficient HHG. The harmonic generation process itself occurs within the HHG source region 3.15 (d)), after which the generated XUV radiation is directed into a diagnostics section. Here, spectral, spatial, and temporal characterization of the harmonics can be performed.

The beamline architecture supports the use of multiple gas jets in combination as the generation medium for HHG. This flexibility enables optimization of the output by tuning parameters such as gas pressure, which directly affects the phase matching conditions within the interaction region. As detailed in Section 1.2.6, phase matching is a key factor in determining both the efficiency and the spectral characteristics of HHG. By selecting the appropriate pressure, constructive interference of the generated harmonic waves along the propagation direction can be achieved, thereby maximizing the yield.

A major advantage of the SYLOS GHHG Compact configuration is its collinear geometry, which facilitates the implementation of IR–XUV and XUV–XUV pump–probe delays without the need to spatially separate the beams. The first delay is introduced by rotating a glass plate in the external IR arm, thereby adjusting the optical path (Fig. 3.15 (e)). The second delay is implemented using a bisected mirror pair (Fig. 3.15 (f)), which allows the two halves of the beam to be delayed relative to each other.

Both methods provide exceptional temporal and spatial stability, which is essential for long-duration measurements requiring fine temporal resolution. This collinear design ensures outstanding spatiotemporal stability, a critical factor for precision experiments, particularly those involving non-linear XUV–XUV interactions. The intrinsic alignment stability of the collinear layout minimizes the need for frequent recalibration and guarantees consistent experimental conditions over extended measurement campaigns.

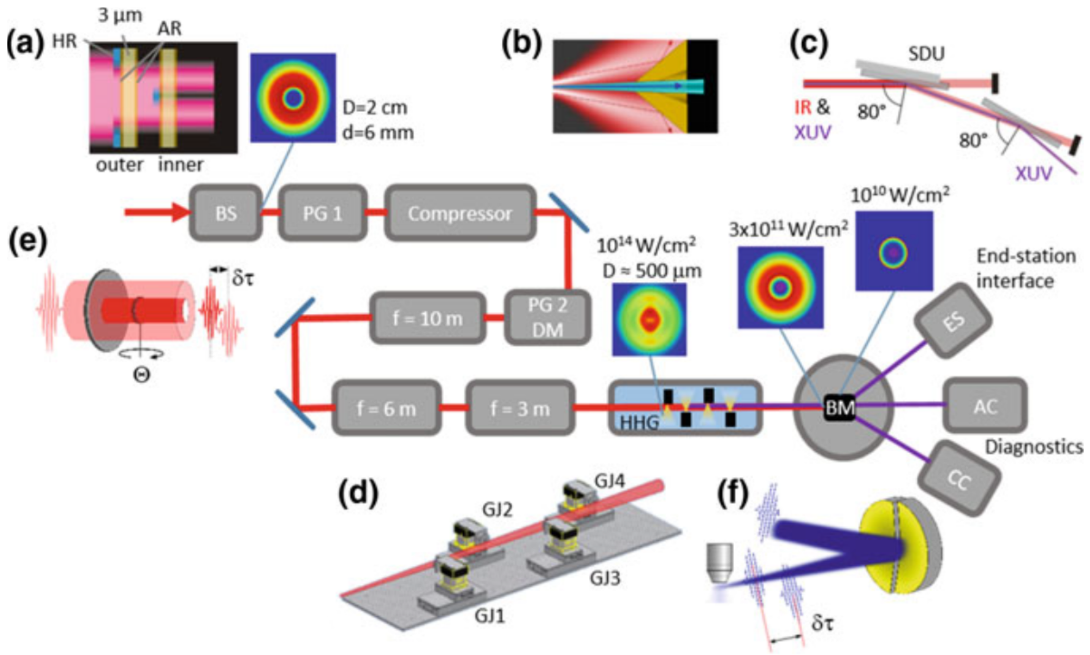

FIGURE 3.15: Compact beamline at ELI ALPS. The beam first passes through a mask (a), forming an annular profile, and is then compressed via reflections from chirped mirrors. The wavefront is optimized using a deformable mirror, after which the beam is focused by 3 m, 6 m, or 10 m focal-length mirrors into one or multiple pulse jets (d). Following generation, most of the residual IR can be removed with a skimmer (b), which images the mask in (a), while the remaining IR is further suppressed using reflection from a silica plate (c). The generated XUV pulse and the IR pump can be temporally delayed relative to each other by inserting a glass plate into the residual low-energy IR path (e). For XUV–XUV pump–probe measurements, a bisected mirror pair can be used to split the beam into two beamlets and introduce a controllable delay between them (f).

Figure 3.15 (a)) depicts the formation of an annular infrared beam profile through the use of a transmissive mask. This configuration enables the generation of high-order harmonics in the central axis of the annular IR beam. Following the generation process, residual infrared radiation must be effectively removed to isolate the XUV signal. As illustrated in Figure 3.15 (b), most of the IR radiation can be blocked by inserting a metallic skimmer downstream from the generation region, selectively allowing the centrally generated XUV beam to pass. To further enhance the suppression of the residual IR pulse, additional filtering can be achieved using specially coated silica plates. These coatings are designed to reflect the XUV efficiently while simultaneously transmitting most of the remaining infrared light, thereby providing an effective and compact method for spectral separation. This multilayer approach ensures high XUV contrast while preserving the beam's spatial and spectral properties, which is crucial for downstream experiments that rely on clean XUV pulses with minimal background from the driving IR field.

Downstream of the diagnostics stage, the beamline diverges into multiple branches, each dedicated to different types of experimental configurations. These include an end-station interface for general-purpose XUV applications, a dedicated section for nonlinear XUV studies, and a linear XUV measurement branch. This modular and highly adaptable design supports a wide range of experimental requirements, enabling cutting-edge research in ultrafast dynamics, attosecond science, and strong-field physics.

Figure 3.16 presents a comparison between the experimentally measured and numerically simulated high harmonic spectra. The experimental measurement was carried out using the SEA laser system (details about the system in section 2.2.1), which delivers ultrashort pulses with an energy of 30 mJ, a pulse duration of 13 fs, and a central wavelength centered at 840 nm. These parameters place the system well within the regime suitable for efficient HHG. The agreement between the experimental data and simulation validates the accuracy of the phase matching model and the numerical parameters used.

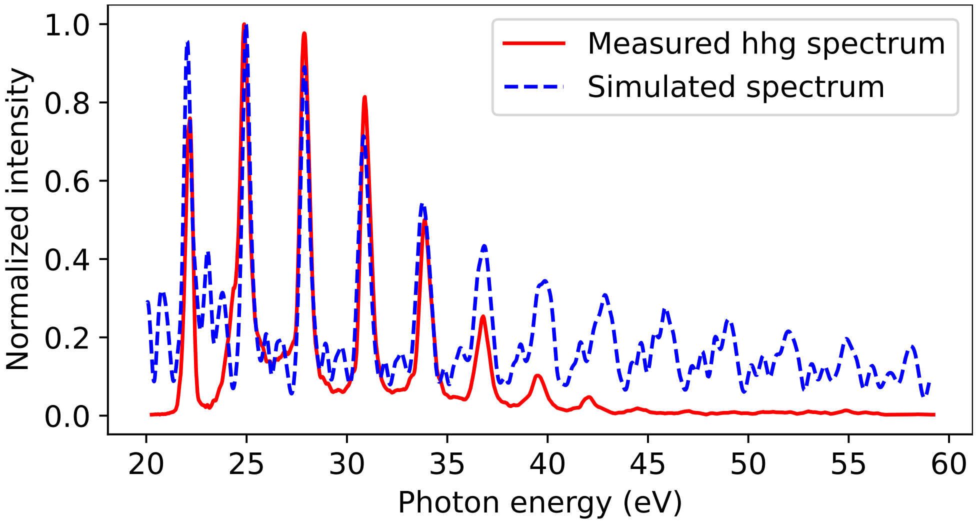

FIGURE 3.16: Comparison between the measured high harmonic spectrum (red line) and the simulated spectrum (dashed blue line) under optimized pressure conditions.

3.9.1 Temporal resolved measurement

Temporal dynamics of the gas density distribution can be measured similarly to the interferometric method case, by delaying the nozzle opening time compared to the time of the laser interaction.

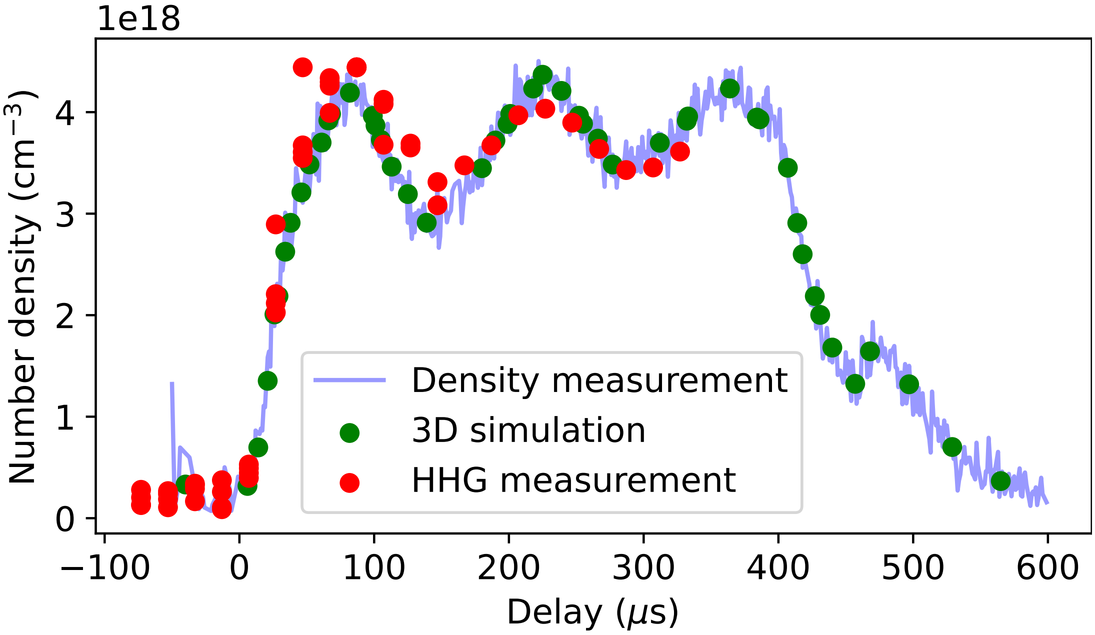

FIGURE 3.17: Comparison of two experimental methods and simulations for determining the temporal evolution of number density. The blue line shows interferometric measurements (as presented in Fig. 3.12), while the red dots represent XUV flux measured with a photodiode on the COMPACT beamline.

The harmonic yield was recorded using a calibrated photodiode, which integrates the emitted signal over the spectral transmission range defined by an aluminum filter—spanning from approximately 20 eV to 70 eV. This range encompasses the most prominent harmonics typically generated in noble gases under such conditions.

Figure 3.17 presents the simulated harmonic yield (green circles) as the function of the delay from the opening of the valve. The gas jet pressure for the simulation was calculated from the number density variation on Figure 3.12. Both the HHG measurements and simulations show a remarkable resemblance to the jet density variation measured with the interferometric technique. We note here that, in our simulations, the single atom response is calculated within the strong field approximation formalism, using the Lewenstein integral [64, 65, 155]. In this case, the relative intensity of the HHG spectra and hence the relative yield is calculated appropriately, but not in absolute photon numbers. To calculate the absolute conversion efficiency, one would need to solve the time dependent Schrödinger equation in 3D for the microscopic response, coupled with Maxwell's equations to take into account the propagation effects. The computational cost of such an implementation is tremendously high, and it is far beyond the scope of the current manuscript. In the simulations carried out here, we focus on the relative HHG yield to compare with the experiments, and for this purpose this well-established computational approach suffices.

The simulation method described above assumes radial symmetry around the laser propagation axis. For the laser spatio-temporal profile, we use the measured focal spot distribution and experimental laser pulse duration in order to mimic the real experimental conditions.

The simulations also revealed that under the circumstances that describe these experiments, transient phase matching [156, 157] limits efficient generation to the first half of the short laser pulse. At the same time, due to minimal reshaping of the pulsed laser beam, there are spatially homogeneous phase matching conditions in the whole interaction volume. This allows us to apply a simple model [80] to explain the variation of the observable harmonic flux in the absorbing medium.

3.9.2 Laser induced strong-field ionization gas jet characterization

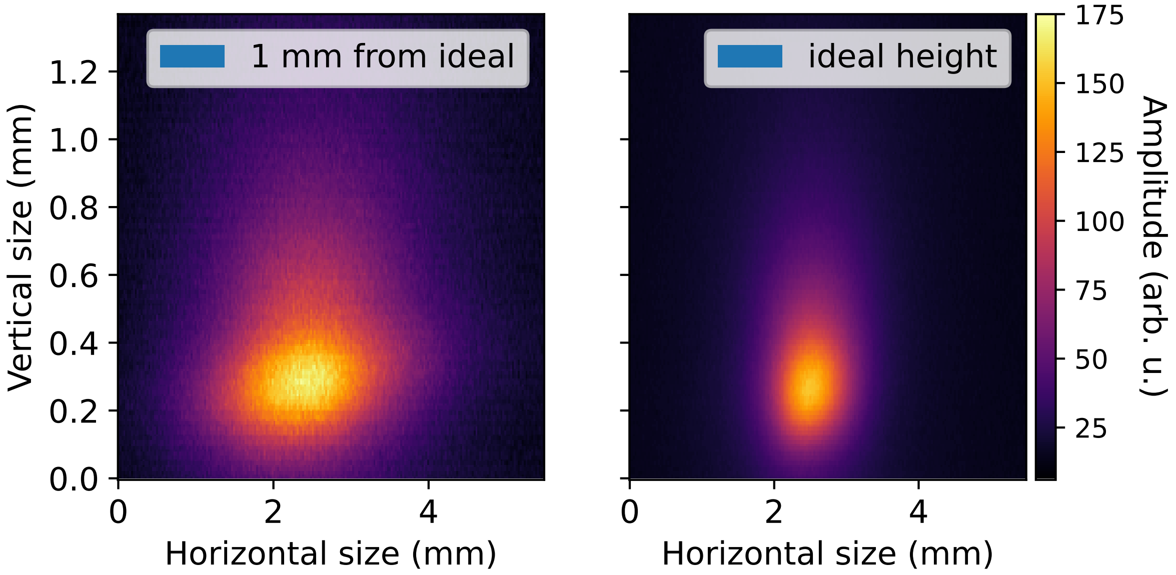

Figure 3.18: Captured laser plasma images. To achieve axial number density information, the gas source had been moved vertically relative to the laser focus. Figure (b) shows the recorded frame at the highest brightness value, while (a) recorded when the source moved 1 mm downwards. The focal point size had been around 400 µm for both cases.

At high intensities, the electric field of the laser becomes sufficiently strong to ionize the gas, resulting in the formation of a laser-induced plasma. The characteristics of the plasma emission—both in terms of brightness and spectral content—depend sensitively on the local laser intensity as well as the spatial distribution of the gas density [158]. Because the intensity of the emitted light correlates with the local gas density under known excitation conditions, this emission can be used as a diagnostic tool to characterize the gas target *in situ*. In principle, this method can provide absolute gas density measurements, provided that all relevant parameters of the interaction—such as laser pulse energy, beam profile, focal geometry, and gas composition—are precisely known [159]. However, achieving such a level of control is non-trivial in experimental systems utilizing high-power laser sources and loose focusing geometries, where small variations in alignment or pulse parameters can have significant effects on the local intensity distribution. Recorded images while the laser and the gas jet position is different along the gas jet symmetry axis can be seen on figure 3.18.

Nevertheless, since the gas source has already been characterized through independent interferometric techniques, as detailed in Section 3.6, the plasma observation-based method can be employed in a complementary manner. It provides a valuable cross-validation mechanism and enables dynamic, real-time monitoring of the gas density during HHG experiments. An additional advantage of this technique lies in its geometric flexibility. The light emitted during ionization is radiated isotropically, which allows for straightforward detection along directions transverse to the laser propagation axis. This facilitates the implementation of online diagnostics without the need for complex optical arrangements. By translating the gas jet along the nozzle axis while keeping the laser beam fixed and aligned to the same axis, one can record the intensity of the plasma-induced emission as a function of position. This scanning approach enables the mapping of the gas density distribution with spatial resolution in the interaction region.

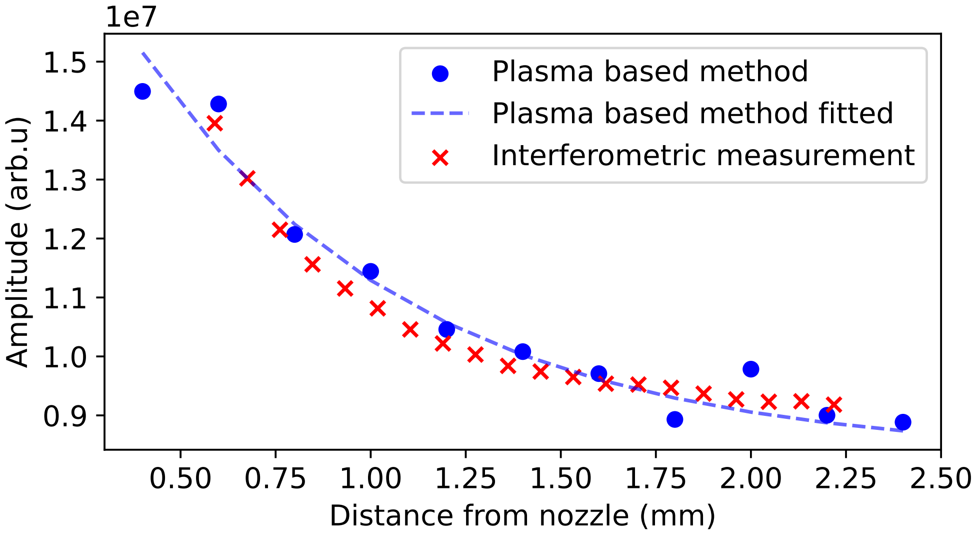

Figure 3.19: Comparison of phase retrieval along the vertical axis using different techniques. The blue dots represent results obtained with the plasma-based method, which are fitted with an exponential function shown as the blue dashed line. The red crosses indicate the reference measurement performed with the interferometric technique.

Experimental results obtained through this laser plasma-based method show good agreement with the gas density profiles reconstructed using interferometric measurements, this can be seen on Figure 3.19. The agreement between the two techniques shows the consistency and reliability of the in-situ plasma-based technique for monitoring gas jet characteristics under high-intensity laser interaction conditions.

3.10 Summary

These findings have broad relevance across several areas of research that rely on high-repetition-rate gas jets. A precise knowledge of the gas density profile is crucial, as many characteristic effects of the underlying phenomena are highly sensitive to it. For instance, applications range from molecular and atomic quantum path interferometry [66, 160], and ion spectroscopy in dilute plasmas [161, 162], to the spatio-temporal shaping of attosecond pulses [163] and their spatio-spectral control [164, 165]. Moreover, such control is also significant in the development of gas-based refractive optics for the extreme ultraviolet regime [166].

T2 As part of my work, I carried out a complete spatial and temporal characterization of cantilever piezo gas valves, which are employed for high-harmonic generation and spectroscopy experiments in both the SYLOS GHHG Long and SYLOS GHHG Compact beamlines. To achieve this, I designed and constructed a stand-alone gas characterization end station, enabling precise measurements independent of the main beamline operation. I simulated interferometric fringe patterns corresponding to the expected gas density distributions and developed a dedicated data analysis code capable of retrieving accurate atomic number density profiles in the interaction region from these measurements. I validated the approach against the experimental data and ensured its applicability to a wide range of operational conditions. Furthermore, I designed the system to be adaptable for different gas delivery configurations, including slit nozzles or multiple gas jets aligned in series, thus extending its utility for future experimental setups and user requirements. The results related to this, published in [P1]

T3 I conducted a series of measurements to verify the gas density results under realistic experimental conditions relevant to both high-harmonic generation and plasma generation. For the HHG verification, I performed dedicated simulation runs replicating the experimental geometry and operational parameters of the stand-alone gas characterization end station. The simulated results showed excellent agreement with the measured data, thereby confirming the accuracy and reliability of the density retrieval method. In parallel, I investigated plasma emission as a diagnostic tool to monitor potential variations in gas pressure during extended operation. This approach provided a practical, real-time monitoring tool, enabling the detection of gradual drifts or fluctuations in the gas delivery system without interrupting the experiment. This experimental result is presented in [P1].

Chapter 4

Machine learning aided CEP detection

4.1 Carrier-Envelope Phase measurement

CEP is a fundamental parameter for the characterization and control of ultrashort laser pulses, especially in the few-cycle regime. An ultrashort pulse can be described as a rapidly oscillating carrier wave under a slowly varying envelope, with the CEP defining the phase offset between the envelope maximum and the nearest peak of the carrier wave. For longer pulses ($\gtrsim 5$ cycles) this phase is negligible, but in few-cycle pulses ($\ll 2$ cycles) even a small CEP shift can drastically alter the instantaneous electric field profile. A mathematical description is provided in Section 1.2.8. Since this phase offset is both subtle and subject to shot-to-shot fluctuations, its measurement is highly nontrivial. Two main approaches exist.

4.1.1 Stereo ATI

A widely used time-domain method for measuring the absolute carrier-envelope phase relies on above-threshold ionization (ATI), a multiphoton ionization process occurring at high laser intensities well above the Coulomb field limit ($\gamma \gg 1$, with the Keldysh parameter γ defined in Section 1.2.1). Experimentally, this is realized by tightly focusing the laser into a gas jet and collecting the ejected electrons with two opposing time-of-flight detectors, an arrangement commonly referred to as stereo-ATI. Example results recorded at ELI ALPS with the HR-1 laser are shown in Fig. 4.1.

As the laser field oscillates, electrons are emitted in both directions and detected simultaneously. To quantify the directional asymmetry, the asymmetry parameter is defined as

$$A(E) = \frac{N_L(E) - N_R(E)}{N_L(E) + N_R(E)}, \tag{4.1}$$

where $N_L(E)$ and $N_R(E)$ denote the electron yields in the left and right detectors, respectively. Low-energy electrons are particularly sensitive to the temporal envelope of the laser pulse, whereas high-energy electrons primarily reflect the strongest half-cycle of the field. The dependence of this asymmetry on the CEP makes stereo-ATI a highly sensitive diagnostic [167]. When the CEP is stabilized, the measured asymmetry values cluster in a well-defined region (Fig. 4.1 (a)), while for fluctuating CEP the asymmetries trace out an entire ellipse-like pattern (Fig. 4.1 (b)).

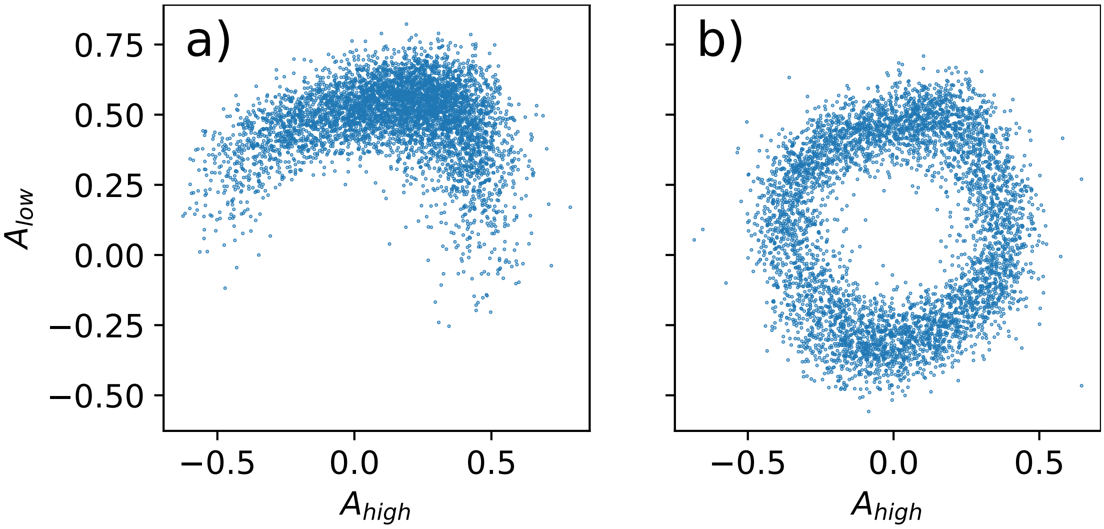

FIGURE 4.1: Stereo ATI measurement for CEP stability using the HR-1 laser. Panel (a) shows a trace with 500 mrad stability, while panel (b) corresponds to 1700 mrad instability.

The main advantage of stereo-ATI lies in its inherently single-shot capability and its applicability at any wavelength capable of ionizing the chosen medium. However, it requires relatively high pulse energy, operation under vacuum conditions, and sophisticated detection electronics. Additionally, real-time CEP stabilization using this method is challenging due to the complexity of the data evaluation process, which involves extracting the asymmetry parameters from the measured electron distributions.

4.1.2 f-2f Interferometry

CEP can also be measured in the frequency domain using f-to-2f interferometry [168]. In this method, a portion of the pulse spectrum is frequency-doubled and interfered with another portion of the fundamental spectrum, allowing extraction of the CEP shift from the resulting interference signal. This signal is typically fed back to a stabilization loop, which may involve a piezo-controlled mirror or an acousto-optic modulator within the laser oscillator or amplifier chain. Compared to stereo-ATI, this approach offers a simpler and more compact solution, although single-shot measurements are not straightforward.

Long-term CEP stability requires careful isolation from environmental noise, thermal drifts, and mechanical vibrations. Additional CEP drifts can also arise during nonlinear propagation or pulse compression, particularly in hollow-core fiber compression or filamentation. Therefore, CEP monitoring after the final compression stage is essential for high-fidelity phase control in experiments.

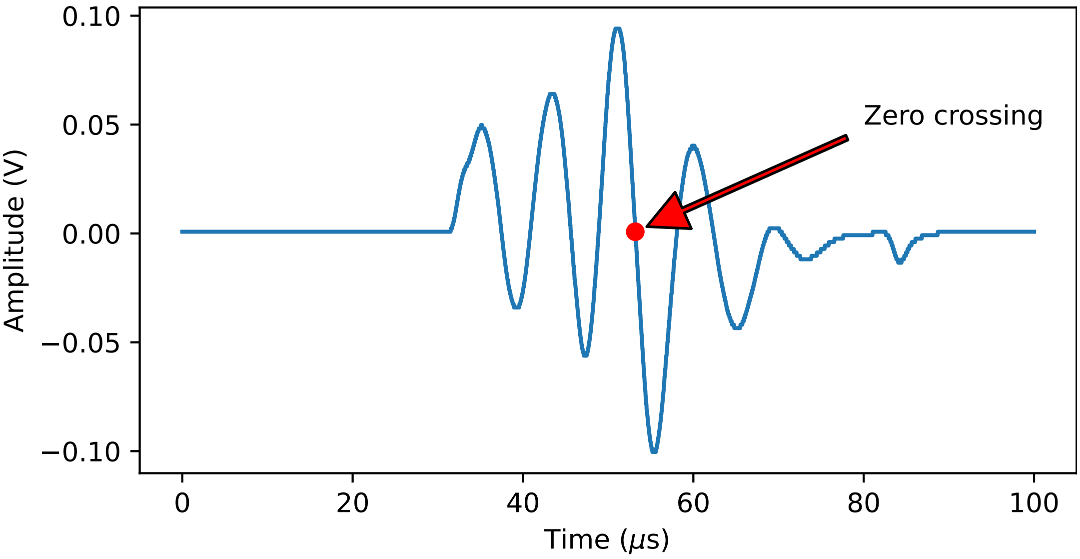

FIGURE 4.2: Measured interference pattern between the fundamental and its second harmonic. The CEP measurement and stabilization are based on the position of an arbitrarily selected zero-crossing, indicated by the red dot.

As the technique relies on frequency doubling the pulse and interfering the second harmonic with the fundamental, a nonlinear crystal with sufficient bandwidth must be available for the laser wavelength in use. While suitable crystals exist for IR and MIR pulses, they are generally unavailable for UV or THz radiation. The zero-crossing of the interference signal (Fig. 4.2) can be monitored using analog electronics, enabling rapid CEP evaluation at rates in the hundreds of kHz or even MHz. In our experiments, a commercial fast CEP-tagging device (Fringeezz, by FastLite) [169] was used. Because the measurement is referenced to a single zero-crossing, it provides only the relative CEP. Compared to stereo-ATI, this approach requires significantly less pulse energy and can be conveniently implemented within the laser system after a simple beam sampler.

This technique relies on frequency doubling the pulse and interfering the second harmonic with the fundamental. Therefore, a nonlinear crystal with sufficient bandwidth must be available for the given laser. While suitable crystals exist for the IR and MIR ranges, they are not available for UV or THz radiation. Monitoring the zero-crossing (Fig. 4.2) can be realized with analog electronics, enabling CEP evaluation at very high rates — in the hundreds of kHz or even MHz range. Since the measurement is referenced to the zero point, it provides only the relative CEP. Compared to stereo-ATI, this approach requires significantly less pulse energy and can be conveniently implemented within the laser system after a simple beam sampler.

4.2 CEP Dependence of High Harmonic Generation in Gases

The relationship between CEP and the high-harmonic spectra in gas-phase HHG is highly nonlinear and intricate. This dependence arises from the strong-field nature of the interaction, where even slight variations in the CEP can lead to significant changes in the resulted dipole response. Consequently, the spectral phase, intensity modulation, and cutoff energy of the generated harmonics exhibit pronounced sensitivity to the CEP, particularly when ultrashort few cycle laser pulses are employed. Understanding and characterizing this dependence is crucial for optimizing experimental conditions and for developing robust CEP retrieval and stabilization techniques.

Given the complexity of the CEP influence on the HHG process, it is highly advantageous to perform comprehensive numerical simulations before conducting experiments. Such simulations provide a predictive understanding of how the CEP modulates the harmonic yield and structure, enabling the evaluation and validation of phase-sensitive diagnostic methods under well-controlled conditions. For the experimental realization, we aim to utilize the SYLOS2 laser system [170], operated in conjunction with the SYLOS GHHG Long beamline [106] infrastructure at ELI ALPS (section 2.2. This state-of-the-art laser system is capable of delivering pulses with energies up to 25 mJ and durations as short as 7 fs at a central wavelength of 825 nm, corresponding to approximately 2.5 optical cycles. The beamline is optimized for long-focal-length operation, employing an 18-meter focusing geometry that enables intensity control within the 1–5 $\mathrm{TW/cm^2}$ range at the interaction region.

The extended focusing geometry results in a confocal parameter of approximately 30 cm. To match this spatial intensity profile, the HHG medium is confined within an adjustable-length gas cell designed to span lengths from 32 to 72 cm. This configuration ensures that the gas target occupies the high-intensity portion of the focal region, facilitating efficient harmonic generation while maintaining favorable phase matching conditions. The numerical tool employed to model CEP-sensitive HHG is described in detail in Section 1.3. To systematically investigate the role of CEP, we performed parametric scans across a full 2π phase range for different pulse durations, corresponding to 0.9 optical cycles (2.835 fs) and 2.5 optical cycles (7 fs) at 825 nm. In these simulations, all experimental parameters other than pulse duration were held constant. While this inherently results in slightly higher peak intensities for the shorter pulses, the comparative analysis remains valid, as the intensity variation does not qualitatively alter the trends observed in CEP sensitivity. The resulting spectra, shown in Figure 4.3, clearly demonstrates the amplified CEP sensitivity for the shorter, 0.9-cycle pulses.

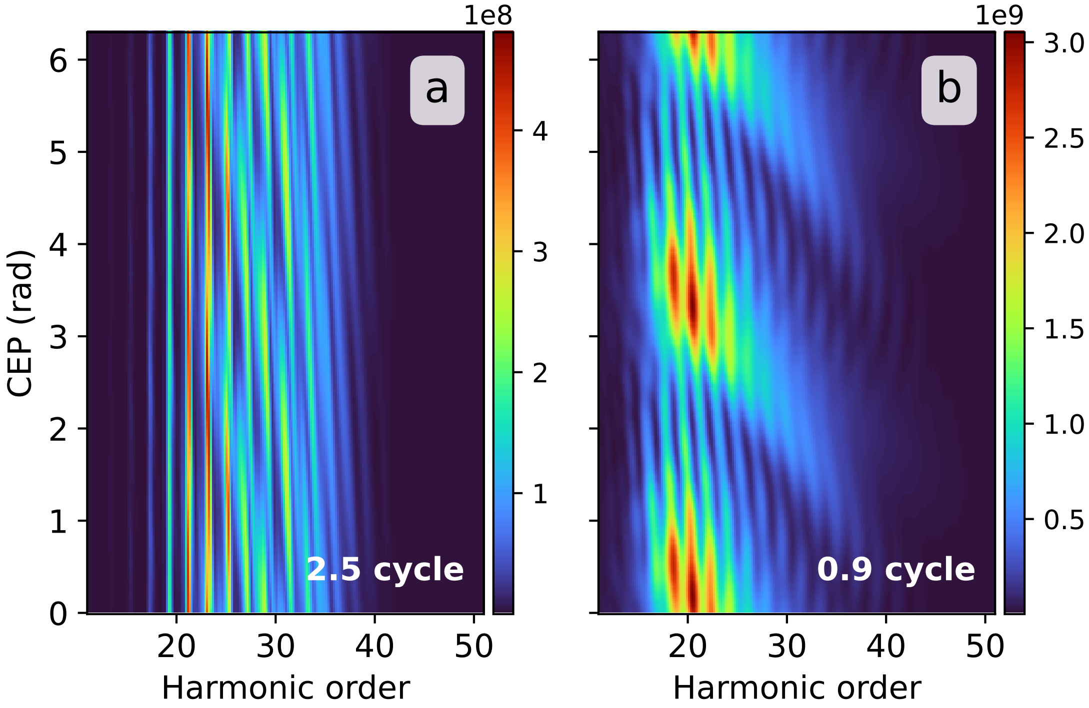

FIGURE 4.3: Simulated CEP-dependent spectra are shown for laser pulses of different durations. In panel (a), the driving laser has a pulse duration corresponding to 2.5 carrier cycles, while in panel (b) a much shorter, 0.9-cycle pulse is applied. Although some CEP dependence is visible in the case of the longer pulse, this effect becomes much stronger for the shorter pulse, where variations in CEP lead to significant changes in the resulting high-harmonic spectra.

Pronounced modulation in the spectral intensity, harmonic cutoff, and spectral shaping can be observed across the phase scan. In contrast, the 2.5-cycle pulse simulations show relatively reduced CEP dependence, as the averaging over multiple optical cycles diminishes the influence of the absolute carrier-envelope phase. These results not only highlight the importance of pulse duration in CEP-dependent HHG, but also underscore the need for precise phase stabilization and characterization in few-cycle laser systems aimed at generating isolated attosecond pulses or conducting ultrafast spectroscopy.

The coherence of this emission process across multiple cycles gives rise to the well-known pattern of odd harmonic orders. It is possible to generate isolated attosecond pulses by spectrally filtering the high-energy cutoff region of the harmonic spectrum [27], where the spectrum is continuous. However, such a technique is often accompanied by limitations, including significantly reduced photon flux and restricted spectral bandwidth, which may compromise the efficiency and applicability of the attosecond source [171].

In the ideal single-cycle pulse with a sine-like carrier-envelope configuration, the HHG process is confined to a single half-cycle of the field (Figure 4.4), resulting in the generation of a clean, broadband attosecond pulse. However, the realization of such ideal driving conditions remains technologically demanding, especially in the near-infrared regime and for high-energy laser systems, where dispersion management, optical damage thresholds, and gain bandwidths impose practical limitations.

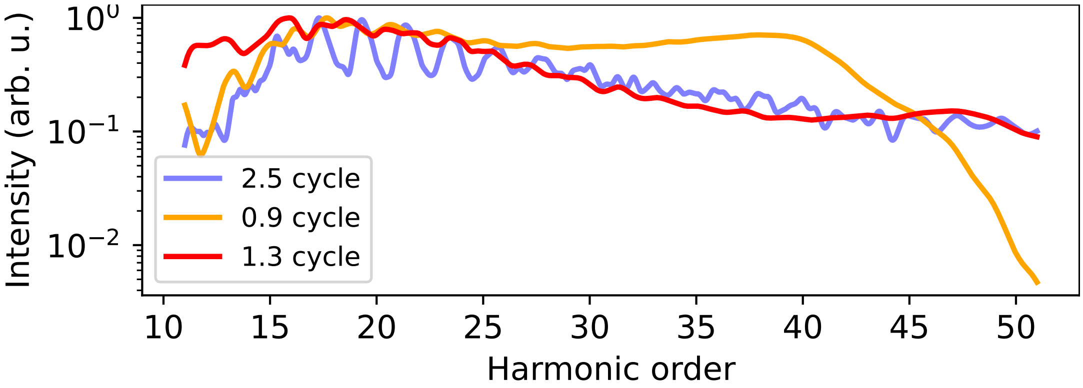

FIGURE 4.4: Simulated HHG spectra with different duration laser pulses. Around the cutoff, the spectra become continuous as the driving fundamental pulse becomes shorter.

At ELI ALPS facility [107–109], significant progress has been achieved toward this objective. Using the SEA laser, pulse durations as short as 4 fs—corresponding to roughly 1.4 optical cycles—have been demonstrated [20] on a dedicated endstation. These pulses already enter the regime in which HHG becomes strongly dependent on the CEP and enable the possibility of generating isolated attosecond bursts. However, integrating the required optics into the SYLOS GHHG Long beamline remains a challenge, as the setup demands a substantial footprint and the management of such a broad spectrum at high pulse energies is technically demanding. Also, the higher repetition rate of the SYLOS laser would be important for pump and probe measurements, creating sub 4 fs pulses with this laser yet to be demonstrated.

4.3 Machine Learning-Based Regression Models for Scientific Applications

The rapid development of machine learning (ML) techniques has opened new avenues for addressing complex regression problems in scientific research [172, 173]. Regression models, which aim to predict continuous outputs from a given set of input features, have long been foundational in data analysis [174–176]. However, traditional statistical methods often struggle with nonlinear relationships, high-dimensional data, and noisy environments that are common in modern scientific experiments. Machine learning-based regression models, particularly those employing supervised learning paradigms, offer powerful alternatives that can capture intricate dependencies between variables, enabling more accurate predictions and deeper understanding of underlying physical phenomena.

In scientific contexts, machine learning tasks, including regression, appear in a wide range of domains. For instance, in materials science, machine learning is employed to predict the band gap [177], mechanical strength [178], or thermal conductivity [179] of novel compounds based on compositional and structural descriptors [180]. In fluid dynamics, machine learning models are used to approximate solutions to the Navier-Stokes equations [181] under various boundary conditions, providing real-time estimation of flow fields [182]. In optical physics, ML-based regression can estimate pulse characteristics such as duration, chirp, and peak intensity from indirect measurements, thereby simplifying diagnostics [183–185]. In astronomy, the models can predict stellar parameters such as temperature, metallicity, and luminosity from spectral data [186, 187].

Several types of machine learning models have proven effective for regression in scientific settings. Linear regression [188, 189] remains a useful baseline for interpretable models, especially when paired with regularization techniques like ridge or LASSO (Least Absolute Shrinkage and Selection Operator) [190] to handle multicollinearity. However, many scientific relationships are inherently nonlinear. Neural networks, particularly deep feedforward and convolutional architectures, can approximate arbitrarily complex functions given sufficient data and training. Kernel-based methods such as support vector regression (SVR) offer strong performance in moderate-dimensional spaces by leveraging similarity measures. Ensemble methods, such as random forests and gradient-boosted trees, provide robustness and strong generalization, particularly when the input features are heterogeneous or exhibit nonstationary distributions and are more protected from overfitting.

One of the main advantages of ML regression in science is the ability to incorporate high-dimensional data without requiring explicit models of the system. For example, hyperspectral imaging data, time-series measurements, or volumetric simulations can all be used directly as input, provided an appropriate feature extraction or dimensionality reduction step is included. Techniques such as principal component analysis (PCA), autoencoders, and t-distributed stochastic neighbor embedding (t-SNE) are often employed in preprocessing pipelines to uncover latent structures in the data. This flexibility allows scientists to move beyond simplified models or limited analytical approximations and instead leverage empirical relationships directly learned from experimental or simulated datasets. Despite their power, machine learning regression models come with challenges in scientific applications. Overfitting is a critical concern, particularly when data is limited or when noise levels are high. Careful cross-validation, regularization, and model selection must be applied to ensure that predictions generalize well to unseen data. Interpretability is another significant issue. While models such as decision trees [176] or linear regressions are naturally interpretable, complex architectures like deep neural networks [191, 192] are often treated as black boxes. These support our choice of ExtraTree model [193] in the following chapters.

4.4 ML based CEP prediction for gas harmonics

An alternative approach for determining the CEP of ultrashort laser pulses involves the analysis of the HHG spectra produced by these pulses. Due to the complex and highly nonlinear dependence of the HHG spectrum on the CEP, direct analytical inversion or parametric fitting methods are often insufficient or unreliable for precise CEP estimation. This challenge underlines the necessity for advanced strategies capable of decoding the implicit CEP information encoded in the spectral features of the generated harmonics. One such promising strategy is the use of data-driven techniques, particularly those based on machine learning regression models.

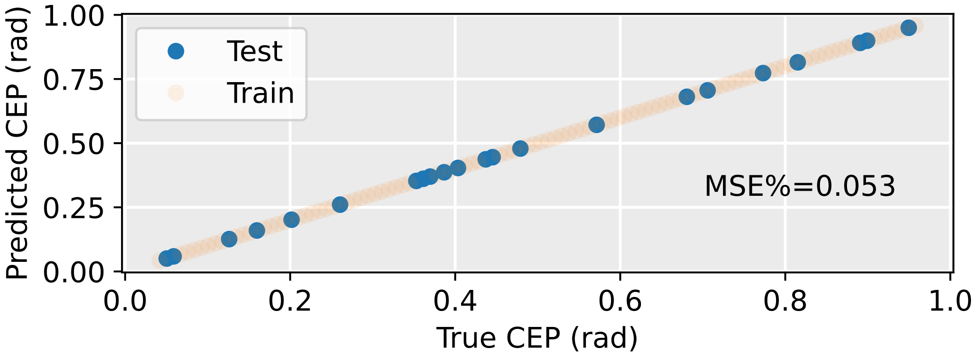

FIGURE 4.5: Results of the ML model trained on the simulated gas HHG dataset. The data were split 80%–20% into training and testing sets. The figure shows a low test MSE%, validating the approach.

Machine learning methods, particularly supervised regression algorithms, offer a flexible framework for learning the mapping between spectral signatures and corresponding CEP values. By constructing a training dataset composed of HHG spectra paired with known CEP values, a regression model can be trained to learn the underlying correlations. Once trained, this model can be used to infer the CEP corresponding to previously unseen spectral inputs, effectively allowing the retrieval of CEP values from experimental HHG data. To validate this approach, a comprehensive numerical simulation of HHG was conducted in which the CEP was systematically varied across a full 2π range. The resulting spectral data were divided into two subsets: a training set, used to build the regression model, and a test set, containing randomly selected CEP values excluded from the training data. Since the test values were not present during the training phase, the model's task resembles interpolation, where it must predict the CEP based on previously observed input-output relationships.

The Mean Squared Error (MSE) is a common loss function in regression tasks defined as

$$\mathrm{MSE} = \frac{1}{N}\sum_{i=1}^{N}\left(y_i - \hat{y}_i\right)^2, \tag{4.2}$$

where y_i and $\hat{y}_i$ are the true and predicted values, respectively, and N is the total number of samples. It measures the average squared difference between predicted and actual values, penalizing large errors more strongly.

For phase values, which are naturally defined modulo 2π, it is convenient to normalize the error so that it falls within a standard range between 0 and 1. To achieve this, MSE% for phases, denoted as MSE%, is defined as

$$\mathrm{MSE\%} = \frac{\sqrt{\mathrm{MSE}}}{\pi}. \tag{4.3}$$

This definition has a clear rationale: taking the square root converts the MSE from squared units to the same units as the phase (radians), making the error directly interpretable. Dividing by π then normalizes the error to the full phase range, naturally bounding MSE% between 0 and 1. In this way, MSE% provides a convenient, unitless metric for quantifying phase prediction accuracy, where 0 represents perfect agreement and 1 corresponds to the maximum possible phase deviation.

The results of this machine learning-based prediction are illustrated in Figure 4.5. The simulations were performed using 4.3 fs (1.5-cycle) pulses at a central wavelength of 840 nm. The dataset consists of 120 spectra and was randomly split into training and testing subsets, with 80% of the data used for training and the remaining 20% for testing.

Even with a relatively modest number of training examples, the regression model demonstrates remarkable accuracy, achieving an MSE% of approximately 0.053%. This means, that even in the case of these relatively long pulses the CEP maps one-to-one with the high harmonic spectrum, making the technique applicable for real circumstances.

At ELI ALPS, near single-cycle pulse durations have been demonstrated using a mid-infrared laser [194]. Using this laser, the group of Mathias Kübel showed the CEP dependence of HHG in ZnO crystals [195]. To test our hypothesis that a machine learning model can estimate the CEP from HHG spectra, we perform experiments on HHG from bulk crystals driven by the mid-infrared laser.

4.5 CEP Dependence of HHG in solid

The theory of solid HHG had been briefly introduced in section 1.4. To understand the CEP dependence, one has to use length gauge, where intra-band and inter-band transitions can be discussed separately.

In gases, high-harmonic generation is highly sensitive to CEP, since the ionization and recombination times depend directly on the instantaneous electric field of the laser. In the case of interband high-harmonic generation in solids, the harmonic emission arises from the coherent recombination of electron-hole pairs that have been excited across the band gap [101]. Once excited, the electrons and holes traverse the conduction and valence bands according to the crystal's band structure. The resulting emission is determined primarily by the energy dispersion and symmetry of the bands, which are periodic in the crystal lattice. Because these properties are intrinsic to the material and largely independent of the absolute phase of the driving carrier wave, the overall harmonic response is not strongly sensitive to the carrier-envelope phase.

The intraband current follows the time dependence of the band structure. Emission occurs at points of largest band curvature, which correspond to instants when the vector potential vanishes, i.e. when the electric field reaches an extremum [101]. The symmetry properties of the target material strongly influence the harmonic response to changes in CEP.

In the case of a randomly distributed interatomic structure on a scale much smaller than the laser wavelength, the harmonic spectrum exhibits a π-periodicity with respect to CEP. This arises because each half-cycle of the driving field produces, on average, the same response, as observed for fused silica [196].

In contrast, for non-centrosymmetric crystals, each half-cycle of the driving field experiences a different collective response. This leads to a 2π CEP dependence of the emitted harmonics. Such a one-to-one mapping between laser CEP and the HHG spectrum requires a crystal with broken inversion symmetry. In our experiments, we therefore chose zinc oxide (ZnO) as the target material. ZnO, being a non-centrosymmetric crystal, supports both even and odd harmonics. Therefore, while interband HHG [195] and gas-phase HHG [197] can exhibit strong CEP dependence, intraband HHG in solids remains essentially insensitive to the CEP [198].

4.6 Simulation Support and Model Performance for Solid-State High Harmonic Generation (SHHG)

Although the comprehensive setup and execution of the numerical simulations presented here fall beyond the direct scope of this thesis work, it is essential to provide a brief overview of the associated efforts as they significantly support and validate the experimental measurements. Detailed descriptions and methodologies related to the simulations can be found in ref [199] which includes an in-depth discussion of the numerical framework and its theoretical underpinnings.

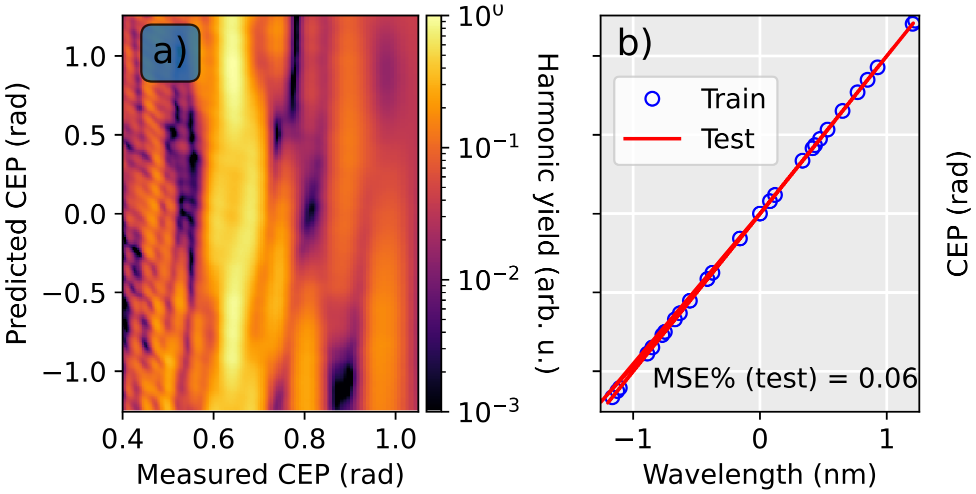

FIGURE 4.6: A theoretical CEP scan was performed in ZnO using an 19 fs pulse at an intensity of 1.36×10^{12} W/cm^2 and a central wavelength of 3.2 μm. Figure (a) shows the simulated HHG spectrum in the solid-state medium, together with the corresponding machine-learning-based CEP regression (b). Similarly to the gas-phase case, with 400 training points the MSE% is already low, reaching a value of 0.06%, which corresponds to a regression line with a slope close to the ideal 45° diagonal.

An example result, analogous to that shown in Figure 4.4 for the gas-phase case, is illustrated in Figure 4.6 (a)).

This figure depicts the simulated HHG spectrum obtained using a mid-infrared driving pulse with 3.2 µm central wavelength with 19 fs pulse duration and 80 µJ pulse energy, alongside the corresponding machine learning model predictions. Notably, the success of the machine learning-based CEP estimation in the solid-state regime demonstrates that the approach remains valid despite the more intricate spectral structure commonly observed in solid harmonics compared to their gas-phase counterparts.

It is also important to highlight the fundamental difference in the periodicity of CEP sensitivity between gas and solid media. Figure 4.7 presents the performance comparison of various regression models trained on datasets of different sizes. Among the models evaluated, the Extra Trees (ExtraTree) [193] regressor was found to be particularly effective. Even with a relatively modest dataset comprising only 100 training points, the model achieved high prediction accuracy, indicating its robustness and efficiency in capturing the complex mapping between spectral features and CEP values. The model's low prediction error highlights its suitability for experimental applications where extensive datasets may not always be feasible to acquire. Additionally, the simulations investigated

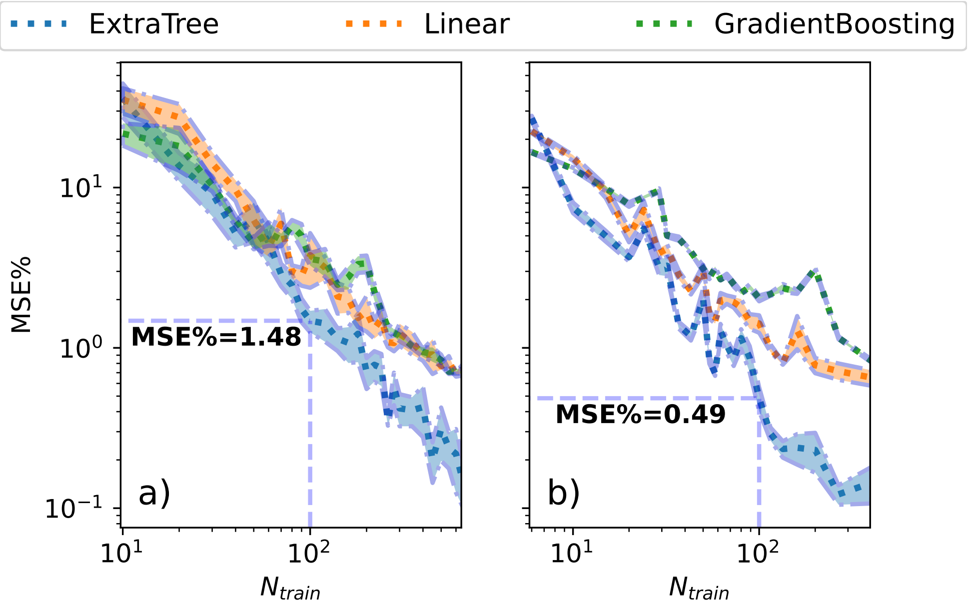

FIGURE 4.7: A comparative analysis of model predictive accuracy using two training data sampling strategies: (a) random and (b) equidistant CEP sampling. Predictive precision is evaluated based on the MSE% of a linear fit applied to predictions from 150 test datasets, each with randomly selected novel CEP values.

the influence of training set distribution on model performance. Specifically, two sampling strategies were compared: randomly spaced and equidistantly spaced CEP values. The results indicate that equidistant sampling yields significantly improved performance over random spacing for the same dataset size. This finding has practical implications for the experimental implementation of CEP tagging using machine learning, suggesting that a deliberate choice of training data spacing can enhance the model's predictive accuracy and reliability.

4.7 Experimental setup

The high-harmonic generation experiments presented in this work were conducted using the mid-infrared laser system at ELI ALPS [200]. This laser operates at a central wavelength of 3.2 µm, with a high repetition rate of 100 kHz and a pulse energy of up to 140 µJ. A typical measured spectrum of the MIR driving field is displayed in Figure 4.10 (a). The laser pulses initially have a temporal duration of approximately 45 fs, which corresponds to several optical cycles at this wavelength. To achieve sub-two-cycle pulses, spectral broadening was implemented using nonlinear propagation through a combination of barium fluoride (BaF_2) and silicon (Si) optical windows (Figure 4.8). Subsequent pulse compression was carried out using additional bulk BaF_2 windows along with a set of three dispersive mirrors exhibiting negative third-order dispersion (TOD). This configuration enabled the generation of laser pulses with durations as short as 18 fs, equivalent to approximately 1.4 optical cycles at 3.2 µm.

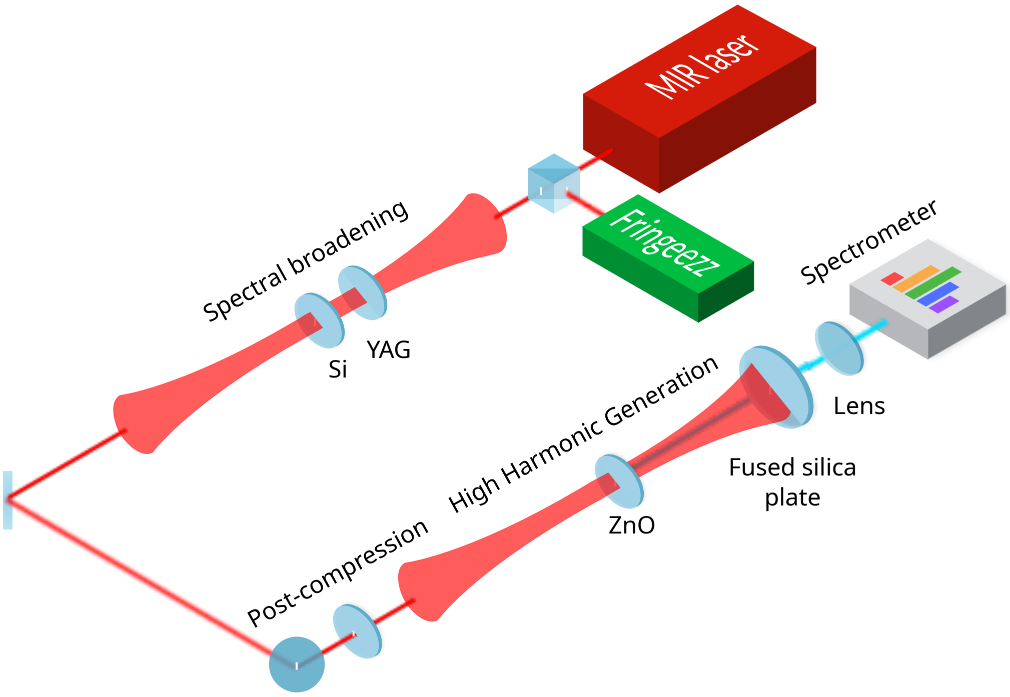

FIGURE 4.8: Schematic experimental setup. The pulses from the MIR laser broadened spectrally and post-compressed, then HHG takes place in a ZnO crystal. The CEP tagging takes place on a sampled beam right after the laser system with a commercial device for CEP tagging, called Fringeezz, which can be installed after an f-2f interferometer. To filter out the mid-infrared pulses before the visible spectrometer, fused silica plates are applied.

Accurate temporal characterization of these ultrashort pulses was essential and was performed using the TIPTOE technique [201]. The diagnostic beam was extracted prior to the focusing optics via a beam splitter, allowing undisturbed measurement of the temporal electric field envelope. Since HHG in solids is strongly CEP-dependent, particularly for few-cycle pulses, carrier-envelope phase stabilization and tagging were imperative. To this end, we employed the Fringeezz, which can be installed after an f–2f interferometric setup, and can provide fast CEP detection using analog electronics. Operating at 10 kHz, this system provides shot-to-shot CEP measurements and was used to close the feedback loop controlling an acousto-optic programmable dispersive filter (AOPDF, Dazzler, Fastlite [116]) within the OPCPA front-end. This feedback mechanism ensured CEP stabilization, better than 100 mrad RMS over long acquisition times. For the HHG process itself, we used a 90 µm-thick single-crystal ZnO target. Several crystallographic cuts are available for ZnO. The c-cut crystal possesses inversion symmetry and therefore generates only odd-order harmonics [202], whereas the a-cut variant allows the generation of both even- and odd-order harmonics. In this work, we used the latter.

The MIR pulses were focused onto the crystal surface using an off-axis parabolic mirror with a focal length of 100 mm. At full compression, the on-target pulse energy was 1.3 µJ, yielding an estimated peak intensity of approximately 1.3×10^{12} W/cm^2. To explore the influence of intensity on the harmonic emission, chirped pulses were also applied, which reduced the peak intensity to around 6.6×10^{11} W/cm^2.

4.8 Experimental results

Following post-compression, the duration of the laser pulse was reduced to below two optical cycles. To characterize such ultrashort waveforms in the time domain, we employed the technique of Tunneling Ionization with a Perturbation for the Time-domain Observation of an Electric field (TIPTOE) [203]. This method provides a direct, field-resolved measurement of the electric field of ultrashort laser pulses based on the nonlinear response of gas-phase media.

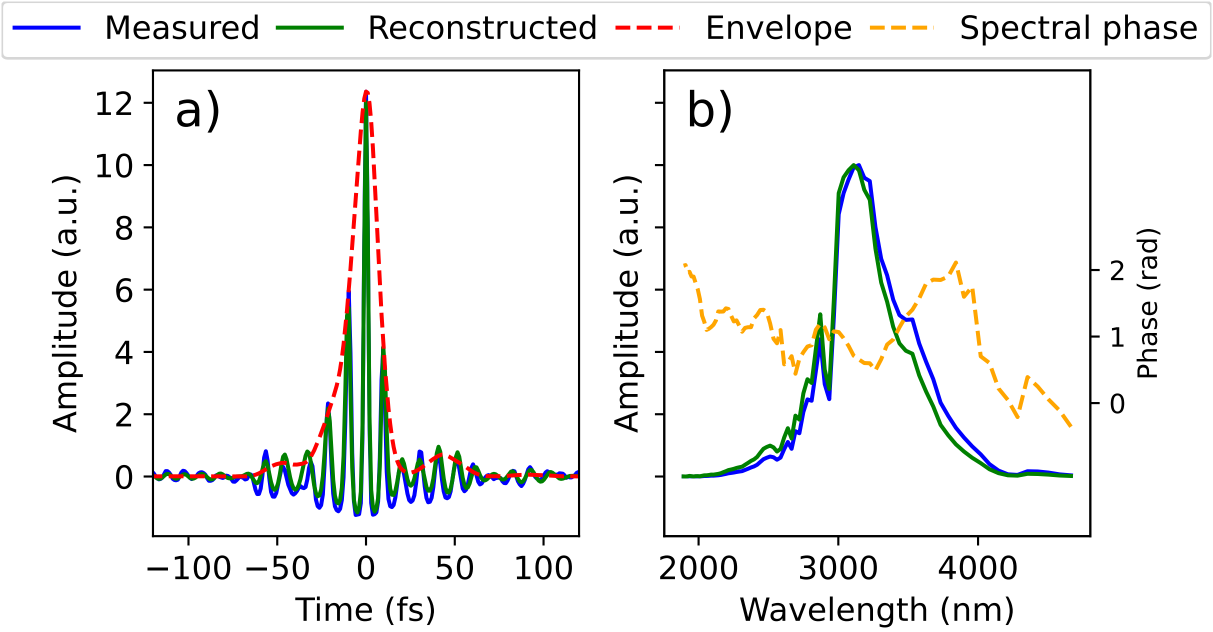

FIGURE 4.9: Results of TIPTOE measurement. (a) Measured and reconstructed electric field and (b) spectral amplitude and spectral phase.

In the TIPTOE device, the incident laser pulse is divided into two spatially separated beamlets using a reflective optic consisting of two concentric mirrors. The outer mirror reflects the main (fundamental) pulse, while the inner mirror reflects a weaker, delayed reference pulse. These two components are subsequently recombined and focused into a common interaction region by a concave mirror. At the focal point, the pulses ionize ambient air through strong-field ionization. The resulting free electrons are accelerated by the local electric field and collected by a pair of electrodes positioned downstream of the interaction region. The detected current signal is sensitive to the instantaneous field strength, enabling the reconstruction of the time-dependent electric field.

To optimize the temporal overlap and achieve the shortest possible pulse duration, dispersion control was implemented using a pair of BK7 glass wedges. By fine-tuning the insertion depth of the wedges, it is possible to introduce variable amounts of group delay dispersion, compensating for residual chirp in the compressed pulse. The resulting ionization signal, modulated by the interference of the fundamental and reference beams, is processed using a proprietary retrieval algorithm provided by the manufacturer of the TIPTOE system.

This algorithm yields a complete temporal characterization of the electric field, including both amplitude and phase (as shown in Figure 4.9 (a)). Furthermore, it allows for the reconstruction of the corresponding optical spectrum and spectral phase (Figure 4.9 (b)), offering detailed insight into the pulse's frequency-domain characteristics. This information is crucial for validating the performance of the post-compression setup and for ensuring that the waveform meets the stringent requirements necessary for subsequent high-field experiments.

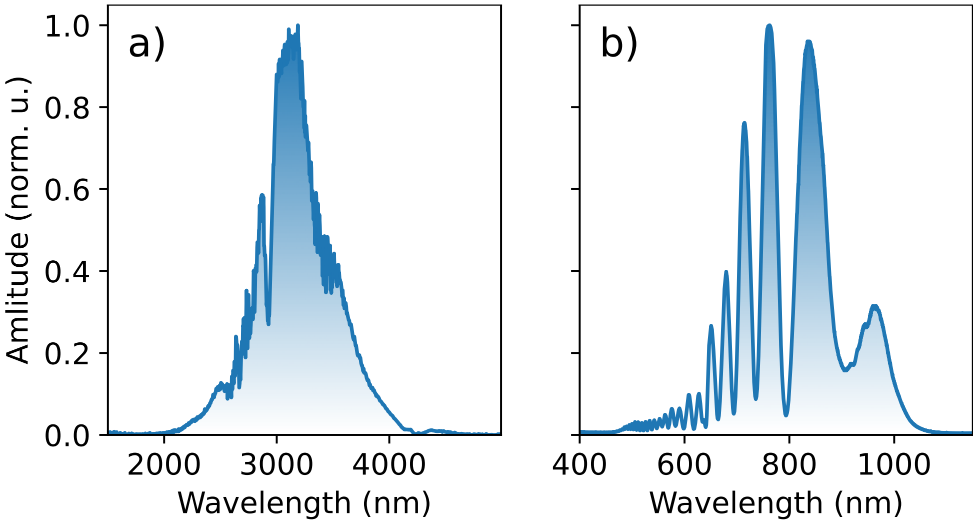

Figure 4.10: Spectrum for MIR (a) and for the generated high order harmonics (b).

After the harmonic generation stage, a 50 mm-long BK7 optical block was inserted to remove the residual MIR driving beam. This filter effectively transmits harmonics in the visible and near-UV range, while strongly attenuating radiation below 350 nm.

Figure 4.10 show the measured spectrum with a commercial fiber-coupled spectrometer (AvaSpec-ULS2048, Avantes), (a) show the spectrum of the IR, this is similar to 4.9 (b), but this recorded before the experimental setup, while 4.10 (b) shows the visible portion of the HHG spectrum spanning from the third to the ninth harmonic.

Each CEP value was sampled across a full 2π scan, using 100 evenly spaced phase steps between $-\pi$ and π. For each CEP setting, 100 single-shot spectra were acquired and averaged to improve the signal-to-noise ratio. Characteristic CEP-dependent features are clearly observed in the harmonic spectra, particularly in the form of modulated intensity patterns across the harmonic orders. It is important to note that the fringe pattern extending into the near-infrared region in Figure 4.11 originates from the interference of HHG emission generated at the front and rear surfaces of the ZnO crystal, a known effect independent of CEP [195]. However, the strong modulation of the harmonic intensity as a function of CEP, especially evident through the appearance of spectral minima, results from constructive and destructive interference of XUV bursts emitted in successive laser half-cycles [196, 204].

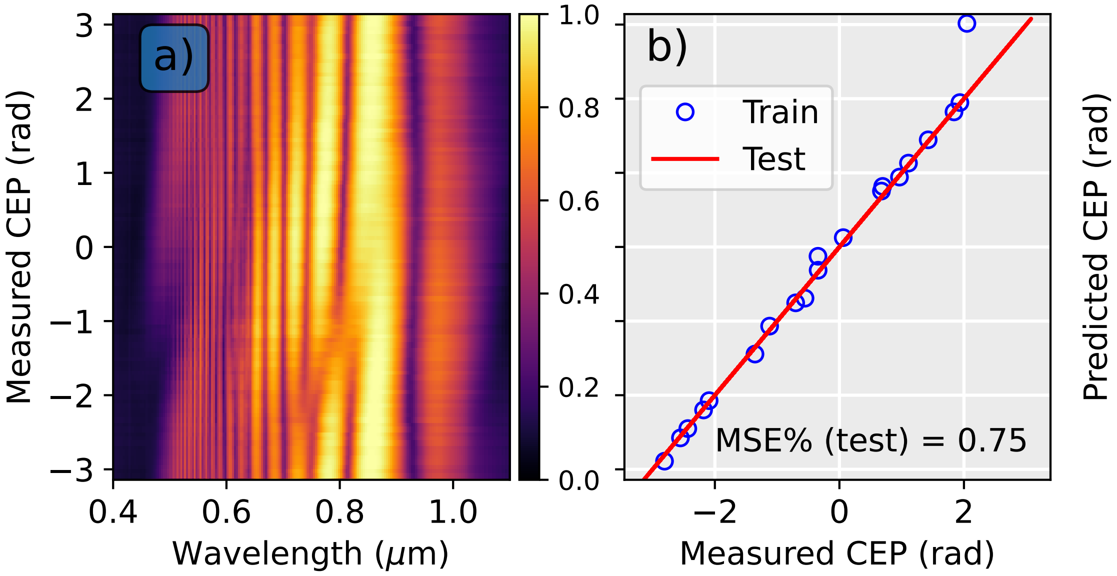

FIGURE 4.11: Measured CEP dependence and the trained ML model. Figure (a) shows the measured high harmonic spectra while scanning the CEP values. The performance of the ExtraTree machine learning algorithm in predicting the measured relative laser CEP using (b) 80% of the data for training (red line) and 20% for testing (open blue circles). The MSE% for this case is 0.75.

A direct comparison between the results of numerical simulations and experimental observations presents several challenges. One of the primary difficulties arises from the fact that CEP is treated in fundamentally different ways in the two approaches. In the case of simulations, the CEP is specified in absolute units, whereas in experimental measurements, only relative values are accessible. In addition, the numerical model, which is based on a one-dimensional (1D) framework, inherently lacks the ability to capture certain key aspects of the experimental setup. Specifically, it cannot replicate the full three-dimensional (3D) symmetry of the actual crystal structure, nor can it account for propagation-related phenomena such as phase matching conditions. These limitations imply that while simulations can offer qualitative insights, they are not expected to reproduce all spectral details observed in experiments. Nevertheless, both theoretical and experimental results exhibit a consistent trend: a clear shift in the position of spectral minima as a function of the CEP is observed. This coherence between datasets underscores the fundamental role of CEP in shaping HHG spectra. It is also well-established that the degree of CEP sensitivity is influenced by ultrafast structural dynamics occurring within the laser-excited lattice. These transient effects are neglected in our simulations, which might contribute to discrepancies between the simulated and measured spectral features. Importantly, the CEP scan performed experimentally demonstrates a one-to-one correspondence between the laser CEP and the generated harmonic spectra. This characteristic is critical, as it ensures the feasibility of employing supervised machine learning techniques to infer the CEP from spectral measurements.

In our analysis, the experimental dataset shown in Fig. 4.11 (b) was divided into two subsets using a random sampling strategy: 80% of the data was allocated for training and the remaining 20% for testing. An ExtraTrees regression model was trained on the spectral input data to predict the corresponding CEP values. The model's accuracy on the training set is illustrated by orange rectangles in the figure, which show a near-perfect match between predicted and actual CEP values. When applied to the previously unseen test data (blue circles), the model continues to perform well, achieving MSE% of 0.75. A noticeable deviation between the predicted and true CEP appears in a region where the training data has a sampling gap, indicated by the discontinuity in that range of the CEP domain. To address this issue, the training dataset was restructured to ensure even sampling of CEP values. In a follow-up experiment shown in Fig.4.12 (a) and Fig.4.12 (b), we redistributed the dataset into equal halves for training and testing, while controlling the sampling to be uniform over the CEP range. This modification resulted in improved predictive performance. Specifically, the evenly sampled dataset yielded an MSE% of 0.61, in contrast to an MSE% of 1.15 obtained from a randomly sampled dataset of equal size. Thus, a factor of approximately two improvements in prediction accuracy was achieved by enforcing uniform sampling during training. These results provide strong evidence that our CEP prediction approach is robust and effective. Moreover, they emphasize the importance of careful dataset construction: achieving high predictive accuracy depends critically on the density and uniformity of CEP values used during the training phase. Such considerations are vital for implementing real-time CEP monitoring in experimental HHG studies using machine learning.

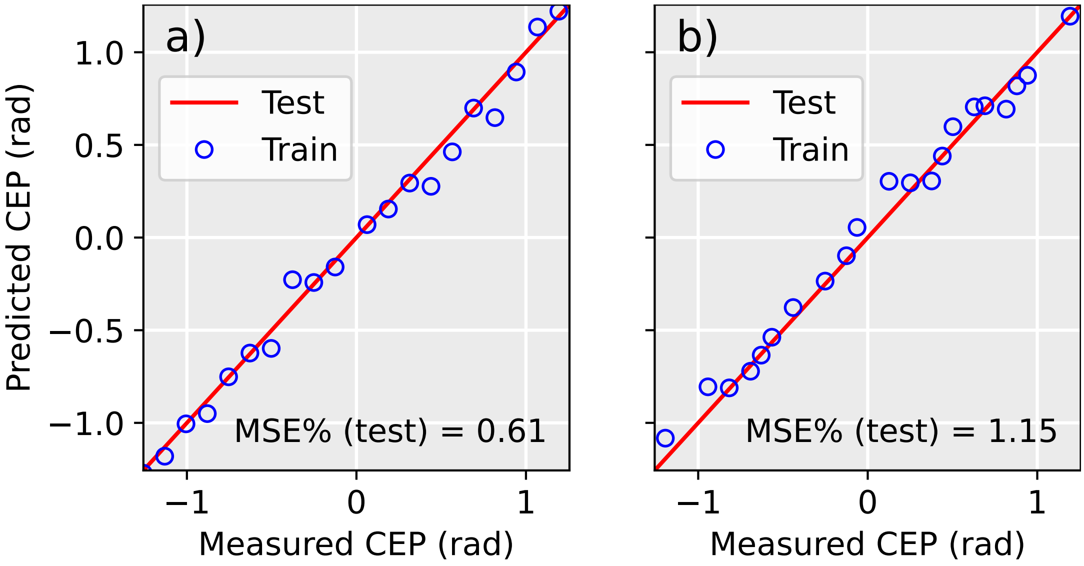

FIGURE 4.12: Measured CEP sampling effect of the trained model. (a) Evenly and (b) randomly sampled datasets were split into 50% training and 50% testing sets. In both scenarios, the slope of the prediction line is nearly 45 degrees, indicating near-perfect estimation performance. MSE% on the test sets are as follows: (a) 0.61%, and (b) 1.15%.

To summarize the findings of this work, we have established and experimentally validated a novel conceptual framework for estimating the carrier-envelope phase of mid-infrared laser pulses using the high-harmonic generation spectrum emitted from a solid-state crystal target. This approach leverages the capability of machine learning (ML) models—specifically, ensemble-based regressors—to recognize intricate spectral features that are uniquely sensitive to variations in the CEP. By exploiting this one-to-one mapping between the CEP and the HHG spectral structure in semiconducting crystals, the model is capable of providing robust, efficient, and cost-effective CEP estimation.

The concept was demonstrated through a combination of theoretical simulations and experimental measurements using a ZnO crystal as the nonlinear medium. The agreement between the simulated and observed trends confirms the viability of this strategy for real-time CEP characterization. Importantly, the methodology requires minimal sampling of the beam—only around 1% of the total pulse energy was used for HHG diagnostics—allowing the rest of the beam to be used in a main experiment. This configuration paves the way for CEP tagging in experiments driven by lasers with randomly varying CEP, offering the possibility of post-sorting experimental data based on the associated CEP. In this study, training of the ML model was performed using reference CEP values obtained by Fringeezz. The underlying framework allows for further generalization: with improved simulation fidelity, it becomes possible to train the model using entirely synthetic data, as previously demonstrated in the context of FROG trace reconstruction [205]. Such an approach could eliminate the need for reference hardware and, in addition, enable direct retrieval of the absolute CEP from the simulations themselves, since the CEP is a known input parameter in the numerical models.

It is worth emphasizing that the present implementation assumes a fixed laser intensity for both training and deployment of the ML model. However, preliminary investigations indicate that the model retains its predictive power across a range of intensities and field configurations, highlighting a certain degree of robustness against experimental fluctuations. Nevertheless, a more comprehensive analysis of the sensitivity of the model to laser intensity variations is ongoing and will be essential for translating this method into a fully generalized, user-independent CEP characterization tool. The broader implications of this work suggest a pathway toward real-time, multi-parameter monitoring and optimization in strong-field physics experiments. Solid-state HHG, particularly in semiconducting media like ZnO, offers a compact and scalable platform where the measurable harmonic spectra are directly shaped by laser properties such as intensity, pulse duration, and CEP. This inherent sensitivity, when coupled with modern ML techniques, enables the development of adaptive diagnostic tools that can support and enhance complex laser-matter interaction experiments. Ultimately, our approach offers a practical and scalable solution for CEP retrieval that significantly reduces the experimental overhead typically associated with spectral phase diagnostics. By requiring fewer measurements and minimizing the complexity of the instrumentation, this method is especially well-suited for high-repetition-rate user facilities such as ELI ALPS, where cost, speed, and accuracy are critical.

4.9 Summary

T4 In order to investigate whether machine learning can be used to predict the carrier-envelope phase of a laser source from high-harmonic generation spectra, I carried out simulations of gas harmonics under conditions matching those of the SYLOS GHHG Long beamline. I then trained a machine learning model using pairs of harmonic spectra and their corresponding CEP values. Finally, I tested the model on spectra it had not seen during training. The predictions reproduced the correct CEP values with only a small error, which confirms the validity of the approach. The demonstrated metrology and conclusion had been shown in [P2] in the context of bulk HHG.

I designed and constructed a dedicated experimental setup. I carried out the complete measurement campaign, which included aligning the beamline, optimizing the HHG process for stable spectral acquisition, and recording a large dataset under controlled experimental conditions. I subsequently performed a detailed analysis of the collected spectra, applying machine learning algorithms to establish the correlation between the spectral features and the CEP of the driving laser pulse. The results demonstrated that this approach is viable, offering the possibility of deploying it as an online diagnostic tool for CEP monitoring. Given its robustness, the method has the potential to be scaled and implemented in larger and more complex HHG beamlines, such as the SYLOS GHHG Long beamline, where real-time CEP tracking could significantly improve experimental stability and reproducibility. This experimental result is presented in [P2].

Summary

Attosecond pulses, produced through high harmonic generation, have become a key tool for exploring atomic and molecular dynamics on their natural timescale [26, 27, 50, 51]. The award of the 2023 Nobel Prize in Physics to Pierre Agostini, Ferenc Krausz, and Anne L'Huillier reflects not only the maturity of this field, but also the importance of their pioneering contributions [206–208]. During the same period, laser technology has advanced at an impressive pace [209]. High–average-power sources with few-cycle pulse durations are now accessible [210], opening the door to new opportunities while also introducing serious challenges. Achieving efficient HHG with such lasers requires more than incremental refinements; it calls for expanded approaches to metrology and diagnostics. In this thesis, I present several attosecond beamlines built around these advanced laser systems, focusing on both on their technical realization and the scientific opportunities they make possible.

Aims

The central aim of this work was to develop and apply characterization techniques for different aspects of HHG. Using multi–tens of millijoule laser drivers, two distinct experimental approaches to achieve optimal phase matching had been carried out. One approach relied on short interaction lengths, such as gas jets, while the other used extended gas cells. As part of a user experiment, The aim was to investigate these two regimes systematically, comparing their performance under realistic conditions. [T1]

With the recent availability of multi–tens of millijoule lasers operating at 1 kHz repetition rate, such as the SYLOS2 system, HHG beamlines can now be driven at conditions that are highly attractive for applications requiring statistical averaging. At the same time, this repetition rate remains compatible with pulsed jet targets, which can serve both as generation media and as end-station targets. A new type of high repetition rate gas valve, promising high gas densities in the multi-kHz range, has recently emerged, though its characterization is not straightforward. The aim was to carry out detailed simulations and experiments to characterize this source with high spatial and temporal resolution, providing insight into its performance and limitations [T2, T3].

When the laser pulse duration approaches fewer than two optical cycles, the carrier-envelope phase becomes a critical parameter for HHG. One of my aims was to develop a method to estimate the CEP directly from measured harmonic spectra using machine learning. Through simulations of gas harmonics driven by the SYLOS laser, this technique feasibility can be evaluated under experimental conditions.

Solid state targets offer the possibility of probing material properties while generating broadband harmonic radiation from the infrared into the ultraviolet. At ELI ALPS, the MIR laser delivers pulses of only 1.5 optical cycles, which, when combined with a suitable crystal, allow strong CEP sensitivity to emerge. My goal was to measure this CEP dependence and to investigate whether machine learning methods could again be applied for CEP estimation, drawing a parallel to the gas-phase case [T4].

Results

T1 Part of the results presented in this thesis point were obtained during a user experiment with a research group from Lund University, investigating the dependence of high-order harmonic generation on medium length and gas pressure. For this experiment, I prepared the beamline and ensured that all subsystems were operating under optimal conditions. I characterized both the temporal and spatial properties of the driving infrared pulse and measured the characteristics of the generated XUV radiation. I optimized the generation conditions for the selected gas targets by adjusting the alignment, focusing geometry, and gas pressure. I also assembled, installed, and configured the gas cells, making sure they were suitable for the required medium lengths and buffer gas conditions. As part of the preparation, I performed preliminary measurements to verify the stability and performance of the setup. During the experimental campaign, I actively assisted the users with their measurements and supported them in analyzing and interpreting the recorded data.

The results confirm that there is an equivalence in terms of HHG yield between a short high pressure and a long low pressure medium. This predicted hyperbolic behavior of the medium length-pressure dependence had been confirmed. The model is not too sensitive to the laser intensity, which also confirmed by the measurements, since without it, it would have been difficult to tackle the issue with the energy loss due to the coupling of the laser beam into the cell between the different experimental cells. The difference between the XUV beamprofile in different medium length was also confirmed.

These findings are important during the designing phase of a new HHG beamline. When the XUV beam profile is not important as the high flux of photons, short high pressure jets has the advantage. Also, these are easier to implement compared to the generation in gas cell to loose focusing condition, and it can be the better choice when the laser energy is lower. The advantage of using long gas cells is that the XUV beam quality is better, and it is less sensitive to the pressure changes in the gas jets, and it is easier to implement a stable generation medium. This result had been published at [P3].

T2 I performed a complete spatial and temporal characterization of cantilever piezo gas valves, which are used for high-harmonic generation and spectroscopy experiments in both the SYLOS GHHG Long and SYLOS GHHG Compact beamlines. To accomplish this, I designed and built a stand-alone gas characterization end station that allowed precise measurements independent of the main beamline operation. I simulated interferometric fringe patterns corresponding to the expected gas density distributions and developed a dedicated data analysis code to retrieve accurate atomic number density profiles in the interaction region. I validated this approach against experimental data and demonstrated its reliability across a wide range of operating conditions. In addition, I designed the system to be flexible and adaptable to different gas delivery configurations, such as slit nozzles or multiple gas jets arranged in series, thereby extending its usefulness for future experimental setups and user needs. The results of this work were published in [P1].

T3 I conducted a series of measurements with high-harmonic generation to record the HHG yield fluctuation caused by gas density changes. For the HHG, I performed simulations using the gas density results recorded with the stand-alone gas characterization end station. The simulated results showed excellent agreement with the measured data, thereby confirming the accuracy and reliability of the density retrieval method. In parallel, I investigated light emitted by the generated plasma as a diagnostic tool to monitor potential variations in gas pressure during extended operation. This approach provided a practical, real-time monitoring tool, enabling the detection of gradual drifts or fluctuations in the gas delivery system without interrupting the experiment. These experimental result is presented in [P1].

T4 To investigate whether machine learning can be used to predict the carrier-envelope phase of a laser source from high-harmonic generation spectra, I carried out simulations of gas HHG, under conditions matching those of the SYLOS GHHG Long beamline. I trained a machine learning model using pairs of harmonic spectra and their corresponding CEP values. Finally, I tested the model on spectra it had not seen during training. The predictions reproduced the correct CEP values with only a small error, which confirms the validity of the approach.

I designed and constructed a dedicated experimental setup and I carried out the complete measurement campaign, which included aligning the beamline, optimizing the

HHG process for stable spectral acquisition, and recording a large dataset under controlled experimental conditions. I subsequently performed a detailed analysis of the collected spectra, applying machine learning algorithms to establish the correlation between the spectral features and the CEP of the driving laser pulse. The results demonstrated that this approach is viable, offering the possibility of deploying it as an online diagnostic tool for CEP monitoring. Given its robustness, the method has the potential to be scaled and implemented in larger and more complex HHG beamlines, such as the SYLOS GHHG Long beamline, where real-time CEP tracking could significantly improve experimental stability and reproducibility. This experimental result is presented in [P2].

Magyar nyelvű összefoglaló

A lézer feltalálásával [1] lehetővé vált rövid, koherens fényimpulzusok előállítása, lehetőséget adva az anyagok időben tranziens folyamatainak vizsgálatára. A fényimpulzushosszak folyamatos rövidítésére való törekvés a lézertechnológia fejlődését motiválta [2], hiszen hogy minél rövidebb a fényimpulzus, annál részletesebben és lokalizáltabban tárhatók fel a dinamikai folyamatok [3, 4]. Ez a kutatási irány nemcsak az ultragyors jelenségek mélyebb megértését eredményezte, hanem új lendületet adott az alkalmazott kutatásoknak [5], és innovációkat indított el olyan ipari területeken, ahol a pontos időzítés és a gyors vezérlés kulcsfontosságú [6].

A közeg által biztosított véges spektrális sávszélesség, valamint a spektrális fázis kezekésének kihívásai alapvető korlátokat szabtak arra, hogy milyen rövid impulzusokat lehet közvetlenül előállítani hagyományos lézererősítő közegekből. Fejlett rendszerekkel – például Ti:zafír lézerekkel és optikai paraméteres erősítőkkel – tipikusan 5–6 fs körüli minimális impulzushossz érhető el [8, 9]. Néhány optikai ciklusos tartomány eléréséhez a közeli infravörös régióban (közel 2 fs) már utókompressziós technikákra van szükség, amelyekhez a szükséges spektrális kiszélesítést nemlineáris optikai közegben valósítják meg [10–13], majd ezt a fényimpulzus időbeli kompresszálása követi, amely csörpölt tükrökkel és akuszto-optikai modulátorokkal diszperziókompenzáción keresztül történik. A legújabb fejlesztések közé tartoznak a többutas cellák [17, 18], valamint a kristályokon vagy üveglemezen alapuló kompressziós sémák [19, 20].

A femtoszekundumosnál rövidebb fényimpulzusok keltéséhez szükséges sávszélesség miatt rövidebb hullámhossz-tartományba kell átlépni, ahol már nem áll rendelkezésre erősítő közeg, valamint posztkomresszálásnál az intenzitás növelésével a spektrális kiszelesedés telítődik, határt szabva az így elérhető legszélesebb spektrumnak.

Femtoszekundumnál rövidebb impulzushossz elérésének érdekében több megközelítés került javaslatra és megvalósításra, ezek közül a magasrendű harmonikus keltés (HHG) bizonyult az egyik legérettebb és kísérletileg leginkább hozzáférhető megközelítésnek [21, 22]. Más irányok – például az ultranagy sávszélességű fény szintézise koherens fázisvezérléssel [23], vagy a plazma wakefield gyorsítókkal hajtott szabad-elektron lézerek (FEL-ek) [24] – szintén ígéretesek, de jellemzően nagyméretű infrastruktúrát és bonyolult kísérleti elrendezéseket igényelnek [25]. Ezzel szemben a HHG labor környezetben is megvalósítható, femto- illetve attoszekundumos impulzusok előállítását teszi lehetővé magas tér- és időbeli koherenciával [26–28].

A HHG egy nemlineáris folyamat, amely során intenzív lézermezőben lévő atomok vagy molekulák a fundamentális lézer frekvencia többszöröseit sugározzák ki páros vagy páratlan felharmónikusok formájában, a közeg szimmetriatulajdonságaitól [29] vagy az elektromos tér tulajdonságaitól [30, 31] függően. A spektrum kiterjedhet az extrém ultraibolya (XUV) tartománytól egészen a lágy röntgenig [32–34]. A korai 2000-es években történt áttörések megmutatták, hogy a HHG felhasználható izolált attoszekundumos impulzusok [27] vagy impulzussorozatok [26] előállítására, megalapozva ezzel az attoszekundumos tudományt, lehetővé téve az elektronok mozgásának vizsgálatát atomokban és molekulákban.

A HHG első kísérleti megfigyelése 1987-ben történt két független kutatócsoport által Chicagóban [35] és a CEA Saclay-ban [36]. A korai kísérletek ritka nemesgázokkal – argonnal, kriptonttal és xenonnal – zajlottak, amelyeket az akkori legfejlettebb lézerek hajtottak: Nd:YAG rendszerek 1064 nm-en [36], KrF excimer lézerek 248 nm-en [37, 38], valamint Ti:zafír lézerek 800 nm-en [38–40]. Az 1990-es évektől kezdve a magasharmonikusokkal kapcsolatos kutatás kiterjedt molekuláris célpontokra is [41–43], feltárva a molekuláris pályák és a nukleáris mozgások szerepét az erős mező dinamikájában. Az attoszekundumos impulzusok egyedülálló képessége, hogy valós időben követhető az elektronikus, vibrációs és szerkezeti dinamika.

Ezt jelentős mérföldkövek követték, például a HHG demonstrációja plazmafelületekről ultra-magas intenzitásokon [44–46], illetve a magas harmonikusok előállítása kristályokból 2010-ben [48, 49, 211]. Ez az áttörés új fejezetet nyitott, és rávilágított a kondenzált anyag rendszerek potenciáljára kompakt, hatékony attoszekundumos fényforrásként. A gázokhoz képest a szilárdtestek nagyobb anyagsűrűséget és jobb integrációs lehetőségeket kínálnak a fotonikai technológiákkal, azonban ezen források viselkedése összetettebb tulajdonságokat hordoznak, például interband átmeneteket és sávstruktúra-hatásokat.

A HHG-val létrehozott attoszekundomos impulzusok mára egyszerre erőteljes fényforrásá és precíziós diagnosztikai eszközzé váltak, lehetővé téve az alkalmazásukat az ultragyors spektroszkópiától [26, 27, 50, 51] a koherens diffraktív képalkotáson [52, 53], a relativisztikus plazmaoptikán [54–56] át egészen az időfelbontott elektron-dinamikáig. Pierre Agostini, Krausz Ferenc és Anne L'Huillier 2023-as Fizikai Nobel-díjjal való kitüntetése nemcsak a terület érettségét bizonyítja, hanem úttörő munkájuk kiemelkedő jelentőségét is [206–208]. Ezzel párhuzamosan a lézertechnológia is lenyűgöző ütemben fejlődött [209]: mára már elérhetők nagy átlagteljesítményű, néhányciklusos impulzusokat előállító források [210], amelyek új lehetőségeket nyitnak meg, ugyanakkor új kihívásokat is teremtenek, hatékony HHG elérése nem egyszerű feladat, átfogó újításokat igényel a metrológia és a diagnosztika területén is.

Célok

Ezen dolgozatban számos olyan attoszekundumos nyalábvonalat mutatok be, amelyek korszerű lézerrendszerekre épülnek. Munkám központi célja a HHG különböző aspektusainak karakterizálási módszereinek fejlesztése és alkalmazása volt. Nagy csúcsteljesítményű lézerrel, az optimális fázisillesztés elérése érdekében, eltérő kísérleti megközelítéseket vizsgáltam. Az egyik megoldásnál a magas harmonikus keltés rövid közegben, például gáz jet-ben történt, míg a másik megoldásnál hosszú gázcella lett alkalmazva. Egy felhasználói kísérlet keretében ezen két kondíciót vizsgáltam szisztematikusan, összehasonlítva a numerikus modell által megjósolt következtetéseket valós kísérleti körülmények között. [T1]

Az utóbbi időben elérhetővé váltak a több tíz millijoule energiájú, 1 kHz ismétlési frekvencián üzemelő lézerek, például a SYLOS2 lézer. Ezen források olyan körülményeket teremtenek HHG-hez, amelyek már lehetővé teszik a statisztikai átlagolást igénylő alkalmazásokat is. Ezen ismétlési frekvencián pulzáló gázforrások még alkalmazhatóak, így szolgálhatnak generáló közegként vagy céltárgyként is. Egy új típusú, piezo lap mozgatásán alapuló, nagy ismétlési frekvencián működő gázszelep vált elérhetővé, amely a több kilohertzes tartományban is nagy gázsűrűséget ígér, de karakterizálása nem triviális feladat. Célom szimulációkon és kísérleteken keresztül ezen forrás tér- és időbeli felbontású vizsgálata volt, amelyek új betekintést adtak, hogyan viselkedik a vákuumba jutatott gáz sugár, vagy gáz jet [T2, T3].

Az impulzushossz két optikai ciklus alá csökkenésével, a vivőburkoló fázis (CEP) kulcsfontosságú paraméterré válik HHG szempontjából. Egyik célom az volt, hogy olyan módszert fejlesszek ki, amely a mért felharmonikus spektrumokból képes közvetlenül meghatározni a CEP értékét gépi tanulás segítségével. A koncepciót szimulációkon keresztül a SYLOS lézer által hajtott gázfelharmonikusokon teszteltem.

Végül ezt az elképzelést kiterjesztettem a szilárdtest HHG-re is. A szilárd céltárgyak lehetőséget kínálnak anyagtulajdonságok vizsgálatára, miközben szélessávú felharmonikus sugárzást bocsátanak ki az infravöröstől az ultraibolya tartományig. Az ELI ALPS MIR lézere 1,5 optikai ciklus hosszúságú impulzusokat biztosít, amelyekkel a megfelelő kristályban keltett harmonikusok erős CEP-érzékenységet mutatnak. A célom az volt, hogy megmérjem ezt a CEP-függést, és megvizsgáljam, vajon a gépi tanulási módszerek alkalmazhatók-e itt is a CEP becslésére, hasonlóan a gázfázisú esethez [T4].

Eredmények

T1 Egy felhasználói kísérlet során, Lundi egyetem kutatóival együttműködve, a magasrendű felharmonikus generálás közeghosszúság- és nyomásfüggését vizsgáltuk. Ennek keretében előkészítettem a nyalábvonalat, és gondoskodtam arról, hogy minden alrendszer optimális körülmények között működjön. Karakterizáltam a generálást végző infravörös impulzus időbeli és térbeli tulajdonságait, valamint megmértem a keletkező extrém ultraibolya (XUV) sugárzás jellemzőit. A választott gázcélpontokra optimalizáltam a generálási körülményeket a fázisillesztés szempontjából, a fókuszgeometria és a gáznyomás beállításával. Részt vettem a kísérlet során használt gáz cellák tervezésében, valamint teszteltem ezeket kísérleti körülmények között. Az előkészületek részeként előzetes méréseket is végeztem, hogy ellenőrizzem a rendszer stabilitását és teljesítményét. A kísérleti kampány alatt segítettem a felhasználókat a mérésekben, valamint támogattam őket az adatok kiértékelésében és értelmezésében.

Az eredmények megerősítették, hogy a HHG hozama szempontjából egy rövid, nagy nyomású közeg, valamint egy hosszú, alacsony nyomású közeg ekvivalens. Ez a közeghossz–nyomás összefüggés várható hiperbolikus viselkedése tehát igazolást nyert. A modell nem túl érzékeny a lézer intenzitására, amit a mérések is alátámasztottak. Ez különösen fontos, hiszen ennek hiányában a lézernyaláb cellába történő csatolásából adódó energiaveszteséget a különbőző cellák között nem lehetett volna kompenzálni. Megerősítést nyert az XUV-nyaláb profiljának különbsége is a különböző közeghosszúságok esetén.

Ezek a eredmények fontosak lehetnek új HHG-nyalábvonalak tervezésekor. Ha a kimenő XUV-nyaláb profiljának minősége kevésbé fontos, mint a nagy fotonfluxus, akkor a rövid, nagy nyomású gázsugarak előnyt jelenthetnek. Ennek megvalósítása egyszerűbb, mint a gázcellás generálás, amely általában hosszabb fókuszálást igényel. Rövid közeg használata az alacsonyabb rendelkezésre álló lézerenergiáknál is jobb választás lehet. A hosszú gázcellák előnye ezzel szemben a jobb nyalábminőség, a kisebb érzékenység a nyomásingadozásokra, valamint az, hogy stabilabb generáló közeget és így XUV forrást lehet velük kialakítani. Ezen eredmények a [P3]-as publikációban kerületek bemutatásra.

T2 Teljeskörű karakterizálást végeztem a pulzáló piezo gázszelepeken térben és időben felbontva. Ezen gázforrások a SYLOS GHHG Long és a SYLOS GHHG Compact nyalábvonalakon is alkalmazva vannak magasrendű felharmonikus keltési és spektroszkópiai kísérletekben. Az interferometrikus méréshez egy önálló gázkarakterizáló végállomást terveztem és építettem, amely lehetővé tette pontos részecskeszám mérését. Interferenciaképeket szimuláltam le a várható gázsűrűség-eloszlásokhoz, és olyan adatelemző kódot fejlesztettem ki, amely pontos atomsűrűség-profilokat tudott visszanyerni. Az eljárást kísérleti adatokkal hasonlítottam össze, és megbizonyosodtam róla, hogy az eljárás széles körű működési feltételek mellett is alkalmazható. A rendszert úgy terveztem, hogy rugalmas legyen különböző geometriájú fúvókákhoz, például résfúvókákhoz vagy sorban elhelyezett több gázsugárhoz is, ezzel kiterjesztve jövőbeli kísérletek és felhasználói igények számára. Ezen eredmény a [P1]-es publikációban található.

T3 A gázsugár részecskeszámának térbeli és időbeli eloszlását ellenőriztem magasharmonikus keltéssel. A kísérlethez kötődő HHG szimulációkat futattam le felhasználva az interferometrikus technikával szerzett eredményeket. A szimulációk kiváló egyezést mutattak a mért adatokkal, ezáltal megerősítve a sűrűség meghatározási módszer pontosságát és megbízhatóságát. Ezzel párhuzamosan a keltett plazma fényerejét is vizsgáltam, mint diagnosztikai eszközt a gáznyomás esetleges változásainak monitorozására hosszan tartó működés közben. Ez a megközelítés praktikus, valós idejű monitorozási lehetőséget adott, amely lehetővé teszi a lassú és gyors gázeloszlás változások detektálását a kísérlet megszakítása nélkül. A mért eredmények összevetése a [P1]-es pubikációban került bemutatásra.

T4 Annak vizsgálatára, hogy a gépi tanulással magasrendű felharmonikus spektrumokból a lézerforrás vivőburkoló fázisa meghatározható-e, szimulációkat végeztem gázfelharmonikusokra a SYLOS GHHG Long nyalábvonal kísérleti feltételeinek megfelelő körülmények között. Ezután egy gépi tanulási modellt tanítottam be felharmonikus spektrum–CEP párok segítségével. Végül olyan spektrumokon teszteltem a modellt, amelyeket még nem látott a model a tanítás során. Az előrejelzések kis hibával reprodukálták a helyes CEP-értékeket, amely megerősítette a módszer érvényességét. A dolgozat írásakor ilyen kísérletek az ELI ALPS-ban gázfázisú HHG esetében még nem végezhetők el.

A szimulációkon keresztül bemutatatott eredményeket ezután szilárdtest magas harmonikusokon keresztül **validáltam**. Egy dedikált kísérleti berendezést terveztem és építettem, majd végrehajtottam a méréseket. Ez magában foglalta a nyalábvonal beállítását és a HHG optimalizálását a stabil spektrális adatgyűjtés érdekében. A mért spektrumokat részletesen elemeztem, és gépi tanulási algoritmusokat alkalmaztam a mért spektrumok és a lézer CEP közötti összefüggés feltárására. Az eredmények igazolták a módszer alkalmazhatóságát, és rámutattak arra, hogy ez online diagnosztikai eszközként is használható a CEP monitorozására. Robusztusságának köszönhetően a módszer alkalmazható nagyobb és összetettebb HHG-nyalábvonalakban is, például a SYLOS GHHG Long rendszeren, ahol a valós idejű CEP-követés hozzájárulhat a kísérletek stabilitásához és reprodukálhatóságához. Az eredmények a [P2]-es cikkben kerültek publikálásra.

Bibliography

[1] A. L. Schawlow and C. H. Townes, “Infrared and optical masers,” *Physical Review*, vol. 112, no. 6, pp. 1940–1949, 1958.

[2] P. M. W. French, “The generation of ultrashort laser pulses,” *Reports on Progress in Physics*, vol. 58, no. 2, pp. 169–262, 1995.

[3] A. H. Zewail, “Femtochemistry: atomic-scale dynamics of the chemical bond,” *The Journal of Physical Chemistry A*, vol. 104, no. 24, pp. 5660–5694, 2000.

[4] F. Krausz and M. Ivanov, “Attosecond physics,” *Reviews of Modern Physics*, vol. 81, no. 1, pp. 163–234, 2009.

[5] P. B. Corkum and F. Krausz, “Attosecond science,” *Nature Physics*, vol. 3, no. 6, pp. 381–387, 2007.

[6] T. Udem, R. Holzwarth, and T. W. Hänsch, “Optical frequency metrology,” *Nature*, vol. 416, no. 6877, pp. 233–237, 2002.

[7] G. Mourou and T. Tajima, “More intense, shorter pulses,” *Science*, vol. 331, no. 6013, pp. 41–42, 2011.

[8] A. Apolonski et al., “Controlling the phase evolution of few-cycle light pulses,” *Physical Review Letters*, vol. 85, no. 4, pp. 740–743, 2000.

[9] R. Ell et al., “Generation of 5-fs pulses and octave-spanning spectra directly from a ti:sapphire laser,” *Optics Letters*, vol. 26, no. 6, p. 373, 2001.

[10] W. H. Knox, R. L. Fork, M. C. Downer, R. H. Stolen, C. V. Shank, and J. A. Valdmanis, “Optical pulse compression to 8 fs at a 5-khz repetition rate,” *Applied Physics Letters*, vol. 46, no. 12, pp. 1120–1121, 1985.

[11] M. Nisoli, S. De Silvestri, and O. Svelto, “Generation of high energy 10 fs pulses by a new pulse compression technique,” *Applied Physics Letters*, vol. 68, no. 20, pp. 2793–2795, 1996.

[12] M. Nisoli et al., “Compression of high-energy laser pulses below 5 fs,” *Optics Letters*, vol. 22, no. 8, p. 522, 1997.

[13] A. Baltuška, Z. Wei, M. S. Pshenichnikov, and D. A. Wiersma, “Optical pulse compression to 5 fs at a 1-mhz repetition rate,” *Optics Letters*, vol. 22, no. 2, p. 102, 1997.

[14] R. Szipöcs, C. Spielmann, F. Krausz, and K. Ferencz, “Chirped multilayer coatings for broadband dispersion control in femtosecond lasers,” *Optics Letters*, vol. 19, no. 3, p. 201, 1994.

[15] R. Szipőcs and A. Kőházi-Kis, “Theory and design of chirped dielectric laser mirrors,” *Applied Physics B: Lasers and Optics*, vol. 65, no. 2, pp. 115–135, 1997.

[16] F. Verluise, V. Laude, Z. Cheng, C. Spielmann, and P. Tournois, “Amplitude and phase control of ultrashort pulses by use of an acousto-optic programmable dispersive filter: pulse compression and shaping,” *Optics Letters*, vol. 25, no. 8, p. 575, 2000.

[17] J. Schulte, T. Sartorius, J. Weitenberg, A. Vernaleken, and P. Russbueldt, “Nonlinear pulse compression in a multi-pass cell,” *Optics Letters*, vol. 41, no. 19, p. 4511, 2016.

[18] A.-L. Viotti et al., “Multi-pass cells for post-compression of ultrashort laser pulses,” *Optica*, vol. 9, no. 2, p. 197, 2022.

[19] C. Rolland and P. B. Corkum, “Compression of high-power optical pulses,” *Journal of the Optical Society of America B*, vol. 5, no. 3, p. 641, 1988.

[20] S. Tóth et al., “Single thin-plate compression of multi-tw laser pulses to 3.9 fs,” *Optics Letters*, vol. 48, no. 1, p. 57, 2022.

[21] G. Farkas and C. Tóth, “Proposal for attosecond light pulse generation using laser induced multiple-harmonic conversion processes in rare gases,” *Physics Letters A*, vol. 168, no. 5–6, pp. 447–450, 1992.

[22] P. B. Corkum, N. H. Burnett, and M. Y. Ivanov, “Subfemtosecond pulses,” *Optics Letters*, vol. 19, no. 22, p. 1870, 1994.

[23] H. Alqattan, D. Hui, V. Pervak, and M. T. Hassan, “Attosecond light field synthesis,” *APL Photonics*, vol. 7, no. 4, 2022.

[24] W. Wang et al., “Free-electron lasing at 27 nanometres based on a laser wakefield accelerator,” *Nature*, vol. 595, no. 7868, pp. 516–520, 2021.

[25] P. K. Maroju et al., “Complex attosecond waveform synthesis at fel fermi,” *Applied Sciences*, vol. 11, no. 21, p. 9791, 2021.

[26] P. M. Paul et al., “Observation of a train of attosecond pulses from high harmonic generation,” *Science*, vol. 292, no. 5522, pp. 1689–1692, 2001.

[27] M. Hentschel et al., “Attosecond metrology,” *Nature*, vol. 414, no. 6863, pp. 509–513, 2001.

[28] H. Alqattan, D. Hui, V. Pervak, and M. T. Hassan, “Attosecond light field synthesis,” *APL Photonics*, vol. 7, no. 4, p. 041 301, 2022.

[29] J. Chen, S. Yu, Y. Li, S. Wang, and Y. Chen, “Odd–even harmonic emission from asymmetric molecules: Identifying the mechanism *,” *Chinese Physics B*, vol. 26, no. 9, p. 094 209, 2017.

[30] X. He et al., “Interference effects in two-color high-order harmonic generation,” *Physical Review A*, vol. 82, no. 3, p. 033 410, 2010.

[31] R. A. Ganeev et al., “Enhancement of high-order harmonic generation using a two-color pump in plasma plumes,” *Physical Review A*, vol. 80, no. 3, p. 033 845, 2009.

[32] Z. Chang, A. Rundquist, H. Wang, M. M. Murnane, and H. C. Kapteyn, “Generation of coherent soft x rays at 2.7 nm using high harmonics,” *Physical Review Letters*, vol. 79, no. 16, pp. 2967–2970, 1997.

[33] P. Tenio, C. Ming-Chang, A. Paul, M. M. M, and K. H. C, “The attosecond nonlinear optics of bright coherent x-ray generation,” *Nature Photonics*, vol. 4, no. 12, pp. 822–832, 1, 2010.

[34] T. Popmintchev et al., “Bright coherent ultrahigh harmonics in the kev x-ray regime from mid-infrared femtosecond lasers,” *Science*, vol. 336, no. 6086, pp. 1287–1291, 2012.

[35] A. McPherson et al., “Studies of multiphoton production of vacuum-ultraviolet radiation in the rare gases,” *Journal of the Optical Society of America B*, vol. 4, no. 4, p. 595, 1987.

[36] M. Ferray, A. L’Huillier, X. F. Li, L. A. Lompre, G. Mainfray, and C. Manus, “Multiple-harmonic conversion of 1064 nm radiation in rare gases,” *J. Phys. B At. Mol. Opt. Phys.*, vol. 21, no. 3, 1988.

[37] N. Sarukura, K. Hata, T. Adachi, R. Nodomi, M. Watanabe, and S. Watanabe, “Coherent soft-x-ray generation by the harmonics of an ultrahigh-power krf laser,” *Physical Review A*, vol. 43, no. 3, pp. 1669–1672, 1991.

[38] K. Kondo, N. Sarukura, K. Sajiki, and S. Watanabe, “High-order harmonic generation by ultrashort krf and ti:sapphire lasers,” *Physical Review A*, vol. 47, no. 4, R2480–r2483, 1993.

[39] J. J. Macklin, J. D. Kmetec, and C. L. Gordon, “High-order harmonic generation using intense femtosecond pulses,” *Physical Review Letters*, vol. 70, no. 6, pp. 766–769, 1993.

[40] D. von der Linde et al., “Generation of high-order harmonics from solid surfaces by intense femtosecond laser pulses,” *Physical Review A*, vol. 52, no. 1, R25–r27, 1995.

[41] M. Lein, N. Hay, R. Velotta, J. P. Marangos, and P. L. Knight, “Role of the intramolecular phase in high-harmonic generation,” *Physical Review Letters*, vol. 88, no. 18, p. 183 903, 2002.

[42] J. Itatani et al., “Tomographic imaging of molecular orbitals,” *Nature*, vol. 432, no. 7019, pp. 867–871, 2004.

[43] N. L. Wagner et al., “Monitoring molecular dynamics using coherent electrons from high harmonic generation,” *Proceedings of the National Academy of Sciences*, vol. 103, no. 36, pp. 13 279–13 285, 2006.

[44] R. Lichters, J. Meyer-ter-Vehn, and A. Pukhov, “Short-pulse laser harmonics from oscillating plasma surfaces driven at relativistic intensity,” *Physics of Plasmas*, vol. 3, no. 9, pp. 3425–3437, 1996.

[45] S. Gordienko, A. Pukhov, O. Shorokhov, and T. Baeva, “Relativistic doppler effect: Universal spectra and zeptosecond pulses,” *Physical Review Letters*, vol. 93, no. 11, p. 115 002, 2004.

[46] B. Dromey et al., “High harmonic generation in the relativistic limit,” *Nature Physics*, vol. 2, no. 7, pp. 456–459, 2006.

[47] S. Ghimire, A. D. DiChiara, E. Sistrunk, P. Agostini, L. F. DiMauro, and D. A. Reis, “Observation of high-order harmonic generation in a bulk crystal,” *Nature Physics*, vol. 7, no. 2, pp. 138–141, 2010.

[48] G. Vampa et al., “All-optical reconstruction of crystal band structure,” *Physical Review Letters*, vol. 115, no. 19, 2015.

[49] G. Ndabashimiye et al., “Solid-state harmonics beyond the atomic limit,” *Nature*, vol. 534, no. 7608, pp. 520–523, 2016.

[50] E. Goulielmakis et al., “Real-time observation of valence electron motion,” *Nature*, vol. 466, no. 7307, pp. 739–743, 2010.

[51] M. Holler, F. Schapper, L. Gallmann, and U. Keller, “Attosecond electron wavepacket interference observed by transient absorption,” *Physical Review Letters*, vol. 106, p. 123 601, 2011.

[52] J. Huijts et al., “Broadband coherent diffractive imaging,” *Nature Photonics*, vol. 14, no. 10, pp. 618–622, 2020.

[53] D. F. Gardner et al., “Subwavelength coherent imaging of periodic samples using a 13.5 nm tabletop high-harmonic light source,” *Nature Photonics*, vol. 11, no. 4, pp. 259–263, 2017.

[54] H. Vincenti, S. Monchocé, S. Kahaly, G. Bonnaud, P. Martin, and F. Quéré, "Optical properties of relativistic plasma mirrors," *Nature Communications*, vol. 5, no. 1, 2014.

[55] A. Leblanc, S. Monchocé, C. Bourassin-Bouchet, S. Kahaly, and F. Quéré, "Ptychographic measurements of ultrahigh-intensity laser–plasma interactions," *Nature Physics*, vol. 12, no. 4, pp. 301–305, 2015.

[56] A. Leblanc, S. Monchocé, H. Vincenti, S. Kahaly, J.-L. Vay, and F. Quéré, "Spatial properties of high-order harmonic beams from plasma mirrors: A ptychographic study," *Physical Review Letters*, vol. 119, no. 15, 2017.

[57] F. Brunel, "Harmonic generation due to plasma effects in a gas undergoing multiphoton ionization in the high-intensity limit," *Journal of the Optical Society of America B*, vol. 7, no. 4, p. 521, 1990.

[58] J. Gao, F. Shen, and J. G. Eden, "Quantum electrodynamic treatment of harmonic generation in intense optical fields," *Physical Review Letters*, vol. 81, no. 9, pp. 1833–1836, 1998.

[59] P. B. Corkum, "Plasma perspective on strong field multiphoton ionization," *Physical Review Letters*, vol. 71, no. 13, pp. 1994–1997, 1993.

[60] J. L. Krause, K. J. Schafer, and K. C. Kulander, "High-order harmonic generation from atoms and ions in the high intensity regime," *Phys. Rev. Lett.*, vol. 68, no. 24, pp. 3535–3538, 1992.

[61] M. Labeye et al., "Optimal basis set for electron dynamics in strong laser fields: The case of molecular ion h2+," *Journal of Chemical Theory and Computation*, vol. 14, no. 11, pp. 5846–5858, 2018.

[62] J. Aygun, C. G. Buitrago, M. F. Ciappina, and A. L. Harris, "Spectral phase pulse shaping reduces ground state depletion in high-order harmonic generation," *The European Physical Journal D*, vol. 78, no. 8, 2024.

[63] M. Marchetta, C. Morassut, J. Toulouse, E. Coccia, and E. Luppi, "Time-dependent ab initio molecular-orbital decomposition for high-harmonic generation spectroscopy," *The Journal of Chemical Physics*, vol. 161, no. 20, 2024.

[64] M. Lewenstein, P. Balcou, M. Ivanov, A. L'Huillier, and P. B. Corkum, "Theory of high-harmonic generation by low-frequency laser fields," *Phys. Rev. A*, vol. 49, no. 3, pp. 2117–2132, 1994.

[65] A. Nayak et al., "Saddle point approaches in strong field physics and generation of attosecond pulses," *Physics Reports*, vol. 833, pp. 1–52, 2019.

[66] T. Csizmadia et al., “Detailed study of quantum path interferences in high harmonic generation driven by chirped laser pulses,” *New Journal of Physics*, vol. 23, no. 12, p. 123 012, 2021.

[67] L. V. Keldysh, “Ionization in the field of a strong electromagnetic wave,” *Sov. Phys. JETP*, vol. 20, pp. 1307–1314, 1965.

[68] N. Boroumand, A. Thorpe, A. M. Parks, and T. Brabec, “Keldysh ionization theory of atoms: Mathematical details,” *Journal of Physics B: Atomic, Molecular and Optical Physics*, vol. 55, no. 21, p. 213 001, 2022.

[69] K. Kulander, K. Schafer, and J. Krause, *Time-dependent studies of multiphoton processes.* Academic Press Inc., 1992, pp. 247–300.

[70] A. M. Perelomov, V. S. Popov, and M. V. Terentev, “Ionization of atoms in an alternating electric field,” *Zhurnal Eksperimental'noi i Teoreticheskoi Fiziki (U.S.S.R.) For English translation see Sov. Phys. - JETP (Engl. Transl.)*, vol. Vol: 50, 1966.

[71] A.-T. Le, H. Wei, C. Jin, and C. D. Lin, “Strong-field approximation and its extension for high-order harmonic generation with mid-infrared lasers,” *Journal of Physics B: Atomic, Molecular and Optical Physics*, vol. 49, no. 5, p. 053 001, 2016.

[72] T. Shaaran, M. F. Ciappina, and M. Lewenstein, “Quantum-orbit analysis of high-order-harmonic generation by resonant plasmon field enhancement,” *Physical Review A*, vol. 86, no. 2, p. 023 408, 2012. arXiv: `1206.3023v2`.

[73] P. Agostini and L. F. DiMauro, “The physics of attosecond light pulses,” *Reports on Progress in Physics*, vol. 67, no. 6, pp. 813–855, 2004.

[74] M. Lewenstein, P. Salières, and A. L'Huillier, “Phase of the atomic polarization in high-order harmonic generation,” *Physical Review A*, vol. 52, no. 6, pp. 4747–4754, 1995.

[75] A. L'Huillier et al., “High-order harmonic-generation cutoff,” *Physical Review A*, vol. 48, no. 5, R3433–r3436, 1993.

[76] L. D. Landau and E. M. Lifshitz, *The Classical Theory of Fields.* Moscow: Foreign Languages Publishing House, 1951, vol. 2, First edition; Translated from the Russian.

[77] A. Yariv, *Quantum electronics*, 3. ed. New York [u.a.]: Wiley, 1989, 676 pp.

[78] J. Lambert, *Photometria sive de mensura et gradibus luminis, colorum et umbrae.* sumptibus vidvae E. Klett, typis C.P. Detleffsen, 1760.

[79] A. Beer, “Bestimmung der Absorption des rothen Lichts in farbigen Flüssigkeiten,” *Annalen der Physik und Chemie*, vol. 86, pp. 78–98, 1852.

[80] E. Constant et al., “Optimizing high harmonic generation in absorbing gases: Model and experiment,” *Physical Review Letters*, vol. 82, no. 8, pp. 1668–1671, 1999.

[81] B. Major, K. Kovács, V. Tosa, P. Rudawski, A. L’Huillier, and K. Varjú, “Effect of plasma-core-induced self-guiding on phase matching of high-order harmonic generation in gases,” *J. Opt. Soc. Am. B*, vol. 36, no. 6, pp. 1594–1601, 2019.

[82] B. Major and K. Varjú, “Extended model for optimizing high-order harmonic generation in absorbing gases,” *Journal of Physics B: Atomic, Molecular and Optical Physics*, vol. 54, no. 22, p. 224 002, 2021.

[83] C. M. Heyl, C. L. Arnold, A. Couairon, and A. L’Huillier, “Introduction to macroscopic power scaling principles for high-order harmonic generation,” *Journal of Physics B: Atomic, Molecular and Optical Physics*, vol. 50, no. 1, p. 013 001, 2016.

[84] R. Weissenbilder et al., “How to optimize high-order harmonic generation in gases,” *Nature Reviews Physics*, vol. 4, no. 11, pp. 713–722, 2022.

[85] C. Guo et al., “Phase control of attosecond pulses in a train,” *Journal of Physics B: Atomic, Molecular and Optical Physics*, vol. 51, no. 3, p. 034 006, 2018.

[86] `https://refractiveindex.info/?shelf=main&book=Ar&page=Bideau-Mehu`.

[87] B. Henke, E. Gullikson, and J. Davis, “X-ray interactions: Photoabsorption, scattering, transmission, and reflection at e = 50-30,000 ev, z = 1-92,” *Atomic Data and Nuclear Data Tables*, vol. 54, no. 2, pp. 181–342, 1993.

[88] `https://henke.lbl.gov/optical_constants/sf/ar.nff`.

[89] C. G. B. Garrett and D. E. McCumber, “Propagation of a gaussian light pulse through an anomalous dispersion medium,” *Physical Review A*, vol. 1, no. 2, pp. 305–313, 1970.

[90] J.-C. DIELS, *Ultrashort laser pulse phenomena, Fundamentals, techniques, and applications on a femtosecond time scale* (Optics and photonics), 2nd ed., J.-C. Diels and W. Rudolph, Eds. Amsterdam: Elsevier/Academic Press, 2006, 652 pp., Previous ed.: 1996. - Includes bibliographical references and index. - Description based on print version record.

[91] V. Tosa, K. T. Kim, and C. H. Nam, “Macroscopic generation of attosecond-pulse trains in strongly ionized media,” *Physical Review A*, vol. 79, no. 4, 2009.

[92] E. Priori et al., “Nonadiabatic three-dimensional model of high-order harmonic generation in the few-optical-cycle regime,” *Phys. Rev. A*, vol. 61, p. 063 801, 6 2000.

[93] M. Geissler, G. Tempea, A. Scrinzi, M. Schnürer, F. Krausz, and T. Brabec, "Light propagation in field-ionizing media: Extreme nonlinear optics," *Phys. Rev. Lett.*, vol. 83, pp. 2930–2933, 15 1999.

[94] M. Ibnchaikh and A. Belafhal, "The abcd-hankel transformation in two-dimensional frequency-domain with polar coordinates," *Phys. Chem. News*, vol. 2, pp. 29–34, 2001.

[95] B. Major, Z. L. Horváth, and K. Varjú, "Spatial characterization of light beams analyzed by cylindrical-grating slit-less spectrometers," *Appl. Opt.*, vol. 57, no. 4, pp. 738–745, 2018.

[96] V. P. Majety and A. Scrinzi, "Static field ionization rates for multi-electron atoms and small molecules," *Journal of Physics B: Atomic, Molecular and Optical Physics*, vol. 48, no. 24, p. 245 603, 2015.

[97] M. V. Ammosov, N. B. Delone, and V. P. Krainov, "Tunnel ionization of complex atoms and of atomic ions in an altemating electromagnetic field," *Sov. Phys. JETP*, vol. 64, p. 1191, 1987.

[98] U. Huttner, K. Schuh, J. V. Moloney, and S. W. Koch, "Similarities and differences between high-harmonic generation in atoms and solids," *Journal of the Optical Society of America B*, vol. 33, no. 7, p. C22, 2016.

[99] G. Vampa and T. Brabec, "Merge of high harmonic generation from gases and solids and its implications for attosecond science," *Journal of Physics B: Atomic, Molecular and Optical Physics*, vol. 50, no. 8, p. 083 001, 2017.

[100] L. Plaja and L. Roso-Franco, "High-order harmonic generation in a crystalline solid," *Physical Review B*, vol. 45, no. 15, pp. 8334–8341, 1992.

[101] M. Wu, S. Ghimire, D. A. Reis, K. J. Schafer, and M. B. Gaarde, "High-harmonic generation from bloch electrons in solids," *Physical Review A*, vol. 91, no. 4, 2015.

[102] M. Korbman, S. Yu Kruchinin, and V. S. Yakovlev, "Quantum beats in the polarization response of a dielectric to intense few-cycle laser pulses," *New Journal of Physics*, vol. 15, no. 1, p. 013 006, 2013.

[103] L. Yue and M. B. Gaarde, "Introduction to theory of high-harmonic generation in solids: Tutorial," *Journal of the Optical Society of America B*, vol. 39, no. 2, p. 535, 2022.

[104] C. M. Heyl, J. Güdde, A. L'Huillier, and U. Höfer, "High-order harmonic generation with μj laser pulses at high repetition rates," *Journal of Physics B: Atomic, Molecular and Optical Physics*, vol. 45, no. 7, p. 074 020, 2012.

[105] J. Rothhardt, M. Krebs, S. Hädrich, S. Demmler, J. Limpert, and A. Tünnermann, "Absorption-limited and phase-matched high harmonic generation in the tight focusing regime," *New Journal of Physics*, vol. 16, no. 3, p. 033 022, 2014.

[106] Eli, *User portal for the long beamline*, `https://up.eli-laser.eu/equipment/sylos-ghhg-long-562069531`, 2025.

[107] S. Kühn et al., "The eli-alps facility: The next generation of attosecond sources," *J. Phys. B At. Mol. Opt. Phys.*, vol. 50, no. 13, 2017.

[108] D. Charalambidis et al., "The Extreme Light Infrastructure—Attosecond Light Pulse Source (ELI-ALPS) Project," in *Progress in Ultrafast Intense Laser Science XIII*. Springer International Publishing, 2017, pp. 181–218.

[109] S. Kahaly and K. Varju, "ELI ALPS status and challenges," in *Research Using Extreme Light Infrastructures: New Frontiers with Petawatt-Level Lasers VI*, B. Rus, D. Margarone, and V. Malka, Eds., SPIE, 2025, p. 2.

[110] L.L.C., *Lund laser centre homepage*, `https://www.llc.lu.se/`, 2025.

[111] M. Shirozhan et al., "High-repetition-rate attosecond extreme ultraviolet beamlines at eli alps for studying ultrafast phenomena," *Ultrafast Science*, vol. 4, 2024, MTMT: 35294705, IF: 9.9.

[112] ElI, *User portal for the SEA laser*, `https://up.eli-laser.eu/laser/sea-561610773`, 2025.

[113] R. Budriūnas et al., "53 w average power cep-stabilized opcpa system delivering 55 tw few cycle pulses at 1 khz repetition rate," *Opt. Express*, vol. 25, no. 5, p. 5797, 2017.

[114] Gentec, *Gentec measurement tools product page*, `https://www.gentec-eo.com/laser-energy-meter`, 2025.

[115] C. A. Schneider, W. S. Rasband, and K. W. Eliceiri, "Nih image to imagej: 25 years of image analysis," *Nature Methods*, vol. 9, no. 7, pp. 671–675, 2012.

[116] P. Tournois, "Acousto-optic programmable dispersive filter for adaptive compensation of group delay time dispersion in laser systems," *Optics Communications*, vol. 140, no. 4–6, pp. 245–249, 1997.

[117] V. Loriot, G. Gitzinger, and N. Forget, "Self-referenced characterization of femtosecond laser pulses by chirp scan," *Optics Express*, vol. 21, no. 21, p. 24 879, 2013.

[118] M. Miranda et al., "Characterization of broadband few-cycle laser pulses with the d-scan technique," *Opt. Express*, vol. 20, no. 17, p. 18 732, 2012.

[119] *Beam imaging solutions*, `https://beamimaging.com/`, 2025.

[120] G. Pretzler, A. Kasper, and K. Witte, "Angular chirp and tilted light pulses in cpa lasers," *Applied Physics B: Lasers and Optics*, vol. 70, no. 1, pp. 1–9, 2000.

[121] A. L. Hoendervanger et al., "Influence of gold coating and interplate voltage on the performance of chevron micro-channel plates for temporally and spatially resolved single particle detection," *Review of Scientific Instruments*, vol. 84, no. 2, 2013.

[122] L. Quintard et al., "Optics-less focusing of xuv high-order harmonics," *Science Advances*, vol. 5, no. 4, 2019.

[123] E. Sobolev et al., "Terawatt-level three-stage pulse compression for all-attosecond pump-probe spectroscopy," *Optics Express*, vol. 32, no. 26, p. 46 251, 2024.

[124] T. Pak et al., "Multi-millijoule terahertz emission from laser-wakefield-accelerated electrons," *Light: Science and Applications*, vol. 12, no. 1, 2023.

[125] X.-L. Zhu, S.-M. Weng, M. Chen, Z.-M. Sheng, and J. Zhang, "Efficient generation of relativistic near-single-cycle mid-infrared pulses in plasmas," *Light: Science and; Applications*, vol. 9, no. 1, 2020.

[126] U. Even, J. Jortner, D. Noy, N. Lavie, and C. Cossart-Magos, "Cooling of large molecules below 1 k and he clusters formation," *The Journal of Chemical Physics*, vol. 112, no. 18, pp. 8068–8071, 2000.

[127] U. Even, ""the even-lavie valve as a source for high intensity supersonic beam"," *EPJ Techniques and Instrumentation*, vol. 2, no. 1, 2015.

[128] A. Auerbach and R. McDiarmid, "Modified pulsed valve for supersonic jet applications," *Review of Scientific Instruments*, vol. 51, no. 9, pp. 1273–1275, 1980.

[129] F. Sylla, M. Veltcheva, S. Kahaly, A. Flacco, and V. Malka, "Development and characterization of very dense submillimetric gas jets for laser-plasma interaction," *Rev. Sci. Instrum.*, vol. 83, no. 3, p. 033 507, 2012.

[130] N. H. Abel, "Auflösung einer mechanischen Aufgabe.," *J. für die reine und Angew. Math. (Crelles Journal)*, vol. 1826, no. 1, pp. 153–157, 1826.

[131] A. N. Tichonov and V. J. Arsenin, *Solutions of ill-posed problems* (A @Halsted Press book). New York, NY [u.a.]: Wiley, 1977, 258 pp., Aus d. Russ. übers.

[132] D. Colton and R. Kress, "Ill-posed problems," in *Inverse Acoustic and Electromagnetic Scattering Theory*. Springer International Publishing, 2019, pp. 111–136.

[133] J. Hadamard, "Sur les problèmes aux dérivées partielles et leur signification physique," *Princeton University Bulletin*, vol. 13, pp. 49–52, 1902.

[134] J. Hadamard, *Lectures on Cauchy's Problem in Linear Partial Differential Equations.* New Haven: Yale University Press, 1923.

[135] I. I. Antokhin, "An efficient and flexible abel-inversion method for noisy data," *Monthly Notices of the Royal Astronomical Society*, vol. 463, no. 2, pp. 2079–2084, 2016.

[136] T. G. Mayerhöfer and J. Popp, "Beyond beer's law: Revisiting the lorentz-lorenz equation," *ChemPhysChem*, vol. 21, no. 12, pp. 1218–1223, 2020.

[137] H. Kragh, "The lorenz-lorentz formula: Origin and early history," en, *Substantia*, Vol 2 No 2 (2018), 2018.

[138] O. F. Mossotti, "Discussione analitica sull'influenza che l'azione di un mezzo dielettrico ha sulla distribuzione dell'elettricità alla superficie di più corpi electrici disseminati in esso," *Memorie di matematica e di fisica della Società italiana delle scienze residente in Modena (Part II)*, vol. 24, pp. 49–74, 1850, In Italian. Original publication; commonly cited as the historical antecedent of the Clausius–Mossotti relation. Archival scan: Archive.org / Biodiversity Heritage Library.

[139] R. J. E. Clausius, *Die mechanische Behandlung der Electricität.* Braunschweig: Vieweg & Sohn, 1879, Original German edition (see historical discussions of the Clausius–Mossotti relation). Scans/preview available via Google Books / archive.org.

[140] L. Onsager, "Electric moments of molecules in liquids," *Journal of the American Chemical Society*, vol. 58, no. 8, pp. 1486–1493, 1936.

[141] P. Debye, "Zur theorie der spezifischen wärmen," *Annalen der Physik*, vol. 344, no. 14, pp. 789–839, 1912.

[142] L. McMackin, R. J. Hugo, R. E. Pierson, and C. R. Truman, "High speed optical tomography system for imaging dynamic transparent media," *Optics Express*, vol. 1, no. 11, p. 302, 1997.

[143] P. B. Gooderum, G. P. Wood, and M. J. Brevoort, "Investigation with an interferometer of the turbulent mixing of a free supersonic jet," Langley Aeronautical Laboratory, National Advisory Committee for Aeronautics (NACA), Langley Field, Virginia, USA, Technical Report NACA-TR-963, 1949, Document acquired 1949; 30 pages; includes interferometric density and velocity distributions.

[144] J. Edwards, *Application of the interferometer to gas analysis.* 1919.

[145] H. Man, J. Duan, and T. Yue, "Dynamic characteristics of gas jets from subsonic and supersonic nozzles for high pressure gas laser cutting," *Optics amp; Laser Technology*, vol. 30, no. 8, pp. 497–509, 1998.

[146] M. Takeda, H. Ina, and S. Kobayashi, “Fourier-transform method of fringe-pattern analysis for computer-based topography and interferometry,” *J. Opt. Soc. Am.*, vol. 72, no. 1, p. 156, 1982.

[147] M. BV, *Piezo amsterdam pulsed valve*, `https://www.amsterdampiezovalve.com/`, 2025.

[148] C. R. Harris et al., “Array programming with NumPy,” *Nature*, vol. 585, no. 7825, pp. 357–362, 2020.

[149] P. Virtanen et al., “SciPy 1.0: Fundamental Algorithms for Scientific Computing in Python,” *Nature Methods*, vol. 17, pp. 261–272, 2020.

[150] G. Bradski, “The OpenCV Library,” *Dr. Dobb’s Journal of Software Tools*, 2000.

[151] A. Kantrowitz and J. Grey, “A high intensity source for the molecular beam. part i. theoretical,” *Review of Scientific Instruments*, vol. 22, no. 5, pp. 328–332, 1951.

[152] S. Kühn et al., “The eli-alps facility: The next generation of attosecond sources,” *Journal of Physics B: Atomic, Molecular and Optical Physics*, vol. 50, no. 13, p. 132 002, 2017.

[153] I. Orfanos et al., “Two-xuv-photon double ionization of neon,” *Physical Review A*, vol. 106, no. 4, p. 043 117, 2022.

[154] Eli, *User portal for the compact beamline*, `https://up.eli-laser.eu/equipment/sylos-ghhg-comp-562036739`, 2025.

[155] K. Amini et al., “Symphony on strong field approximation,” *Reports on Progress in Physics*, vol. 82, no. 11, p. 116 001, 2019.

[156] J. Schötz et al., “Phase-matching for generation of isolated attosecond xuv and soft-x-ray pulses with few-cycle drivers,” *Phys. Rev. X*, vol. 10, p. 041 011, 4 2020.

[157] B. Schütte et al., “Bright attosecond soft x-ray pulse trains by transient phase-matching in two-color high-order harmonic generation,” *Opt. Express*, vol. 23, no. 26, pp. 33 947–33 955, 2015.

[158] B. H. Failor, S. Chantrenne, P. L. Coleman, J. S. Levine, Y. Song, and H. M. Sze, “Proof-of-principle laser-induced fluorescence measurements of gas distributions from supersonic nozzles,” *Review of Scientific Instruments*, vol. 74, no. 2, pp. 1070–1076, 2003.

[159] A. Comby, S. Beaulieu, E. Constant, D. Descamps, S. Petit, and Y. Mairesse, “Absolute gas density profiling in high-order harmonic generation,” *Optics Express*, vol. 26, no. 5, p. 6001, 2018.

[160] S. Chatziathanasiou et al., “Quantum path interferences in high-order harmonic generation from aligned diatomic molecules,” *Physical Review A*, vol. 100, no. 6, 2019.

[161] A. Lifschitz et al., “Ion acceleration in underdense plasmas by ultra-short laser pulses,” *New Journal of Physics*, vol. 16, no. 3, p. 033 031, 2014.

[162] S. Kahaly, F. Sylla, A. Lifschitz, A. Flacco, M. Veltcheva, and V. Malka, “Detailed experimental study of ion acceleration by interaction of an ultra-short intense laser with an underdense plasma,” *Scientific Reports*, vol. 6, no. 1, 2016.

[163] H. Wikmark et al., “Spatiotemporal coupling of attosecond pulses,” *Proceedings of the National Academy of Sciences*, vol. 116, no. 11, pp. 4779–4787, 2019.

[164] A. Dubrouil et al., “Spatio–spectral structures in high-order harmonic beams generated with terawatt 10-fs pulses,” *Nature Communications*, vol. 5, no. 1, 2014.

[165] M. Hoflund et al., “Focusing properties of high-order harmonics,” *Ultrafast Science*, vol. 2021, 2021.

[166] L. Drescher et al., “Extreme-ultraviolet refractive optics,” *Nature*, vol. 564, no. 7734, pp. 91–94, 2018.

[167] M. Kübel et al., “High-order phase-dependent asymmetry in the above-threshold ionization plateau,” *Physical Review Letters*, vol. 126, no. 11, p. 113 201, 2021.

[168] L. Xu, T. W. Hänsch, C. Spielmann, A. Poppe, T. Brabec, and F. Krausz, “Route to phase control of ultrashort light pulses,” *Optics Letters*, vol. 21, no. 24, p. 2008, 1996.

[169] Amplitude, *Fringeezz device product page*, `https://amplitude-laser.com/add_ons/metrology/fringeezz/`, 2025.

[170] Eli, *User portal for the sylos2 laser*, `https://up.eli-laser.eu/laser/sylos-2-1415610464`, 2025.

[171] G. Sansone et al., “Isolated single-cycle attosecond pulses,” *Science*, vol. 314, no. 5798, pp. 443–446, 2006.

[172] G. Carleo et al., “Machine learning and the physical sciences,” *Reviews of Modern Physics*, vol. 91, no. 4, p. 045 002, 2019.

[173] F. F. Sahle and T. L. Lowe, “Design strategies for programmable oligonucleotide nanotherapeutics,” *Drug Discovery Today*, vol. 25, no. 1, pp. 73–88, 2020.

[174] T. Cover and P. Hart, “Nearest neighbor pattern classification,” *IEEE Transactions on Information Theory*, vol. 13, no. 1, pp. 21–27, 1967.

[175] L. Breiman, “Bagging predictors,” *Machine Learning*, vol. 24, no. 2, pp. 123–140, 1996.

[176] L. Breiman, J. H. Friedman, R. A. Olshen, and C. J. Stone, *Classification And Regression Trees*. Routledge, 2017.

[177] K. Choudhary et al., “Recent advances and applications of deep learning methods in materials science,” *npj Computational Materials*, vol. 8, no. 1, 2022.

[178] J. Ojih, M. Al-Fahdi, A. D. Rodriguez, K. Choudhary, and M. Hu, “Efficiently searching extreme mechanical properties via boundless objective-free exploration and minimal first-principles calculations,” *npj Computational Materials*, vol. 8, no. 1, 2022.

[179] J. Carrete, W. Li, N. Mingo, S. Wang, and S. Curtarolo, “Finding unprecedentedly low-thermal-conductivity half-heusler semiconductors via high-throughput materials modeling,” *Physical Review X*, vol. 4, no. 1, p. 011 019, 2014.

[180] T. Xie and J. C. Grossman, “Crystal graph convolutional neural networks for an accurate and interpretable prediction of material properties,” *Physical Review Letters*, vol. 120, no. 14, p. 145 301, 2018.

[181] M. Raissi, P. Perdikaris, and G. Karniadakis, “Physics-informed neural networks: A deep learning framework for solving forward and inverse problems involving nonlinear partial differential equations,” *Journal of Computational Physics*, vol. 378, pp. 686–707, 2019.

[182] K. Duraisamy, G. Iaccarino, and H. Xiao, “Turbulence modeling in the age of data,” *Annual Review of Fluid Mechanics*, vol. 51, no. 1, pp. 357–377, 2019.

[183] T. Zahavy et al., “Deep learning reconstruction of ultrashort pulses,” *Optica*, vol. 5, no. 5, p. 666, 2018.

[184] M. Stanfield et al., “Real-time reconstruction of high energy, ultrafast laser pulses using deep learning,” *Scientific Reports*, vol. 12, no. 1, 2022.

[185] I. Tóth, A. M. M. Gherman, K. Kovács, W. Cho, H. Yun, and V. Toşa, “Reconstruction of femtosecond laser pulses from frog traces by convolutional neural networks,” *Photonics*, vol. 10, no. 11, p. 1195, 2023.

[186] S. Fabbro et al., “An application of deep learning in the analysis of stellar spectra,” *Monthly Notices of the Royal Astronomical Society*, vol. 475, no. 3, pp. 2978–2993, 2017.

[187] H. W. Leung and J. Bovy, “Deep learning of multi-element abundances from high-resolution spectroscopic data,” *Monthly Notices of the Royal Astronomical Society*, 2018.

[188] N. Altman and M. Krzywinski, “Simple linear regression,” *Nature Methods*, vol. 12, no. 11, pp. 999–1000, 2015.

[189] M. Krzywinski and N. Altman, “Multiple linear regression,” *Nature Methods*, vol. 12, no. 12, pp. 1103–1104, 2015.

[190] R. Tibshirani, “Regression shrinkage and selection via the lasso,” *Journal of the Royal Statistical Society Series B: Statistical Methodology*, vol. 58, no. 1, pp. 267–288, 1996.

[191] S. Amari, “A theory of adaptive pattern classifiers,” *IEEE Transactions on Electronic Computers*, vol. EC-16, no. 3, pp. 299–307, 1967.

[192] S.-i. Amari, “Natural gradient works efficiently in learning,” *Neural Computation*, vol. 10, no. 2, pp. 251–276, 1998.

[193] P. Geurts, D. Ernst, and L. Wehenkel, “Extremely randomized trees,” *Machine Learning*, vol. 63, no. 1, pp. 3–42, 2006.

[194] R. Flender et al., “Dispersive mirror characterization and application for mid-infrared post-compression,” *Journal of Optics*, vol. 23, no. 6, p. 065 501, 2021.

[195] R. Hollinger et al., “Carrier-envelope-phase measurement of few-cycle mid-infrared laser pulses using high harmonic generation in zno,” *Optics Express*, vol. 28, no. 5, p. 7314, 2020.

[196] Y. S. You et al., “High-harmonic generation in amorphous solids,” *Nature Communications*, vol. 8, no. 1, 2017.

[197] H. Mashiko et al., “Double optical gating of high-order harmonic generation with carrier-envelope phase stabilized lasers,” *Physical Review Letters*, vol. 100, no. 10, p. 103 906, 2008.

[198] N. Tancogne-Dejean, O. D. Mücke, F. X. Kärtner, and A. Rubio, “Ellipticity dependence of high-harmonic generation in solids originating from coupled intraband and interband dynamics,” *Nature Communications*, vol. 8, no. 1, 2017.

[199] P. Földi, M. G. Benedict, and V. S. Yakovlev, “The effect of dynamical bloch oscillations on optical-field-induced current in a wide-gap dielectric,” *New Journal of Physics*, vol. 15, no. 6, p. 063 019, 2013.

[200] N. Thiré et al., “Highly stable, 15 w, few-cycle, 65 mrad cep-noise mid-ir opcpa for statistical physics,” *Optics Express*, vol. 26, no. 21, p. 26 907, 2018.

[201] S. B. Park et al., “Direct sampling of a light wave in air,” *Optica*, vol. 5, no. 4, p. 402, 2018.

[202] S. Gholam-Mirzaei, J. Beetar, and M. Chini, “High harmonic generation in zno with a high-power mid-ir opa,” *Applied Physics Letters*, vol. 110, no. 6, 2017.

[203] W. Cho, J.-u. Shin, and K. T. Kim, “Reconstruction algorithm for tunneling ionization with a perturbation for the time-domain observation of an electric-field,” *Scientific Reports*, vol. 11, no. 1, 2021.

[204] Y. S. You et al., “Laser waveform control of extreme ultraviolet high harmonics from solids,” *Optics Letters*, vol. 42, no. 9, p. 1816, 2017.

[205] I. Tóth, A. M. M. Gherman, K. Kovács, W. Cho, H. Yun, and V. Toşa, “Reconstruction of femtosecond laser pulses from frog traces by convolutional neural networks,” *Photonics*, vol. 10, no. 11, p. 1195, 2023.

[206] A. L’Huillier, “Nobel lecture: The route to attosecond pulses,” *Rev. Mod. Phys.*, vol. 96, p. 030 503, 3 2024.

[207] F. Krausz, “Nobel lecture: Sub-atomic motions,” *Rev. Mod. Phys.*, vol. 96, p. 030 502, 3 2024.

[208] P. Agostini, “Nobel lecture: Genesis and applications of attosecond pulse trains,” *Rev. Mod. Phys.*, vol. 96, p. 030 501, 3 2024.

[209] M. M. Aléonard et al., *Whitebook ELI – Extreme Light Infrastructure; Science and Technology with Ultra-Intense Lasers*, pt. Andreas Thoss, 2011.

[210] J. Rothhardt, S. Hädrich, J. Delagnes, E. Cormier, and J. Limpert, “High average power near-infrared few-cycle lasers (laser photonics rev. 11(4)/2017),” *Laser and Photonics Reviews*, vol. 11, no. 4, 2017.

[211] S. Ghimire, A. D. DiChiara, E. Sistrunk, P. Agostini, L. F. DiMauro, and D. A. Reis, “Observation of high-order harmonic generation in a bulk crystal,” *Nature Physics*, vol. 7, no. 2, pp. 138–141, 2010.

Publications

Own publications

(P1) **B. Nagyillés**, Z. Diveki, A. Nayak, M. Dumergue, B. Major, K. Varjú, and S. Kahaly, “Time-resolved investigation of a high-repetition-rate gas-jet target for high-harmonic generation,” *Physical Review Applied*, vol. 20, no. 5, p. 054 048, 2023, MTMT: 34434071, IF: 4.4

(P2) **B. Nagyillés**, G. N. Nagy, B. Kiss, E. Cormier, P. Földi, K. Varjú, S. Kahaly, M. U. Kahaly, and Z. Diveki, “Mir laser cep estimation using machine learning concepts in bulk high harmonic generation,” *Optics Express*, vol. 32, no. 26, p. 46 500, 2024, MTMT: 35670820, IF: 3.3

(P3) E. Appi, R. Weissenbilder, **B. Nagyillés**, Z. Diveki, J. Peschel, B. Farkas, M. Plach, F. Vismarra, V. Poulain, N. Weber, C. L. Arnold, K. Varjú, S. Kahaly, P. Eng-Johnsson, and A. L’Huillier, “Two phase-matching regimes in high-order harmonic generation,” *Optics Express*, vol. 31, no. 20, p. 31 687, 2023, MTMT: 34393336, IF: 3.3

Other own publications

(O1) P. Ye, T. Csizmadia, L. G. Oldal, H. N. Gopalakrishna, M. Füle, Z. Filus, **B. Nagyillés**, Z. Divéki, T. Grósz, M. Dumergue, P. Jójárt, I. Seres, Z. Bengery, V. Zuba, Z. Várallyay, B. Major, F. Frassetto, M. Devetta, G. D. Lucarelli, M. Lucchini, B. Moio, S. Stagira, C. Vozzi, L. Poletto, M. Nisoli, D. Charalambidis, S. Kahaly, A. Zaïr, and K. Varjú, "Attosecond pulse generation at eli-alps 100 khz repetition rate beamline," *Journal of Physics B: Atomic, Molecular and Optical Physics*, vol. 53, no. 15, p. 154 004, 2020, MTMT: 31421355, IF: 1.5

(O2) K. Chordiya, V. Despré, **B. Nagyillés**, F. Zeller, Z. Diveki, A. I. Kuleff, and M. U. Kahaly, "Photo-ionization initiated differential ultrafast charge migration: Impacts of molecular symmetries and tautomeric forms," *Physical Chemistry Chemical Physics*, vol. 25, no. 6, pp. 4472–4480, 2023, MTMT: 33107909, IF: 3.676

(O3) M. Staněk, O. Hort, L. Jurkovičová, M. Albrecht, O. Finke, **B. Nagyillés**, B. Farkas, T. Csizmadia, T. Grósz, A. Körmöczi, Z. Divéki, and J. Nejdl, "Photoelectric charge from metallic filters: An online xuv pulse energy diagnostics," *Applied Physics Letters*, vol. 125, no. 9, 2024, MTMT: 35256432, IF: 3.6

(O4) M. Shirozhan, S. Mondal, T. Grósz, **B. Nagyillés**, B. Farkas, A. Nayak, N. Ahmed, I. Dey, S. C. De Marco, K. Nelissen, M. Kiss, L. G. Oldal, T. Csizmadia, Z. Filus, M. De Marco, S. Madas, M. U. Kahaly, D. Charalambidis, P. Tzallas, E. Appi, R. Weissenbilder, P. Eng-Johnsson, A. L'Huillier, Z. Diveki, B. Major, K. Varjú, and S. Kahaly, "High-repetition-rate attosecond extreme ultraviolet beamlines at eli alps for studying ultrafast phenomena," *Ultrafast Science*, vol. 4, 2024, MTMT: 35294705, IF: 9.9

(O5) E. Skantzakis, I. Orfanos, A. Nayak, I. Makos, I. Liontos, E. Vassakis, T. Lamprou, V. Tsafas, T. Csizmadia, Z. Diveki, **B. Nagyillés**, B. Farkas, S. Mukhopadhyay, D. Rajak, S. Madas, M. Upadhyay Kahaly, S. Kahaly, R. Weissenbilder, P. Eng-Johnsson, E. Appi, A. L'Huillier, G. Sansone, K. Varju, L. A. A. Nikolopoulos, A. Emmanouilidou, P. Tzallas, and D. Charalambidis, "Non-linear extreme ultraviolet applications with attosecond pulses," in *Progress in Ultrafast Intense Laser Science XVII.* Springer Nature Switzerland, 2024, pp. 1–24, MTMT: 35061801

Presentations, Posters, Conference papers

(C1) B. Major, B. Farkas, M. Dumergue, K. Kovacs, S. Kuehn, A. L'Huillier, **B. Nagyillés**, P. Rudawski, V. Tosa, P. Tzallas, D. Charalambidis, K. Osvay, G. Sansone, and K. Varjú, "The eli alps research infrastructure: Scaling attosecond pulse generation for a large scale infrastructure," in *High-Brightness Sources and Light-driven Interactions*, ser. HILAS, OSA, 2018, HW4A.1, MTMT: 27462331

(C2) **B. Nagyillés** et al., *Eli-alps sylos ghhg beamlines: Optimizing generation conditions for high-power laser pulses*, Poster at Atto VII, Szeged, Hungary, Demonstration of Attosecond beamline, 2019

(C3) **B. Nagyillés** et al., *High flux high harmonic generation at the sylos long beamline at eli-alps*, Poster at Atto VIII, Orlando, Florida, 2022

(C4) **B. Nagyillés** et al., *Time resolved characterization of high repetition rate gas jet target for high harmonic generation*, Poster at Atto IX, Jeju, Korea, 2023

(C5) R. Weissenbilder, E. Appi, J. Peschel, **B. Nagyillés**, S. Carlström, Z. Divéki, B. Farkas, M. Plach, K. Varjú, S. Kahaly, C. L. Arnold, P. Eng-Johnsson, and A. L'Huillier, "Hyperbolic trend in optimization of high-order harmonic generation in gases," in *2023 Conference on Lasers and Electro-Optics (CLEO)*, 2023, pp. 1–2, MTMT: 34434143

(C6) **B. Nagyillés** et al., *Mir laser cep estimation using machine learning concepts in bulk high harmonic generation*, Poster at 5th Attochem Workshop, Tenerife, Spain, 2024

(C7) **B. Nagyillés**, *Mir laser cep estimation using machine learning concepts in bulk high harmonic generation*, Talk at USTS 2024, Sitges, Spain, 2024

(C8) **B. Nagyillés**, *Extreme ultraviolet time-resolved photoelectron spectroscopy: Toward the ultimate probe of molecular dynamics*, Poster at XUVTRPES Workshop 2025, Freiburg, 2025

(C9) **B. Nagyillés**, *The effect of laser pulse duration on the yield of high harmonic generation*, Poster presentation at Atto X, Lund, Sweden, 2025

(C10) D. István, C. János, T. Szabolcs, T. L. Tamás, S. Tamás, G. P. Prasannan, A. D. Jenő, K. Balázs, D. Zsolt, **B. Nagyillés**, F. Balázs, K. Andor, and B. Ádám, *A sylos2a lézerrendszer és a vákuum szerepe a hullámfront stabilizálásában*, Kvantumelektronika : Szimpózium a hazai kvantumelektronikai kutatások eredményeiről Bibliogr.: 23. p. ; ill. 2025, MTMT: 36329464

Acknowledgements

First and foremost, I would like to thank my wife, Dr. Kalyani Chordiya, for her endless patience and support. Over the past year, a substantial part of my free time was devoted to this work, and her understanding made it possible. I am also deeply grateful to my parents, siblings, and in-laws, who have always encouraged me and stood behind me in so many aspects of life.

I would like to express my gratitude to Dr. Zsolt Divéki for the many research projects we carried out together and for agreeing to supervise this work. I am equally thankful to Dr. Subhendu Kahaly, whose guidance and supervision was invaluable both during my PhD and in the process of publishing my research. I owe much to Prof. Katalin Varjú, who has supported my work since my MSc studies, and to Balázs Farkas, with whom I have worked since my BSc years. I would also like to thank Dr. Balázs Major for introducing me to the simulation code and for patiently answering countless questions, and Dr. Andor Körmöczi, who generously took over many of my responsibilities while I was writing this thesis. I am grateful as well to Dr. Bálint Kiss, who always offered support and secured beamtime for our experiments. There are far too many colleagues at ELI ALPS to name here, but I carry a great sense of appreciation for all those who contributed to and supported my work.

I would also like to thank our collaborators in Lund, who welcomed me during my secondment and provided valuable support in the development of the SYLOS GHHG Long beamline. In particular, I am indebted to Dr. Piotr Rudawski, Dr. Sylvain Maclot, Prof. Per Eng-Johnsson, and Prof. Anne L'Huillier for their expertise and encouragement.

Finally, this work would not have been possible without the facilities and resources of ELI ALPS. The project (GINOP-2.3.6-15-2015-00001) was supported by the European Union and co-financed by the European Regional Development Fund, for which I am sincerely grateful.